

The Local Ly α Forest. I. Observations with the GHRS/G160M on the Hubble Space Telescope ¹

Steven V. Penton, John T. Stocke, and J. Michael Shull ²

Center for Astrophysics and Space Astronomy, Department of Astrophysical and Planetary Sciences, University of Colorado, Boulder CO, 80309

spenton@casa.colorado.edu, stocke@casa.colorado.edu, mshull@casa.colorado.edu

ABSTRACT

We present the target selection, observations, and data reduction and analysis process for a program aimed at discovering numerous, weak (equivalent width ≤ 100 mÅ) Ly α absorption lines in the local Universe ($0.003 \leq z \leq 0.069$). The purpose of this program is to study the physical conditions of the local intergalactic medium, including absorber distributions in Doppler width and H I column density, redshift evolution of absorber number density, line-of-sight two-point correlation function, and the baryonic content and metallicity. By making use of large-angle, nearby galaxy redshift surveys, we will investigate the relationship (if any) between these Ly α absorbers and galaxies, superclusters and voids. In Paper I, we present high resolution (~ 19 km s⁻¹) spectroscopic observations of 15 very bright ($V \leq 14.5$) AGN targets made with the Goddard High Resolution Spectrograph (GHRS) aboard the Hubble Space Telescope (HST). We find 81 definite ($\geq 4\sigma$) and 30 possible ($3 - 4\sigma$) Ly α absorption lines in these spectra, which probe a total pathlength of 116,000 km s⁻¹ ($\Delta z \sim 0.4$) at very low redshift ($z \leq 0.069$) and column density ($12.5 \leq \log N_{\text{HI}} \leq 14.5$). We found numerous metal lines arising in the Milky Way halo, including absorption from high velocity clouds in 10 of 15 sightlines and numerous absorptions intrinsic to the target AGN. Here, we describe the details of the target selection, HST observations, and spectral reduction and analysis. We present reduced spectra, absorption line lists, “pie diagrams” showing the known galaxy distributions in the direction of each target, and nearest galaxy tables for each absorber. In Papers II and III, we use the data presented here to determine the basic physical characteristics of the low- z Ly α forest and to investigate the relationship of the absorbers to the local galaxy distribution.

Subject headings: intergalactic medium — quasars: absorption lines — ultraviolet: galaxies — galaxies: halos

¹Based on observations with the NASA/ESA Hubble Space Telescope, obtained at the Space Telescope Science Institute, which is operated by the Association of Universities for Research in Astronomy, Inc. under NASA contract No. NAS5-26555.

²Also at JILA, University of Colorado and National Institute of Standards and Technology.

1. Introduction

Since the discovery of the high-redshift Ly α forest over 25 years ago, these abundant absorption features in the spectra of QSOs have been used as evolutionary probes of the intergalactic medium (IGM), galactic halos, large-scale structure, and chemical evolution. These absorbers were originally divided into “metal-bearing” systems, which occur primarily at higher H I column densities, and Ly α -only systems, which occur primarily at lower H I column densities (Sargent 1987). Recent observations of C IV lines in Ly α absorbers with column densities $N_{\text{HI}} \geq 10^{14.5} \text{ cm}^{-2}$ (Tytler et al. 1995; Cowie et al. 1995) have blurred the distinction between these two population of absorbers. However, the clustering properties of the high-redshift C IV systems are more like those of galaxies than the Ly α clouds (Cristiani et al. 1997). Certainly many of the higher column density absorbers, particularly the Lyman limit systems (Steidel 1995) and damped-Ly α systems (Wolfe 1995), appear to be associated with the gaseous halos of individual galaxies. Thus, the distinction between these two populations may still be an important one.

In the past few years, these discrete Ly α lines have been interpreted theoretically by N-body hydrodynamical models (Cen et al. 1994; Hernquist et al. 1996; Zhang et al. 1997; Davé et al. 1999) as arising from baryon density fluctuations associated with gravitational instability during the epoch of structure formation. However, these models do not contain the detailed physics of star formation and supernova ejecta, which can move material from the disks of galaxies into the halo or beyond in a “galactic fountain” (Shapiro & Benjamin 1993; Slavin, Shull, & Begelman 1993). Therefore, these simulations cannot exclude the possibility that at least some Ly α absorbers are “recycled” gas from sites of active star formation in galaxies. Regardless, the lowest column density absorbers ($N_{\text{HI}} \leq 10^{14.5} \text{ cm}^{-2}$) are the most likely systems to be unassociated with galaxies and primordial in their chemical abundances.

At high redshift, ground-based observations indicate rapid evolution in the distribution of Ly α absorption lines per unit redshift, $dN/dz \propto (1+z)^\gamma$, where $\gamma \approx 2.5$ for $z \geq 1.5$. This evolution is consistent with a picture of these features as highly ionized “clouds” whose numbers and sizes were controlled by the evolution of the IGM pressure, the metagalactic ionizing radiation field, and galaxy formation. If the evolution in cloud numbers at $z > 1.6$ continued into the present epoch, few Ly α clouds would remain by $z \sim 0$. However, one of the delightful spectroscopic surprises from the first year of the *Hubble Space Telescope* (HST) was the discovery of many Ly α absorption lines toward the quasar 3C 273 at $z_{\text{em}} = 0.158$ by both the Faint Object Spectrograph (FOS, Bahcall et al. 1991b) and the Goddard High Resolution Spectrograph (GHRS, Morris et al. 1991, 1993). More recent data from HST support the slowing of the evolution of Ly α systems at $z \leq 1.5$ (Weymann et al. 1998). This evolutionary shift is probably a result of the collapse and assembly of baryonic structures in the IGM (Davé et al. 1999) together with the decline in the intensity of the ionizing radiation field (Haardt & Madau 1996; Shull et al. 1999b). Detailed results of the Ly α forest evolution in the redshift interval $0 < z < 1.5$ are described in the FOS Key Project papers: the three catalog papers (Bahcall et al. 1993, 1996; Jannuzi et al. 1998) and the evolutionary analysis (Weymann et al. 1998).

Because the HST/FOS studies were primarily detections of strong Ly α lines, with equivalent widths (EWs) greater than 0.24 Å, they most likely probe only the higher column density population of absorbers. A great deal more information about the low- z IGM can be gained from studies of the more plentiful weak absorbers, including the evolution of the lower column density population, which may be physically distinct. Realizing the importance of spectral resolution in detecting weak Ly α absorbers, the Colorado group has engaged in a long-term program with the HST/GHRS, using the G160M grating at 19 km s $^{-1}$ resolution to study the very low-redshift ($z < 0.07$) Ly α forest. Earlier results from our study have appeared in various papers (Stocke et al. 1995; Shull, Stocke, & Penton 1996; Shull et al. 1998) and reviews (Shull 1997; Shull, Penton, & Stocke 1999a). While other groups have used the GHRS to probe these lower column density clouds (e.g., Tripp, Lu, & Savage 1998a,b; Impey, Petry, & Flint 1999), their observations used the lower-resolution GHRS/G140L grating, which failed to detect the weakest Ly α lines and did not resolve the stronger ones. The program described here detects lines as weak as EW $\cong 13$ mÅ ($N_{\text{HI}} \sim 10^{12.5}$ cm $^{-2}$), comparable to the detection limit reached with the Keck Observatory plus HIRES spectrograph at high redshift (Songaila, Cowie, & Hu 1995). Because the HST/G160M resolves most of the Ly α absorption lines, it provides, for the first time, the range of observed Doppler parameters (b -values) and the two-point correlation function of the low- z Ly α forest at velocity separations ≤ 100 km s $^{-1}$.

In order to attain the required resolution and sensitivity, we made two important compromises in the observing strategy. First, only the brightest UV targets could be used for the program; the rare Seyferts, QSOs, and BL Lacs with $V \sim 14.5$ are our primary candidates. Second, because the HST/G160M grating yields only ~ 35 Å of useful coverage for Ly α forest lines, little pathlength is surveyed per target compared to either the FOS Key Project survey observations or the ground-based spectra at higher redshift. However, in many ways the $\sim 8,000$ km s $^{-1}$ pathlength surveyed by these spectra are the most important piece of the Ly α forest, being the nearest ~ 100 Mpc to us. The distances to Ly α absorbers discovered in the present survey allow an immediate comparison with galaxy locations derived from redshift surveys that sample approximately the same range in distances (e.g., the CfA redshift surveys, Huchra et al. 1992). One of the first discoveries of our program was that some Ly α absorbers are found in nearby galaxy “voids”, providing the first detection of gas in those voids (Stocke et al. 1995; Shull, Stocke, & Penton 1996). Additionally, the small distances (on the cosmic scale) to these absorbers allow deeper galaxy surveys in the optical and 21 cm emission line, from which the most sensitive limits have been set on the non-detection of galaxies nearby to Ly α clouds (Van Gorkom et al. 1993, 1996; Morris et al. 1993; Rauch, Weymann, & Morris 1996; Shull et al. 1998; Impey, Petry, & Flint 1999). Observations of the latter type led us to investigate strong Ly α systems toward PKS 2155-304 (Shull et al. 1998) with very low metal abundance, which may be among the first detected primordial H I clouds in the local Universe.

The first set of four papers discuss our full GHRS dataset of low column density, low- z Ly α absorption systems. In Paper I (this article) we describe our HST/GHRS observations and catalog of Ly α absorbers. In Paper II (Penton, Shull, & Stocke 2000a) we describe the primary scientific results from our program, including information on the physical parameters mentioned above and

the nature of the low-redshift Ly α forest. In Paper III (Penton, Stocke, & Shull 2000b) we discuss the relationship between the Ly α absorbers discovered in our GHRS program and the nearby galaxy distribution from available galaxy redshift surveys. In Paper IV (Penton, Stocke, & Shull 2000c), we will combine these GHRS observations with results from 13 STIS sightlines to discuss the two-point correlation function of the low- z Ly α forest. These low- z Ly α absorption lines, combined with information about the distribution of nearest galaxies, can probe large-scale baryonic structures (filaments) in the IGM, some of which may be remnants of physical conditions set up during the epoch of galaxy formation.

In this first paper, we describe data from the HST/GHRS of very bright AGNs, which we use to detect low column density ($\log N_{\text{HI}} = 12.5 - 14.5$) Ly α absorption clouds at very low redshift ($z < 0.07$). The GHRS with the G160M grating delivers spectral resolution $R \sim 15,000$. Subsections of this paper describe the target selection and basic observational setup (§ 2), calibration (§ 2.2), spectral processing (§ 2.3), and a thorough description of each sightline (§ 3). This paper concludes with a tabulation of all quantities directly measured from the spectra.

2. HST Observations, Calibration, and Spectral Processing

2.1. HST Observations

To study the local Ly α forest, we used all available HST GHRS/G160M spectra that meet the following simple criteria: (1) Available: public domain GHRS/G160M spectra or our own HST Guest Observer observations, and (2) Appropriate: spectra blueward of the target’s Ly α emission and in the wavelength range 1218–1300 Å ($0.002 < z < 0.069$ for Ly α). The majority of these observations were obtained from our HST Guest Observer projects 3584, 5715, and 6593. We selected our targets based upon two factors: brightness and location in the sky. To determine the brightest targets in the UV, we used the IUEAGN database (Penton, Shull, & Edelson 2000d) to coadd all IUE spectra of AGN to determine the brightest UV targets with appropriate redshifts. We limited our selection to targets with $z_{\text{em}} < 0.18$, to avoid having Ly β appear in our wavelength band of interest (1218–1300 Å), but we required $z_{\text{em}} > 0.025$ to maximize pathlength beyond the region absorbed by the Milky Way interstellar H I. In project 3584 (which carried over into project 5715) we observed 4 objects behind well-studied galaxy voids in the foreground of the “Great Wall” (Stocke et al. 1995; Shull, Stocke, & Penton 1996). In the hope of determining the relationship between galaxies and Ly α absorbers in the low- z universe, we selected this region of the sky where the CfA galaxy redshift surveys were most complete (Huchra et al. 1992; Giovanelli & Haynes 1984). Owing to the lack of sufficiently bright targets in the direction of the first CfA slice, in project 6593 we observed 7 additional targets in other directions. Our sample is rounded out by 5 archival spectra and a few additional exposures on targets that we had already observed. One of our archival targets is at higher z than the above limit ($z=0.297$; H 1821+632) but is also included. In this sightline we take special care to differentiate Ly α lines from other lines, such as Ly β for

$z > 0.19$ absorbers. Recent FUSE observations of several of these sightlines (Shull et al. 2000) detect $\text{Ly}\beta$ corresponding to the stronger $\text{Ly}\alpha$ absorbers, with EWs $> 200 \text{ m}\text{\AA}$. Our survey of low- z $\text{Ly}\alpha$ clouds continues with HST/STIS observations of an additional 13 targets, which will be reported elsewhere.

Table 1 summarizes the HST observations and observational parameters of the forty-one GHRS/G160M exposures towards the 15 targets included in our dataset. The first column in Table 1 identifies the observed target, while the second column lists the HST exposure or dataset identifier. Additional columns provide: (3) the exposure calendar date, (4) whether the COSTAR (Corrective Optics Space Telescope Axial Replacement) optics were in place at the time of the exposure, (5) the exposure time (in seconds), (6 & 7) the wavelength extent of the spectrum, (8) the HST/GHRS wavelength calibration (SPYBAL) exposure used in the calibration of the spectrum, and (9) the HST proposal identification number (PID) and Principal Investigator (PI) of the observation.

Table 2 summarizes the J2000 positions (columns 2-5) and redshifts (z ; column 6) of our HST targets. All redshifts are the optical, narrow-line, emission redshifts as reported from the NASA/IPAC Extragalactic Database (NED).³ Also included in Table 2, but discussed in detail later, are, by column: (7) the Galactic H I velocity centroid relative to the Local Standard of Rest (LSR) along this sightline as determined from the Leiden/Dwingeloo or Parkes multibeam survey, (8) the adjustment required to convert the observed wavelength scale to the LSR, where $\Delta V_{\text{lsr}} = V_{\text{lsr}} - V_{\text{obs}}$, as determined from the location of the S II Galactic absorption lines (1250, 1253, and 1259 \AA , see § 2.3.3) (9) the order (**O**) of the polynomial used to normalize the continuum of each target, (10) the dominant H I 21 cm velocity of the Galactic High Velocity Clouds (HVCs) along each sightline as reported by Wakker & van Woerden (1991), and (11) the mean signal-to-noise ratio (S/N) per resolution element (RE) of each spectrum. The Galactic H I HVC velocities are taken from Wakker & van Woerden (1991), and the Galactic H I LSR velocity measurements are taken from the Leiden/Dwingeloo survey (Hartmann & Burton 1997). Note that Fairall 9, Mrk 335 and PKS 2155-304 are located near the Magellanic Stream (Gibson et al. 2000b), while Mrk 279, Mrk 290, Mrk 501, Mrk 817, and H 1821+643, are close to the HVC complex C (Gibson et al. 2000a). The sightline to Mrk 421 lies between the Galactic HVC MI and MII clouds, and the Mrk 509 sightline passes near the Galactic center negative velocity HVC feature. These objects are therefore more likely to contain Galactic absorption features at velocities other than the LSR.

³The NASA/IPAC Extragalactic Database (NED) is operated by the Jet Propulsion Laboratory, California Institute of Technology, under contract with NASA.

Table 1: HST GHRS/G160M Observations

Target	Dataset	Date	COSTAR Deployed ?	ET (sec)	λ_{start} (Å)	λ_{end} (Å)	Spybal	PID/PI ^a
(1)	(2)	(3)	(4)	(5)	(6)	(7)	(8)	(9)
3C273	z0gu010mn	02/23/91	No	1824.8	1265.430	1301.460	z0gu010nm	1140/WEYMANN
3C273	z0gu010om	02/23/91	No	2737.1	1234.680	1270.790	z0gu010pm	1140/WEYMANN
3C273	z1760105t	11/27/94	Yes	1115.1	1214.110	1250.270	z1760103t	3951/WEYMANN
3C273	z1760107t	11/27/94	Yes	1115.1	1214.130	1250.290	z1760106t	3951/WEYMANN
3C273	z1760108t	11/27/94	Yes	1115.1	1214.130	1250.290	z1760106t	3951/WEYMANN
AKN120	z3e70604t	12/26/96	Yes	5702.4	1222.542	1258.674	z3e70603t	6593/STOCKE
AKN120	z3e70606t	12/26/96	Yes	5702.4	1222.587	1258.707	z3e70605t	6593/STOCKE
AKN120	z3e70608m	12/27/96	Yes	5702.4	1222.609	1258.726	z3e70607t	6593/STOCKE
AKN120	z3e7060at	12/27/96	Yes	2433.0	1222.638	1258.751	z3e70609t	6593/STOCKE
ESO141-G55	z3e70204t	08/15/96	Yes	7248.4	1222.511	1258.638	z3e70203t	6593/STOCKE
ESO141-G55	z3e70206t	08/15/96	Yes	7248.4	1222.542	1258.662	z3e70205t	6593/STOCKE
ESO141-G55	z3i70105t	10/09/96	Yes	9085.0 ^b	1228.710	1265.920	z3i7010ct	6451/SAVAGE
FAIRALL9	z26o0208n	04/09/94	Yes	7096.3	1231.660	1267.750	z26o020at	5300/SAVAGE
FAIRALL9	z3e70404m	08/01/96	Yes	13407.0	1219.702	1255.843	z3e70403t	6593/STOCKE
FAIRALL9	z3e70406t	08/01/96	Yes	6412.0	1240.312	1276.384	z3e70405t	6593/STOCKE
H1821+643	z15f0208m	04/17/93	Yes	6386.7	1231.660	1267.750	z15f0207t	4094/SAVAGE
H1821+643	z27n0108m	04/05/94	Yes	9123.8	1231.660	1267.750	z27n0107t	5299/LU
IZW1	z1a60404n	09/09/93	No	24178.1	1221.401	1257.544	z1a60403t	3584/STOCKE
IZW1	z2ia0204n	02/07/95	Yes	21897.2	1221.299	1257.437	z2ia0203t	5715/STOCKE
MARK279	z3e70304t	01/17/97	Yes	5702.4	1222.537	1258.673	z3e70303t	6593/STOCKE
MARK279	z3e70306t	01/17/97	Yes	5702.4	1222.576	1258.703	z3e70305t	6593/STOCKE
MARK279	z3e70308t	01/17/97	Yes	5702.4	1222.615	1258.737	z3e70307t	6593/STOCKE
MARK279	z3e7030at	01/17/97	Yes	1419.3	1222.643	1258.762	z3e70309t	6593/STOCKE
MARK290	z3kh0104t	01/10/97	Yes	1622.0	1231.760	1268.950	z3kh0103t	6590/WAKKER
MARK290	z3kh0105t	01/10/97	Yes	2433.0	1231.780	1268.970	z3kh0103t	6590/WAKKER
MARK290	z3kh0107t	01/10/97	Yes	2230.3	1231.810	1268.990	z3kh0106t	6590/WAKKER
MARK335	z1a60304n	09/03/93	No	13787.1	1221.408	1257.550	z1a60303t	3584/STOCKE
MARK421	z2ia0104t	02/02/95	Yes	9085.0 ^c	1221.426	1257.569	z2ia0103t	5715/STOCKE
MARK501	z1a65204m	02/28/93	No	29196.3	1221.418	1257.561	z1a65203t	3584/STOCKE
MARK509	z1790208m	05/23/93	No	6082.6	1231.730	1267.840	z1790207t	3463/SAVAGE
MARK509	z3e70704t	10/19/96	Yes	4257.8	1219.468	1255.610	z3e70703t	6593/STOCKE
MARK817	z3e70104t	01/12/97	Yes	8870.4	1222.568	1258.704	z3e70103t	6593/STOCKE
MARK817	z3e70106t	01/12/97	Yes	8236.8	1222.616	1258.741	z3e70105t	6593/STOCKE
MARK817	z3e70108t	01/12/97	Yes	7907.3	1222.645	1258.767	z3e70107t	6593/STOCKE
PKS2155-304	z1aw0106t	05/11/93	No	1558.7	1222.580	1258.700	z1aw0105t	3965/BOGGESS
PKS2155-304	z1aw0107t	05/11/93	No	1558.7	1222.590	1258.710	z1aw0105t	3965/BOGGESS
PKS2155-304	z1aw0108m	05/11/93	No	1520.6	1222.600	1258.720	z1aw0105t	3965/BOGGESS
PKS2155-304	z3e70504t	10/06/96	Yes	3801.6	1257.580	1293.628	z3e70503t	6593/STOCKE
PKS2155-304	z3e70505t	10/06/96	Yes	3168.0	1257.634	1293.669	z3e70503t	6593/STOCKE
Q1230+0115	z3cj0105t	07/11/96	Yes	5474.3	1216.960	1254.200	z3cj0103t	6410/RAUCH
Q1230+0115	z3cj0108t	07/11/96	Yes	5474.3	1217.000	1254.230	z3cj0106t	6410/RAUCH

^aHST Proposal Id number (PID) / HST Principal Investigator (PI).^bAn HST anomaly caused the final exposure to be cut short by 38.8 seconds.^cSubexposures 5 through 15 were unusable due to an HST pointing error. The originally scheduled observation was 14598.1 seconds in length.

Table 2: HST GHRS/G160M Targets

Target	RA (J2000) (hh:mm:ss)	DEC (J2000) (\pm dd:mm:ss)	l ($^{\circ}$)	b ($^{\circ}$)	z	$V_{\text{lsr}}^{\text{a}}$ (H I) (km/s)	$\Delta V_{\text{lsr}}^{\text{b}}$ (km/s)	O ^c	$V_{\text{hvc}}^{\text{d}}$ (km/s)	S/N
(1)	(2)	(3)	(4)	(5)	(6)	(7)	(8)	(9)	(10)	(11)
3C273	12 29 06.8	+02 03 07.8	-70.05	64.36	0.1583	-5	10.5	13	115	27.2
AKN120	05 16 11.4	-00 08 59.4	-158.31	-21.13	0.0331	5	-2.7	14*	-116	22.2
ESO141-G55	19 21 14.3	-58 40 14.9	-21.82	-26.71	0.0371	0	-2.6	20*	200	25.8
FAIRALL9	01 23 45.9	-58 48 20.9	-64.93	-57.83	0.0461	-6	-8.8	20*	190	32.7
H1821+643	18 21 57.1	+64 20 36.7	94.00	27.42	0.2968	-1	46.5	6	-180	20.0
IZW1	00 53 34.9	+12 41 36.3	123.75	-50.17	0.0607	-5	33.3	14	-100	13.2
MARK279	13 53 03.4	+69 18 29.6	115.04	46.86	0.0306	5	50.0	25*	-135	30.0
MARK290	15 35 52.4	+57 54 09.6	91.49	47.95	0.0296	-5	27.9	9*	-120	17.1
MARK335	00 06 19.5	+20 12 10.3	108.76	-41.42	0.0256	-3	30.5	25*	-400	33.3
MARK421	11 04 27.4	+38 12 30.8	179.83	65.03	0.0300	-8	38.2	5	-110	23.9
MARK501	16 53 52.2	+39 45 36.6	63.60	38.86	0.0337	0	55.4	9	-115	15.3
MARK509	20 44 09.8	-10 43 24.5	35.97	-29.86	0.0344	4	15.1	23*	-240	28.4
MARK817	14 36 22.1	+58 47 39.4	100.30	53.48	0.0313	-2	19.6	27*	-115	42.7
PKS2155-304 ^e	21 58 52.0	-30 13 32.3	17.73	-52.25	0.1165	-4	17.5	4	-200	20.3
PKS2155-304 ^f	21 58 52.0	-30 13 32.2	17.73	-52.25	0.1165	-4	3.0	3	-200	34.2
Q1230+0115	12 30 50.0	+01 15 21.7	-68.74	63.66	0.1170	-5	1.1	7	115	9.2

^aThe velocity centroid (in km s^{-1}), relative to the LSR, of the Galactic H I along this sightline as determined from the Leiden/Dwingeloo or Parkes multibeam survey.

^b $\Delta V_{\text{lsr}} = V_{\text{lsr}} - V_{\text{obs}}$, as determined from the location of the S II Galactic lines (1250, 1253, and 1259 \AA).

^cThe order of the polynomial used to normalize the spectrum. An asterisk (*) indicates that a broad Gaussian component was included to model intrinsic Ly α emission, present in the observed band.

^dLSR velocity in km s^{-1} of the dominant HI-HVC in this direction as reported by Wakker & van Woerden (1991).

^eValues for Pre-COSTAR exposure covering 1222–1258 \AA .

^fValues for Post-COSTAR exposure covering 1257–1294 \AA .

2.2. GHRS Calibration

All of our HST/G160M spectra were taken with the Large Science Aperture (LSA) and are a mixture of pre- and post-COSTAR observations as noted in Table 1. All data were re-calibrated with the final GHRS recommendations (Sherbert & Hulbert 1997), using the familiar standard IRAF/STSDAS/CALHRS environment, with the following exceptions:

1. *Background Subtraction:* We find that the null order polynomial (identified in CALHRS nomenclature as **PLY_CORR**) background subtraction gives superior results to the median (**MDF_CORR**) and mean (**MNF_CORR**) background options, mainly due to the inappropriately small size of the default filter box.
2. *Wavelength Calibration:* As listed in Table 1, the indicated GHRS spectrum Y-balances (SPYBAL’s) were used during the recalibration process to correct the initial wavelength zero point offsets.
3. *Blemishes and Degradation Accounting:* To avoid any possible detector artifacts from appearing as weak spectral features, photocathode blemishes, dead, noisy or “flaky” diodes, pixels with Reed-Solomon decoding errors (which indicate possible data transmission errors) are removed from the spectra. For this reason, some spectra have incomplete wavelength coverage, while others have varying S/N ratios across the spectrum.

All subsequent data reductions were performed using the Interactive Data Language (IDL) of Research Systems, Inc (<http://www.rsinc.com>). Because of the low S/N of the individual data files, the subexposure coadditions were performed in wavelength space weighted by exposure time, and not by using the IRAF default STSDAS/CALHRS routines **poffsets** and **specalign**. To achieve this, an exposure time vector was created that defines the actual on-target exposure time for each pixel. The exposure time for each sub-exposure is calculated from the information in the FITS header. Specifically, for each exposure, the following procedure was followed:

1. If the spectra were taken in FP-SPLIT mode, coadd all spectra at identical carousel positions by exposure time.
2. Check the quality of the sub-exposures for anomalies.
3. Recalculate the exposure time from the dataset headers and compare this to the STDSAS/FITS **EXPTIME** header keyword.
4. If the spectral subexposures were not quarter-stepped, resample the spectra to quarter-stepped (quarter GHRS diode) pixels, conserving flux and adjusting the error vectors accordingly.
5. Smooth the spectra to the resolution appropriate for the line-spread function (LSF) of the detector at the time of observation. The pre-COSTAR large science aperture (LSA) line spread

function (LSF) can be represented by a core of Full Width Half Maximum (FWHM)=1.2 diodes ($\sim 20 \text{ km s}^{-1}$ at 1240 \AA) and broad wings (Gilliland & Hulbert 1993). The post-COSTAR GHRS LSF is well-modeled (Gilliland et al. 1992) by a single sharp Gaussian with FWHM=1.1 diodes or $\sim 19 \text{ km s}^{-1}$ in our wavelength range. The smoothing is performed by convolving the LSF of the GHRS/LSA at the time of observation with the flux and error vectors.

Once all the subexposures are in place, we used the following procedure to determine the final spectrum:

1. Use the first subexposure of the first dataset to define the wavelength scale.
2. Populate the final flux, error and exposure time vectors with the first subexposure values, except where any anomaly appears in the calibration flags. Possible anomalies include photocathode blemishes, faulty diodes, and decoding errors as previously described.
3. Coadd the next exposure, weighting by the exposure time in the flux vector. Add the exposure times to the exposure vector. Assume Poisson statistics and combine, in quadrature, the exposure’s 1σ error vector into the merged error vector. The coaddition is performed pixel by pixel into the closest wavelength bin of the first exposure. If no wavelength bin is detected within one-half of a quarter-stepped pixel width, a new wavelength bin is created and populated. This most commonly occurs at the edges of the spectra, as the coverage is extended by multiple observations.
4. Repeat until all exposures of this dataset are merged.
5. If the flux level of the target is constant, or if the temporal separation between observations is small, combine all subexposures of all appropriate datasets to the existing merged exposure. If the flux levels between exposures at different epochs are not constant, then we scale the flux level of the subsequent exposures to the first spectrum for each target listed in Table 1. The error vectors of these exposures are also scaled to preserve the proper S/N weighting. The scaling is determined by the average fluxes in the overlap region of the exposures. For ESO 141-G55 (HST exposure z3i70105t), Markarian 509 (HST exposure z3e70704t), and Fairall 9 (HST exposures z3e70404m and z3e70406t), we allow a scaling that varies linearly across the overlap region to compensate for any “Baldwin Effect”.⁴ For PKS 2155-304, the pre- and post-COSTAR observations covered different wavelength ranges and are analyzed separately.

⁴The “Baldwin Effect”, first noted in Baldwin (1977), pertains to the observed systematic decrease of the equivalent width of AGN line emission (e.g., $\text{Ly}\alpha$) with an increase in continuum luminosity. This changes the continuum slope in the vicinity of the $\text{Ly}\alpha$ emission in the indicated spectra.

2.3. Spectral Processing

2.3.1. Line Identification: Local Continuum Method and b -values

To begin the spectral processing, we treat all spectral fluctuations with $> 1\sigma$ negative departures from the continuum as our initial absorption line list. Linear continuum and Gaussian features (with observed Doppler velocities constrained in the range of $12 < b_{\text{obs}} < 100 \text{ km s}^{-1}$) are fitted to a 4 \AA region centered on prominent features. This wide range of b -values allows us to include all possible absorption lines in these spectra. Gaussian features are fitted to the functional form, $\exp [-(\lambda - \lambda_c)^2 / 2\Delta\lambda_D^2]$, where λ_c is the line center and the observed Doppler widths (b_{obs}) are related to the Gaussian widths by $\mathbf{W}_G = b_{\text{obs}}/\sqrt{2}$, and $\Delta\lambda_D = (\lambda/c)\mathbf{W}_G$. The Ly α b -value is related to the physical properties of the absorbing gas by :

$$b = \sqrt{\frac{2kT}{m_p} + V_{\text{turb}}^2} = \sqrt{V_{\text{therm}}^2 + V_{\text{turb}}^2} \quad , \quad (1)$$

where T is the temperature of the cloud, m_p is the proton mass, k is the Boltzmann constant, and V_{turb} represents non-thermal turbulent motion of the absorbing gas. We selected Gaussian components because, at the spectral resolution and S/N of these observations, we are unable to distinguish between Gaussian and Voigt line profiles at high confidence level, and at the column densities that we are sampling, Gaussian and Lorentzian profiles are virtually indistinguishable. In addition it is unclear whether we are resolving discrete individual absorption clouds or nondiscrete ensembles of neutral hydrogen spread in velocity space. Up to 10 Gaussian components are fitted simultaneously to each region of interest, with features taken from the initial line list. If more than 10 Gaussian components are required, or if the continuum is non-linear, we decrease the wavelength region accordingly until the fitting can proceed. When we encounter obvious asymmetries, features broader than $b_{\text{obs}}=100 \text{ km s}^{-1}$, or distinct absorption minima, we count them as additional features and add them to the line list.

We repeat this procedure of adding Gaussian components and refitting all features when we encounter an absorption feature broader than 100 km s^{-1} , until all modeled features have $b_{\text{obs}} < 100 \text{ km s}^{-1}$. Occasionally, we relax this limit to allow strong intrinsic and Galactic features to have $b_{\text{obs}} = 100 \text{ km s}^{-1}$. This minimizes the number of components in exceptionally broad features that are almost certainly not intervening absorptions. Although we allow absorption features with $b_{\text{obs}} \leq 12 \text{ km s}^{-1}$ to remain in the initial absorption line list, they are removed after we perform a continuum normalization, or by our selection of a $\geq 3\sigma$ significance cutoff. In addition, we observe broad low-contrast absorption troughs ($b_{\text{obs}} > 100 \text{ km s}^{-1}$) in some of the low S/N spectra. We interpret these as continuum features, detector artifacts, or possible nondiscrete absorption features. In these cases, we fit the troughs with Gaussians to maintain the continuum integrity, but we do not count them as Ly α absorption features.

We express the strength of an absorption feature in terms of its observed equivalent width (EW) in m \AA . An accurate determination of the EW depends on an accurate modelling of the

continuum level in the absence of any absorption. For the majority of this paper, we are interested in the rest-frame equivalent widths, $\mathcal{W} = \text{EW}/(1+z)$. We quote \mathcal{W} in all Tables. However we often use the abbreviation EW in contexts where the difference between observed and rest-frame values are unimportant. We calculate the significance level (SL) of each potential absorber by integrating the S/N per 19 km s^{-1} FWHM resolution element (RE) of the best-fit Gaussian. This SL is different (usually larger) than that indicated by the uncertainty in \mathcal{W} , which is derived from the uncertainties of the best-fit Gaussian components. Features with $SL \geq 4\sigma$ are termed “definite” absorbers, while features with $3\sigma \leq SL < 4\sigma$ are termed “possible” absorbers. The continuum and absorption feature fits are performed in IDL using a Levenberg-Marquardt χ^2 minimization implementation based on MINPACK-1 (Moré & Wright 1993; Markwardt 1999).

The measured b -values are independent of the EW measurements and are important determinations in their own right. These are the first b -value measurements published at low- z , and are essential for converting \mathcal{W} to column density in higher column density absorbers. To obtain b -values, the measured Gaussian widths (\mathbf{W}_G) are deconvolved using the **smoothed** LSFs of the pre- and post-COSTAR data (as appropriate) since the data themselves have been smoothed as described in the previous section. In the limit of very high S/N data, this smoothing could decrease our ability to determine accurate b -values for very narrow features. But, for the modest S/N present in the current data, two effects “trade-off” against each other to make small b -values equally accurate in smoothed and unsmoothed data: The error inherent in fitting the data with a Gaussian and the error in determining whether that Gaussian is distinctly broader than the LSF. We see no evidence that smoothing these data have made it more difficult to measure very narrow b -values; indeed a couple of b -values at $\leq 15 \text{ km s}^{-1}$ are found. As Lu et al. (1996) have pointed out on the basis of simulations using moderate S/N ratio spectra, these very low- z b -values have large errors and are underestimates of the true line widths due to the presence of noise. Specifically, since the data are inherently smeared by the instrumental profile, and by our smoothing, both with $\sigma_{\text{gauss}} \sim 8.07 \text{ km s}^{-1}$, our measured b -values are related to our smoothed observed b -values ($b_{\text{obs}} = \sqrt{2} \mathbf{W}_G$) by:

$$b = \sqrt{2} \sqrt{\mathbf{W}_G^2 - 2 \times (8.07 \text{ km s}^{-1})^2} = \sqrt{b_{\text{obs}}^2 - (16.14 \text{ km s}^{-1})^2}. \quad (2)$$

As discussed in Paper II, the measured b -values in pre-COSTAR data are occasionally artificially large due to spacecraft “jitter”. In all Tables reporting b -values, we always list the b -values corrected by equation 2 above.

2.3.2. Continuum Normalization: Global Continuum Method

Because a major source of uncertainty in all EW determinations is the continuum placement, we also performed a global continuum normalization to give two independent estimates (“local” vs. “global”) of the continuum placement. We used polynomial fits to model a global continuum and normalize each spectrum. The order of the continuum-fitting polynomial was selected by

performing F-tests on increasing polynomial orders until adding an additional order is not justified (Mandel 1984). For each spectra, the order of the normalizing polynomial is indicated in Table 2 and is restricted to be less than 30. For objects with broad intrinsic Ly α emission (Akn 120, ESO 141-G55, Fairall 9, Mrk 279, Mrk 290, Mrk 335, Mrk 509, and Mrk 817), we include a single Gaussian to improve the continuum fit near the emission feature. The continuum fits are made on the raw data, with $3\times\text{FWHM}$ (Full Width at Half Maximum) regions centered on each 3σ absorption feature replaced by continuum estimates plus added Gaussian noise. Including noise in the replaced spectral regions was necessary to avoid biasing the global continuum modeling. The unnormalized spectra of each target and the polynomial fits are shown in the spectral plots (Appendix A).

From the difference in the measured values of EW obtained from the “local” and “global” continuum methods, we conservatively overestimate the contribution of the continuum uncertainty to the EW and significance level (SL) determinations. In Figure 1, we compare the deviations of EWs using the local continuum fits from the global continuum results. The differences are well-fitted by a Gaussian with a HWHM (half width at half maximum) of 1.1%. Taking this value to be the 1σ error estimate, we conservatively add a 3σ (3.4%) additional continuum placement uncertainty in quadrature with the statistical uncertainties of the EW, and hence the significance levels, of all features. Note that this systematic continuum placement error is an additional uncertainty above and beyond the statistical uncertainty of absorption feature plus continuum included in the error estimates. Although it is clear from Figure 1 that our continuum normalization correction is a considerable overestimate for most absorption features, a few words are needed to explain the “outliers” at $> 10\%$ difference in Figure 1. These outliers occur mostly from blended lines or clustered absorption features located on the wings of significant continuum features, such as the target’s Ly α emission. Multi-component fits of blended absorption lines find a χ^2 solution that shares the EW between the absorption components. This increases the uncertainty in determining the EW of the individual blended components, but not the total EW. Even slight continuum adjustments can significantly alter the EW absorption ratio between the blended features, while leaving the total absorption almost unchanged. This produces outliers in Figure 1 that are not associated with the continuum normalization error, but rather arise from special individual circumstances. Hence, our procedure does not underestimate the total errors for these outlier features. Indeed, because a continuum placement error is rarely included in the error budget for absorption-line EWs, we have been conservative, but we believe correct, in including this additional uncertainty.

2.3.3. Wavelength Adjustment to Local Standard of Rest (LSR)

Once all features have been modeled, we use the wavelength of the strongest components of the Galactic S II triplet, 1250.584 Å, 1253.811 Å, 1259.519 Å to determine the offset $\Delta V_{\text{lsr}} = (V_{\text{lsr}} - V_{\text{obs}})$ that can be applied to adjust the observed, approximately heliocentric, wavelength scale of the GHRS spectra to the LSR frame. These adjustments are given in column 10 of Table 2. This

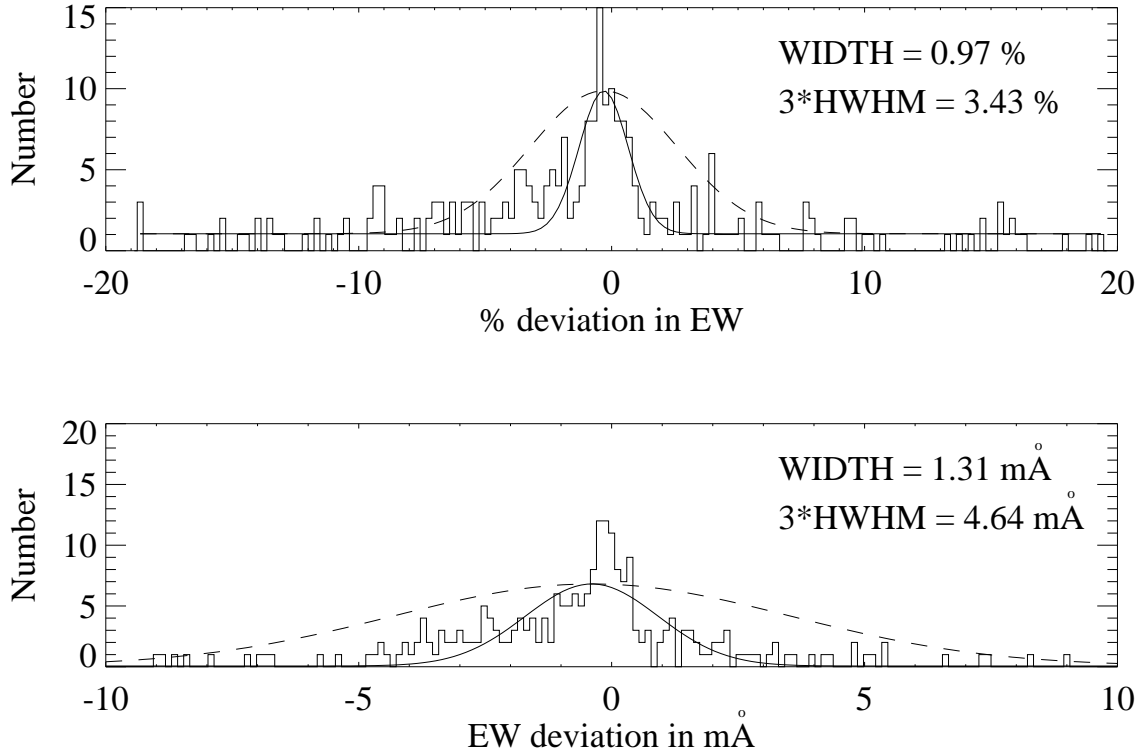


Fig. 1.— The upper panel shows the percent deviation in absorption feature EWs of the “local” continuum determinations versus the “global” determinations. WIDTH indicates the width of the Gaussian that best fits the distribution (shown as a solid curve). The dashed curve represents a Gaussian with a width of $3 \times$ the HWHM (half width at half maximum) of the best-fit distribution. This 3σ deviation represents the additional systematic EW uncertainty introduced in the spectral normalization. The bottom panel shows the same deviations in units of mÅ.

technique assumes that the S II lines occur at the same LSR velocity as the dominant component of the Galactic H I, determined from the Leiden/Dwingeloo survey (Hartmann & Burton 1997) for all objects except Fairall 9 and ESO 141-G55. For these two objects, the Galactic H I velocities relative to the LSR were determined from the Parkes multibeam survey (Haynes et al. 1999).

The Galactic H I velocities relative to the LSR along each sightline are given in column 9 of Table 2. It is our opinion that this LSR-corrected wavelength scale is more accurate than the heliocentric scale provided by the GHRS recalibration because the precise location of the target in the LSA is unknown. Owing to target motion in the LSA, pre-COSTAR observations can have velocity offsets as large as 70 km s^{-1} ($1''$ in the LSA), while post-COSTAR observations can have velocity offsets as large as 60 km s^{-1} ($0.85''$ in the LSA). As described in the HST Data Handbook⁵, there are a number of other effects, such as thermal motion, that can significantly affect the wavelength scale of an observation. By consistently applying our LSR adjustment, we obtain a more precise wavelength scale. We estimate that the accuracy with which H I and S II velocities can be matched is $\pm 5 \text{ km s}^{-1}$, limited by the width and structure of the H I 21 cm profile. This amount of velocity uncertainty is added in quadrature to the individual uncertainties of the features based upon the Gaussian fits. This total velocity uncertainty of individual absorption features is $\leq 10 \text{ km s}^{-1}$, and it is this total value which is listed in all tables. Column 8 of Table 2 lists these velocity offsets for each target.

We construct the final line list by refitting all features in the manner described above in the normalized (“global” continuum method) LSR. We use the Gaussian centers, heights, and widths (\mathbf{W}_G , related to the b -value) from the “local” continuum method as the initial values for the final χ^2 “global continuum” minimization to determine the final line lists. As described above, we determine the statistical significances of all lines using an error estimate that includes both the statistical error in the χ^2 fitting technique and the systematic error associated with continuum placement.

2.3.4. Galactic Spectral Features

The 1218–1300 Å range contains only a few strong Galactic interstellar lines (see Table 3, Morton 1991). These lines, although useful for correcting the wavelength scale to LSR, also eliminate a small portion of our available pathlength for Ly α detection. A full discussion of the pathlength availability appears in Appendix A. Table 3 lists the rest wavelength for each of the Galactic lines in our waveband, as well as $\log(\lambda f)$ and λf . Unsaturated lines of the same species and ionization state are expected to have EW ratios that match the λf ratios. For example, N V $\lambda 1238$ and $\lambda 1242$ are expected to have EWs in the ratio of 2:1. These ratios allow for distinction between Galactic absorption and intervening Ly α absorption at expected Galactic line positions. For many of these features, the appearance of multiple lines of the same species in our waveband allows us

⁵Version 3.1: March 1998, Section 37.6.5, “Wavelength Data Uncertainty”, available from <http://www.stsci.edu>.

to identify Galactic features based upon expected wavelengths and strengths. These features are denoted by a “**g**” in the line lists. Since highly ionized species may have different velocities within our Galaxy, we allow an offset of up to 0.2 \AA ($\sim 50 \text{ km s}^{-1}$) for definite ($SL \geq 4\sigma$) Galactic feature identifications. Possible ($3\sigma \leq SL < 4\sigma$) Galactic identifications are allowed a larger offset range up to 0.5 \AA ($\sim 120 \text{ km s}^{-1}$) and are denoted by a question mark in the line identifications.

Often, Galactic absorption is detected at velocities other than the LSR, due to well-known high-velocity clouds (HVCs) within our Galaxy. These detections are indicated by a “**h**” in the identification field of our line lists. Our observations are unique in that they are able to place upper limits on metallicity of the HVCs in several species, Mg II, S II, and, in some cases, Si II. Individual detections of HVCs will be reported both in the line lists and in later sections. A detailed analysis of the HVC results toward Complex C and the Magellanic Stream will appear elsewhere (Gibson et al. 2000a,b).

Galactic and HVC absorption lines remove a portion of our available pathlength for Ly α detection. At the location of each definite, or possible, Galactic and HVC absorption line, we remove a portion of the spectrum equal to the FWHM of the absorption feature on each side of the identified line center. We suspect that occasional weak intervening Ly α features are superimposed upon Galactic/HVC features. However, if we cannot conclusively determine this occurrence based upon expected line strengths, we consider the superimposed portion of the spectrum unusable for Ly α detection. In such cases, we report the total absorption as Galactic/HVC and remove this portion of the available pathlength for intervening Ly α detection.

2.3.5. *Intrinsic, Intergalactic, and Non-Ly α Absorbers*

Many AGN are observed to possess “intrinsic” absorbers at $z_{\text{abs}} \sim z_{\text{em}}$. One measure of the appropriateness for excluding potential intrinsic absorption systems from our line list is the “Proximity Effect” (Bajtlik & Ostriker 1988) or “Inverse Effect” (Murdoch et al. 1986), which refer to the observed decrease of absorption line density, dN/dz , when approaching the target AGN’s emission redshift. This decrease has been interpreted as due to increased photoionization of the absorption-line systems by the target AGN’s UV radiation field (Carswell et al. 1982). To avoid any possible skewing of our statistics by this effect, we include only absorption systems in which the ionizing radiation from the target AGN is 10% or less of the metagalactic ionization radiation field. At low redshift, the metagalactic ionizing intensity at 912 \AA has been estimated to be $I_0 = 1.3^{+0.8}_{-0.5} \times 10^{-23} \text{ ergs cm}^{-2} \text{ s}^{-1} \text{ Hz}^{-1} \text{ sr}^{-1}$ (Shull et al. 1999b). Assuming that the mean value of the specific ionizing luminosity at 912 \AA from the IUEAGN database, $L_{912} = 6 \times 10^{29} \text{ erg s}^{-1} \text{ Hz}^{-1}$, is representative of our HST targets, we can calculate the “standoff” distance (D) from the target QSO at which the QSO’s ionizing flux decreases to $I_0/10$:

$$\frac{L_{912}}{(4\pi D^2)4\pi} = \frac{I_0}{10} \Rightarrow D = \frac{1}{4\pi} \sqrt{\frac{10 L_{912}}{I_0}} = 17.5 h_{70}^{-1} \text{ Mpc}, \quad (3)$$

which is equivalent to $cz \approx 1,200 \text{ km s}^{-1}$, where h_{70} is the Hubble constant in units of $70 \text{ km s}^{-1} \text{ Mpc}^{-1}$.

Therefore, we consider non-Galactic absorption features within $1,200 \text{ km s}^{-1}$ of the redshift of the target to be either $\text{Ly}\alpha$ clouds near the AGN affected by the “proximity effect” or intrinsic absorption near the target. For consistency, we will use the term “intrinsic” for all $\text{Ly}\alpha$ absorptions within $1,200 \text{ km s}^{-1}$ of the target, or metal lines associated with the target AGN. Lines identified as $\text{Ly}\alpha$ outside of this limit will be termed “intergalactic”. Non- $\text{Ly}\alpha$ lines associated with known higher- z systems, such as in H 1821+643, will be termed “non- $\text{Ly}\alpha$ ” absorbers.

Lines intrinsic to the target AGN are not included in any of our low- z $\text{Ly}\alpha$ forest statistics and are marked by an “i:” prefix in the identification fields of the target line lists. Likewise, the pathlength within $1,200 \text{ km s}^{-1}$ of the AGN is excluded from our total observed pathlength. Our choice of a $1,200 \text{ km s}^{-1}$ radial velocity limit relative to the target (V_r) limit is supported by the analysis of intrinsic absorption lines in Seyfert 1 galaxies by Crenshaw et al. (1999). In Figure 2, we display this sample, obtained from ultraviolet HST/FOS and GHRS $\text{Ly}\alpha$, C IV $\lambda\lambda 1548, 1550$, N V $\lambda\lambda 1238, 1242$, and S IV $\lambda\lambda 1393, 1402$ detections, in terms of number (N) of intrinsic systems versus V_r . Five of the 17 targets in Crenshaw et al. (1999) are also in our sample. As shown by the vertical line at $-1,200 \text{ km s}^{-1}$ in Figure 2, our radial velocity limit includes the vast majority, but not quite all, of the detected intrinsic systems. These results support the claim that our blueward velocity limit is reasonable, but not perfect, in protecting against any outflowing “intrinsic” absorbers associated with the target. In Figure 3, we plot $|V_r|$ versus rest-frame EW (\mathcal{W}) for all $\text{Ly}\alpha$ absorbers in our sample with $|V_r| < 5,000 \text{ km s}^{-1}$. Notice that several absorbers with $|V_r| < 1,200 \text{ km s}^{-1}$ have $\mathcal{W} > 200 \text{ m}\text{\AA}$, while only one of the absorbers identified as intergalactic has $\mathcal{W} > 200 \text{ m}\text{\AA}$. This further supports our assumption that a $1,200 \text{ km s}^{-1}$ blueward velocity limit accounts for the majority of intrinsic or outflowing absorbers. In terms of pure Hubble flow distance, this blueward velocity limit is well in excess of the $230 h_{70}^{-1} \text{ kpc}$ galactic halo size inferred by Lanzetta et al. (1995), and probably eliminates any possible $\text{Ly}\alpha$ absorptions associated with the targets.

We stress that any velocity limit that purports to separate intergalactic from intrinsic systems is somewhat uncertain. While we have presented several pieces of evidence that $1,200 \text{ km s}^{-1}$ is a reasonable velocity limit, it is impossible unambiguously to classify any individual $\text{Ly}\alpha$ absorber as either intrinsic or intergalactic. Any use of the intrinsic or intergalactic line lists must take this uncertainty into account.

A few of our targets, such as H 1821+643, have known intergalactic $\text{Ly}\alpha$ absorption systems with redshifts greater than our survey cutoff. Higher Lyman series lines or metal-line absorptions associated with these systems that fall within our wavelength range ($1218\text{--}1300 \text{ \AA}$) are termed “non- $\text{Ly}\alpha$ ”. These features are indicated by a “z:” in the identification field of the line lists. As with the intrinsic features, these features are not included in any of our low- z $\text{Ly}\alpha$ forest statistics. Additionally, the pathlength obscured by these features is excluded from the available pathlength

for Ly α detection using the same method as the Galactic/HVC features.

3. Results by Object

In this section, the observations of each target are discussed in detail. Composite spectra (Figures 5–20) and a spectral line identification table (Table 9) appear in Appendix A, for our sightlines in the same order presented here. The wavelength scales have been corrected to the LSR by equating the Galactic H I LSR velocity in each sightline (Table 2, column 7) with the location of the S II $\lambda\lambda$ 1250, 1253, 1259 Galactic interstellar lines in the observed waveband. To provide an overall sense of the number and strength of our detections, as well as the quality of our spectra, Figure 4 shows the number of reported intergalactic Ly α absorbers as a function of significance level (SL).

3.1. 3C 273

The sightline to 3C 273 is perhaps the most studied of all low- z QSO targets (Bahcall et al. 1991a,b, 1993; Brandt et al. 1993, 1997; Morris et al. 1991, 1993; Weymann et al. 1995). Morris et al. (1993) provide a summary of all HST spectra available as of 1993, including those observed with the GHRS+G160M, GHRS+G140L, and FOS+G130. Refitting all features with their JASON software, Morris et al. (1993) report 12 features in our wavelength range of interest ($z < 0.07$). Our spectrum combines the two GHRS G160M spectra summarized in Morris et al. (1993) with three additional 1218–1250 Å spectra obtained in 1994 (see Table 1). This results in a 1218–1300 Å spectrum shown in Figure 5, the only one in our sample that covers our entire spectral range of interest. Our analysis of these spectra, recalibrated as discussed earlier, reveals 18 Ly α absorption features at $SL \geq 3\sigma$, of which 13 have $SL \geq 4\sigma$. Our results differ from those of Morris et al. (1993) in the following regards:

1. At $\lambda \approx 1224.2\text{--}1225.0$ Å we see a broad absorption trough at the red edge of the Galactic damped Ly α line that we model with two Ly α absorption features greater than 4σ totalling ~ 64 mÅ. Bahcall et al. (1991a) report a 240 mÅ feature at 1224.52 Å, while Bahcall et al. (1993), Brandt et al. (1993), and Bahcall et al. (1991b) do not report this feature.
2. The 1280.3 Å feature (not given in any other line lists) was determined to be a Ly α absorber, not Galactic C I λ 1280, owing to the absence of the expected C I λ 1277 in our spectrum.

Also detected along this sightline are the Galactic features Mg II λ 1239.9, N V $\lambda\lambda$ 1238, 1242, S II $\lambda\lambda$ 1250, 1253, 1259, and Si II λ 1260.4 + Fe II λ 1260.5 (which is possibly blended with C I λ 1260). Based upon the absence of a Mg II λ 1240.4 detection, it is possible that the 1240.01 Å detection could be Ly α instead of the reported Mg II λ 1239.9.

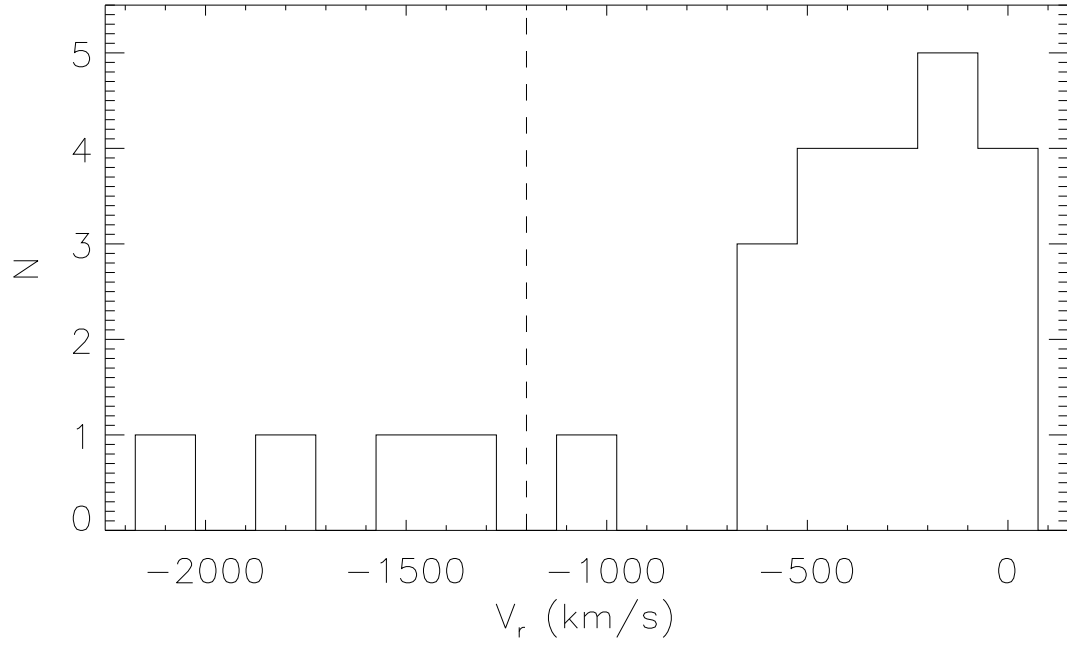


Fig. 2.— Radial velocity distribution relative to the target (V_r in km s^{-1}) of the HST UV sample of Seyfert 1 galaxy “intrinsic” absorbers presented by Crenshaw et al. (1999). The dashed vertical line at $-1,200 \text{ km s}^{-1}$ indicates our blueward radial velocity limit for determining which $\text{Ly}\alpha$ features are intrinsic or “associated” with the target.

Table 3. Galactic Lines

Ion	Wavelength (Å)	$\log(\lambda f)$	λf
N V	1238.821	2.289	194.54
Mg II	1239.925	-0.106	0.784
Mg II	1240.395	-0.355	0.442
N V	1242.804	1.988	97.28
S II	1250.583	0.834	6.82
S II	1253.811	1.135	13.65
S II	1259.519	1.311	20.46
Si II	1260.422	3.104	1270.57
Fe II	1260.533	1.499	31.55
C I	1260.736	1.696	49.66
C I	1277.245	2.091	123.31
C I	1280.135	1.493	31.12

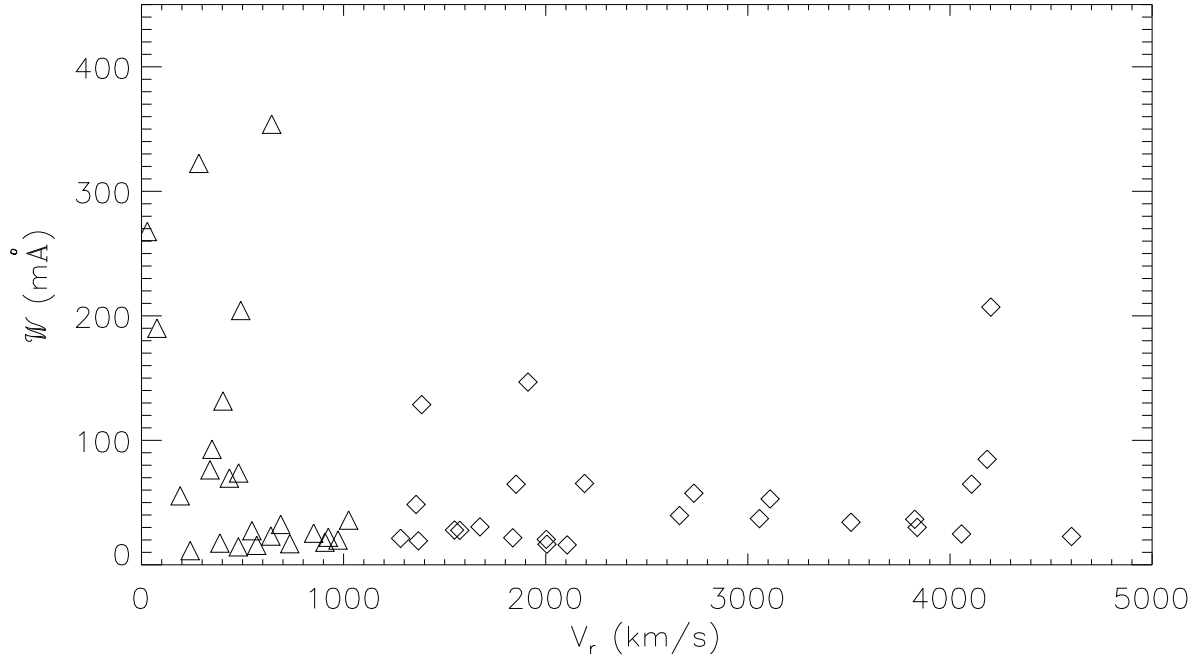


Fig. 3.— Distribution of rest-frame EW (\mathcal{W}) versus radial velocity relative to target ($|V_r|$ in km s^{-1}) of our sample. The triangle absorbers are those determined by our criterion to be intrinsic ($|V_r| < 1,200 \text{ km s}^{-1}$), while the diamonds indicate intergalactic $\text{Ly}\alpha$ absorbers.

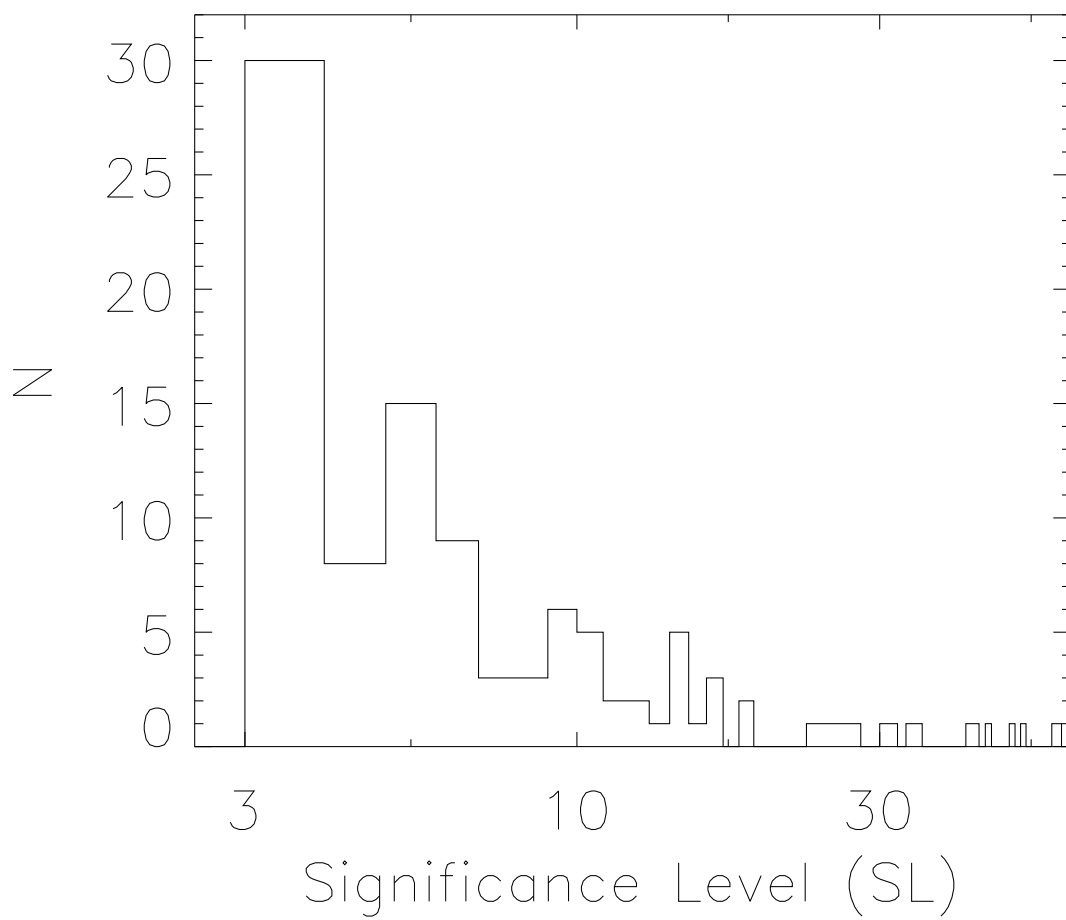


Fig. 4.— Significance level (SL) distribution of our detected intergalactic Ly α absorbers.

As discussed in Sembach & Savage (1996) and Burks et al. (1994), the sightline towards 3C 273 passes through the edges of Galactic radio loops I and IV near the North Polar Spur (l, b)=(290°, 64.4°) and near the Sagittarius spiral arm. Although no HVCs are reported in this direction, we do detect Galactic N V λ 1238, S II $\lambda\lambda$ 1250, 1253, 1259, and Si II λ 1260.4 + Fe II λ 1260.5 at infalling velocities up to 50 km s⁻¹. This is most prevalent in the peculiarly shaped N V λ 1242 absorption.

In Weymann et al. (1995), the 1220 Å and 1222 Å Ly α features were measured to have b -values of 40.7 ± 3.0 km s⁻¹ and 34.3 ± 3.3 km s⁻¹, respectively. They analyzed the same GHRS observations as we did, using Voigt profile fitting on spectra that were carefully cross-correlated at the subexposure level. We elected not to include such cross-correlations in our standard data reduction because the vast majority of our GHRS subexposures were of insufficient S/N to accomplish this procedure with confidence. Positional shifts of the target in the HST aperture can cause sub-diode spectral shifts in the subexposures. This causes us occasionally to overestimate the b -values of the absorption features, but it does not affect our measurements of the centers, EWs, or significance levels of the absorption features. The consequences of this drift on our measured b -values will be explored in Paper II. The LSR offset for this spectrum was 0.044 Å or 10.5 km s⁻¹ at 1253 Å.

3.2. Akn 120

The spectrum of Akn 120 (Arakelian 120, also known as Mrk 1095) covers 1223 to 1259 Å and has an average S/N per resolution element of 22. Our spectrum of Akn 120 contains 5 definite and 2 possible Ly α absorbers, one intrinsic Ly α absorption, and strong Galactic detections in Mg II $\lambda\lambda$ 1239.9, 1240.4, S II $\lambda\lambda$ 1250, 1253, and N V λ 1238. Based upon only a 0.9σ detection of N V λ 1242, it appears that N V λ 1238 (which appears extremely broad) is partially contaminated by an intergalactic Ly α system. The 0.9σ N V λ 1242 feature is below our limit for inclusion. N V λ 1242 is listed as the alternate identification for the 1242.9 Å Ly α feature because its spectral proximity falls within our generous limits (§ 2.3.4). However, due to the strength of the 1242.9 Å feature, we are confident of the identification as Ly α . Of special note is the well-resolved and closely spaced ($\Delta v = 60$ km s⁻¹) pair of strong Ly α absorbers at 7960 and 8020 km s⁻¹. This pair is flanked to the blueward by two additional $\sim 4\sigma$ absorbers at 7792 and 7867 km s⁻¹. The dominant HVC H I velocity, relative to the LSR, in this direction (Wakker & van Woerden 1991) is -116 km s⁻¹. We not detect this HVC in any of the Galactic lines in our waveband. For S II $\lambda\lambda$ 1250, 1253, we do not detect this HVC at the 4σ \mathcal{W} limit of 20 mÅ. The Akn 120 sightline was corrected to the LSR using the Galactic H I and only two S II lines (1250, 1253 Å). The LSR offset for this spectrum was -0.011 Å or -2.7 km s⁻¹ at 1253 Å.

3.3. ESO 141-G55

Our spectrum of ESO 141-G55 contains no definite absorbers and only one possible intergalactic Ly α absorber. This spectrum has a good S/N (~ 26 per RE), so that we are sensitive to 4σ Ly α absorptions below 40 mÅ for a large portion of the spectrum. This sightline does contain strong Galactic N V $\lambda\lambda 1238, 1242$, Mg II $\lambda\lambda 1239.9, 1240.4$, S II $\lambda\lambda 1250, 1253, 1259$, and Si II $\lambda 1260.4 + \text{Fe II } \lambda 1260.5$. We also detect an HVC at $V_{\text{lsr}} \cong -65 \text{ km s}^{-1}$ in S II $\lambda\lambda 1250, 1253, 1259$, Si II $\lambda 1260.4 + \text{Fe II } \lambda 1260.5$, and possibly N V $\lambda\lambda 1238, 1242$ (1.7σ and 1.4σ respectively). We also detect a very strong intrinsic Ly α absorption at 1258 Å, or $V_{\text{lsr}} \cong -640 \text{ km s}^{-1}$ relative to ESO 141-G55. This sightline does not pass through any known radio loops or Galactic H I-HVCs. The flux level of the z3i70105t HST exposure was scaled to be consistent with the other ESO 141-G55 exposures (see Table 1). The scaling was applied linearly across the overlap region with the other exposures to compensate for a noticeable “Baldwin Effect” between exposures. The LSR offset for this spectrum was -0.011 Å or -2.6 km s^{-1} at 1253 Å.

3.4. FAIRALL 9

We detect 8 definite, 1 possible, and 6 intrinsic Ly α absorption features in our spectrum of Fairall 9. The spectrum of Fairall 9 includes 3 separate post-COSTAR exposures, one of which was reported in Lu, Savage, & Sembach (1994). The two additional exposures were obtained in 1996, two years after our first exposure. The additional exposures allow us to confirm and refine the earlier results on both the Ly α absorptions and the Galactic/HVC absorptions. The flux levels of the additional HST/G160M exposures, z3e70404m and z3e70406t, were scaled to be consistent with the initial Fairall 9 exposure. The scaling was applied linearly across the overlap region with the initial exposure. The feature identified as N V $\lambda 1238.8$ in Table 9, is probably blended with a Ly α feature based upon the marginal 1.8σ ($\mathcal{W} = 8 \pm 6 \text{ mÅ}$) detection of N V $\lambda 1242$. Given the expected 2:1 ratio of these Galactic absorption features, the $48 \pm 11 \text{ mÅ}$ absorption feature at 1238.8 Å is anomalously strong and asymmetric. However, given the uncertainty in determining the relative strength and b -value for the possible Ly α absorption, we have chosen to exclude this feature and the associated pathlength from our Ly α survey.

The Fairall 9 sightline passes through the Magellanic Stream (MS), which is detected in our waveband (1220–1276 Å) in Si II $\lambda 1260.4 + \text{Fe II } \lambda 1260.5$ and S II $\lambda\lambda 1250, 1253$. In addition, the Galactic Si II $\lambda 1260.4 + \text{Fe II } \lambda 1260.5$ absorption feature appears to be blended with a MS S II $\lambda 1259$ absorption. H I 21 cm emission (Morras 1983) reveals two high velocity MS components at $\sim 160 \text{ km s}^{-1}$ ($N_{\text{HI}} \sim 2 \times 10^{19} \text{ cm}^{-2}$) and 200 km s^{-1} ($N_{\text{HI}} \sim 6 \times 10^{19} \text{ cm}^{-2}$). Lu, Savage, & Sembach (1994) report two high velocity components of Si II $\lambda 1526$ at $+170 \text{ km s}^{-1}$ and $+200 \text{ km s}^{-1}$. In our S II $\lambda\lambda 1250, 1253, 1259$ detections of the MS, we are unable to resolve the MS clearly into separate components. Savage, Sembach, & Lu (1997) report detection of this HVC in Si II $\lambda 1260.4 + \text{Fe II } \lambda 1260.5$. We confirm this detection centered at $+180 \text{ km s}^{-1}$ and

covering the range $+100$ to $+260$ km s^{-1} . We were able to model this absorption with two features centered at $V_{\text{lsr}} = +128$ km s^{-1} and $+190$ km s^{-1} . We do not detect the MS in N V $\lambda\lambda 1238, 1242$ or in Mg II $\lambda\lambda 1239.9, 1240.4$ at the 10 mÅ level. Assuming that the MS S II $\lambda\lambda 1250, 1253$ absorption features are on the linear portion of the curve of growth, (Gibson et al. 2000b) find a MS metallicity of $[\text{S}/\text{H}] = -0.52 \pm 0.04$. This compares to the LMC and SMC values of -0.57 ± 0.09 and -0.68 ± 0.15 , respectively (Russell & Dopita 1992).

While several absorbers are detected in the wavelength range 1262–1266 Å, the rapidly rising continuum on the blue wing of Ly α calls their reality into question. Specifically, due to our concerns about the reality of these features, we have refit the continuum for Fairall 9 by altering the order of the global fit significantly. The statistical significances of these features remains robust despite these changes, so we list them as definite or possible Ly α features as shown in Figure 8.

The z3e70404m exposure of Fairall 9 contains a “medium” photocathode blemish in the 1254–1256 Å range. This blemish, combined with the coaddition of multiple exposures with different wavelength ranges, produces a notch in the sensitivity detection limit near 1255 Å. The LSR offset for this spectrum was -0.037 Å or -8.8 km s^{-1} at 1253 Å.

3.5. H1821+643

The GHRs/G160M spectrum of H 1821+643 (as known as QSO E1821+643) covers 1231.66–1267.75 Å or $0.01315 < z < 0.04284$. In this spectrum, we detect five definite and seven possible Ly α lines, along with very strong Galactic N V $\lambda\lambda 1238, 1242$ and Mg II $\lambda\lambda 1239.9, 1240.4$. Savage, Sembach, & Lu (1995) report C IV-HVCs along this sightline at $V_{\text{lsr}} = -70, -120$, and -213 km s^{-1} with column densities of $N_{\text{CIV}} = 6, 6$ and 1×10^{13} cm^2 , respectively. We detect the $V_{\text{lsr}} = -70$ km s^{-1} component in N V $\lambda 1238$ and S II $\lambda 1250$, and the $V_{\text{lsr}} = -120$ km s^{-1} component in S II $\lambda\lambda 1253, 1259$, and Si II $\lambda 1260.4$ + Fe II $\lambda 1260.5$. The individual detection of the -70 and -120 km s^{-1} components is complicated by their spectral proximity. The LSR offset for this spectrum was 0.187 Å or 44.7 km s^{-1} at 1253 Å.

Many Ly α lines outside of our wavelength coverage have been reported along this sightline. This complicates detection of Ly α absorption features in our spectrum due to the possibility of non-Ly α lines associated with the higher cz Ly α absorbers occurring in our waveband. As reported in Bahcall et al. (1993), Savage, Sembach, & Lu (1995), and Tripp, Lu, & Savage (1998a,b), this sightline contains 9 known intergalactic Ly α absorbers with $\mathcal{W} > 200$ mÅ that are outside our redshift coverage. Also outside our coverage are 19 weaker intergalactic Ly α absorbers. Six of these have $100 \text{ mÅ} \leq \mathcal{W} < 200 \text{ mÅ}$ and 13 with $50 \text{ mÅ} \leq \mathcal{W} < 100 \text{ mÅ}$. In addition to these 28 Ly α systems, Savage, Sembach, & Lu (1995) report a Ly β absorber at $z=0.21656$. We doubt the reality of this identification owing to the absence of any Ly α absorption at this redshift (1478.9 Å) in Tripp, Lu, & Savage (1998a,b). We do detect the feature identified as Ly β in Savage, Sembach, & Lu (1995) at 1247.94 Å, but we identify it as Ly α at $z=0.0265$.

Bahcall et al. (1993) report a 680 mÅ intrinsic Ly α absorption at 1577 Å in their FOS data of H 1821+643. In our waveband, we expect to detect C III λ 977 and Ly γ associated with this absorber. Indeed, we detect these strong features at $z = 0.29673 \pm 0.00002$. Since both of these features are present, these detections allow us to shift the observations of Savage, Sembach, & Lu (1995) and Tripp, Lu, & Savage (1998a,b) to our LSR velocity scale. Based upon these LSR corrected wavelengths, in Table 4 we list all expected intervening absorptions lines from known intervening systems at higher redshift. Table 4 is ordered by strength of the rest-frame⁶ Ly α absorption ($\mathcal{W}_{Ly\alpha}$), and breaks naturally into detections and non-detections. Table 4 lists by column: (1) expected wavelength of the absorption based upon the redshift of the system and our LSR correction; (2) line identification; (3) system redshift; (4) rest-frame EW of Ly α in the system; (5) reference for the Ly α detection; (6) whether this feature was detected in our spectrum; and (7) comments, including the observed rest-frame EW.

In addition to the C III λ 977.0 and Ly γ absorptions at $z=0.297$, we detect 6 (possibly 7) of the 14 expected features, including 3 Ly β and 3 O VI λ 1031.92 lines. Of these 6 lines, the 1244.6 Å (Ly β), 1256.5 Å (Ly β), and 1264.1 Å (O VI λ 1031.92) detections were reported by Tripp, Lu, & Savage (1998a,b) or Savage, Sembach, & Lu (1995). The 1264 Å O VI λ 1031.92 absorption system at $z=0.225$ is studied in detail by Savage, Tripp, & Lu (1998), Barlow & Tytler (1998), and Tripp, Lu, & Savage (1998a,b). Our observations suggest that the $z=0.225$ system is actually composed of two components separated by ~ 75 km s⁻¹. This has recently been confirmed by Ly δ and Ly ϵ FUSE observations (Shull et al. 2000; Oegerle et al. 2000). We report the first detection of O VI λ 1031.92 (1252.2 Å) associated with the detected Ly β (1244.6 Å) at $z=0.213$. The unambiguous identification of O VI λ 1037.62 associated with this system is not possible due to HVC S II λ 1259.5 absorption. However, based upon the strength of the O VI λ 1031.92 detection (51 mÅ), we would expect a ~ 34 mÅ detection of O VI λ 1037.62. The S II λ 1259.5 HVC detection (80 ± 21 mÅ) is significantly stronger than our S II λ 1250.6 and S II λ 1253.8 HVC detections (30 ± 17 and 33 ± 13 mÅ) indicating that we are probably detecting O VI λ 1037.62 at $z=0.213$. In addition, we report the detection of Ly β (1257.7 Å) and O VI λ 1031.92 (1257.7 Å) associated with the $z=0.226$ Ly α detection of Tripp, Lu, & Savage (1998a). As summarized in Table 4, we detect all anticipated absorption features (Ly β , O VI λ 1032, 1038, or C III λ 977) whose associated Ly α absorption has $\mathcal{W} > 163$ mÅ.

It is important to note that, due to the uncertainties associated with the redshift determinations of the FOS Ly α detections and the limited resolution of the GHRS/G160M, the possibility of feature misidentifications in this sightline is greater than in the rest of our sample. As a followup study of this target with HST/STIS, we were awarded Cycle 8 observing time to measure the C IV λ 1548, 1550 absorption features associated with our O VI λ 1031.9 detections. We detect C IV for the strongest systems surveyed and will present these results elsewhere. At the extreme blue end of our spectrum, a feature which is possibly C III λ 977 associated with the $z=0.261$ system, is marginally detected (2σ). Due to the systematically higher noise level at the edges of the GHRS spectrum,

⁶Table 6 of Tripp, Lu, & Savage (1998a) incorrectly identifies rest-frame values as observed-frame.

this feature is not included by our $SL \geq 3\sigma$ criteria.

3.6. IZW1

The GHRS/G160M spectrum of IZW1 was first reported in Stocke et al. (1995). Except for Q1230+0115, this is the lowest S/N spectrum in our sample (~ 13), with an average 4σ detectable limit of $\mathcal{W}=100$ mÅ. We detect no intergalactic Ly α absorbers, although results previously presented (Stocke et al. 1995) showed 3 Ly α absorbers (two $> 4\sigma$, one $3\text{--}4\sigma$). However these spectra relied on the default 1995 IRAF/STSDAS/CALHRS calibration, which did not correctly handle photocathode blemishes and dead diodes. In both HST exposures, z1a60404n and z2ia0204n, approximately 1% of the spectrum was affected by a medium photocathode blemish, and 4% suffered from bad diodes. The previously reported 1222.21 Å absorption feature, now present at only $SL=1.6\sigma$, is close to the edge of our spectrum in a region of poor S/N. The previously reported 1236.5 Å feature is marginally present at $SL=1.8\sigma$. This is unfortunate, since two studies (Grogan & Geller 1998; Stocke et al. 1995) used these results for detailed analysis of the galaxy density distribution along this sightline. Our recalibrations show the previously reported Ly α features to be non-existent or below the 3σ level. The only features with $SL \geq 3\sigma$ in the GHRS/G160M spectra of IZW1 are the Galactic S II features. As previously reported in Stocke et al. (1995), and observed with IUE, the continuum hump at ~ 1245 Å is rest-frame C III $\lambda 1175$ emission at the redshift of IZW1. The LSR offset for this spectrum was 0.139 Å or 33.4 km s $^{-1}$ at 1253 Å.

3.7. Markarian 279

This spectrum is dominated by strong Ly α emission from Markarian 279 centered at 1252 Å ($z=0.0294$). The sightline passes through the HVC complex C, which we detect in S II $\lambda 1250$ at -160 km s $^{-1}$ (4.0σ) and in N V $\lambda 1238$ at -136 km s $^{-1}$ (4.4σ). Detection of this HVC is not possible in S II $\lambda 1253$ owing to strong intrinsic Ly α absorption at 1253.0–1253.7 Å. While Galactic N V $\lambda 1238$ is strong in this sightline (11σ , 51 mÅ), Galactic N V $\lambda 1242$ falls below our 3σ threshold for being included in our line list for this object. This alerts us to the possibility that the Galactic N V $\lambda 1238$ absorption may be superimposed on an intergalactic Ly α . Although we have only ~ 23 Å of coverage after applying our $cz_{\text{em}} - 1,200$ km s $^{-1}$ blueward limit, we detect six $SL \geq 4\sigma$ and two $3\sigma \leq SL < 4\sigma$ Ly α absorbers. The 1241.8 Å Ly α absorption feature could possibly be Si III $\lambda 1206.5$ intrinsic to Mrk 279 at $V_{\text{lsr}} \cong -40$ km s $^{-1}$. However, since we do not detect any intrinsic Ly α absorption at this velocity, this is likely to be an intergalactic Ly α absorption and we identify it as such. The LSR offset for this spectrum was 0.116 Å or 27.7 km s $^{-1}$ at 1253 Å.

Table 4: Anticipated Absorption Features in the H1821+643 Spectrum

Detections						
λ_{exp} (Å)	Identification	z	$\mathcal{W}_{\text{Ly}\alpha}$ (mÅ)	Ref	Detected	Comments
1256.53	Ly β	0.22489	739 ± 22	1	Yes	$\mathcal{W} = 509 \pm 28$ mÅ , two components
1264.13	OVI 1031.92	0.22489	739 ± 22	1	Yes	$\mathcal{W} = 190 \pm 18$ mÅ, $\Delta v \sim 75$ km s $^{-1}$
1261.25	Ly γ	0.29673	524 ± 8	1	Yes	$\mathcal{W} = 253 \pm 19$ mÅ
1267.07	CIII 977.03	0.29673	524 ± 8	1	Yes	$\mathcal{W} = 259 \pm 17$ mÅ
1244.60	Ly β	0.21326	483 ± 18	1	Yes	$\mathcal{W} = 153 \pm 18$ mÅ
1252.12	OVI 1031.92	0.21326	483 ± 18	1	Yes	$\mathcal{W} = 51 \pm 17$ mÅ, blended with Ly α at 1252.5 Å
1259.03	O VI λ 1037.62	0.21326	483 ± 18	1	Probable	$\mathcal{W} \sim 40$ mÅ, blended with HVC S II λ 1259.5
1257.75	Ly β	0.22621	280 ± 20	2	Yes	$\mathcal{W} = 20 \pm 14$ mÅ
1265.36	OVI 1031.92	0.22621	280 ± 20	2	Yes	$\mathcal{W} = 16 \pm 12$ mÅ
Non-Detections						
λ_{exp} (Å)	Identification	z	$\mathcal{W}_{\text{Ly}\alpha}$ (mÅ)	Ref	Detected	Comments
1237.63	CIII 977.03	0.26660	163 ± 13	1	No	
1247.04	Ly β	0.21577	146 ± 15	2	No	$< 2\sigma$
1254.58	OVI 1031.92	0.21577	146 ± 15	2	Possible	blended with Ly α
1242.93	Ly β	0.21176	104 ± 14	2	No	Blended with N V λ 1242
1250.45	OVI 1031.92	0.21176	104 ± 14	2	Indeterminate	If present, blended with Galactic S II λ 1250.6
1259.53	Ly β	0.22782	71 ± 11	1	Indeterminate	If present, blended with Galactic S II λ 1259.5
1236.32	OVI 1031.92	0.19794	58 ± 15	1	No	

Note. — All equivalent widths are rest-frame values. These spectral features are anticipated based upon the detection of Ly α absorption at a redshift that places strong non-Ly α lines (e.g., Ly β) in our waveband. The table is ordered by strength of the Ly α absorption and breaks naturally into detections and non-detections.

References. — 1: (GHRS+G160M) Savage, Sembach, & Lu (1995) or 2: (GHRS+G140L) Tripp, Lu, & Savage (1998a,b).

3.8. Markarian 290

The Markarian 290 spectrum was obtained by Wakker in 1997 for the purpose of studying the Galactic HVC complex C. This spectrum contains 3 definite and 3 possible ($3\sigma \leq SL < 4\sigma$) Ly α absorption features. Our spectrum covers a spectral range of 1232–1263 Å and is dominated by Ly α emission from Mrk 290 at ~ 1253 Å. Along this sightline we detect strong Galactic S II $\lambda\lambda 1250, 1253, 1259$, and Si II $\lambda 1260.4 + \text{Fe II } \lambda 1260.5$. As determined from Wakker & van Woerden (1991), the dominant H I-HVC velocity in this direction is -120 km s^{-1} . Wakker et al. (1996) report detections of high velocity gas (H I 21 cm) at $V_{\text{lsr}} \cong -138 \text{ km s}^{-1}$ and -115 km s^{-1} . We do not have the spectral resolution to resolve these two HVCs. We detect this combined HVC in Si II $\lambda 1260.4 + \text{Fe II } \lambda 1260.5$, S II $\lambda\lambda 1250, 1253, 1259$, and N V $\lambda\lambda 1238, 1242$. The S II and Si II+Fe II detections are all heavily blended with intrinsic Ly α absorption, and their EWs are not well determined. The LSR and HVC N V $\lambda\lambda 1238, 1242$ detections all fall below the 3σ level and are not included in the line list. The HVC detection of N V $\lambda 1242.8$ appears to be partially blended with Si III $\lambda 1206.5$ intrinsic to Mrk 290 (which is detected at $SL=3.7\sigma$). The LSR offset for this spectrum was 0.116 Å or 27.9 km s^{-1} at 1253 Å .

While several absorbers are reported in the wavelength range 1245–1248 Å, the rapidly rising continuum on the blue wing of the target’s Ly α emission calls their reality into question. Due to our concerns about the reality of these features, we have refit the continuum for Mrk 290 by altering the order of the global fit significantly. The statistical significances of these features remains robust despite these changes, so we list them as definite or possible Ly α features as shown in Figure 12.

3.9. Markarian 335

This sightline was previously reported in Stocke et al. (1995). It contains 4 definite Ly α absorption features along with strong Ly α emission from Markarian 335 and Galactic features. Due to calibration improvements, the wavelengths and feature significances have changed slightly from our previous results. Although not listed in Table 9, we also report possible weak detections of Galactic Mg II $\lambda\lambda 1239.9, 1240.4$ (2.5σ and 2.7σ). The Galactic Mg II $\lambda\lambda 1239.9, 1240.4$ absorption occurs at a wavelength at which Ly α would occur if it were associated with the galaxy identified as 00036+1928 in the CfA redshift survey and in Table 10. This galaxy is only $\sim 700h_{70}^{-1} \text{ kpc}$ from the sightline and appears as the small ‘v’ at $\sim 6,000 \text{ km s}^{-1}$ in the Mrk 335 “pie diagrams” of Figure 29. All Ly α absorption features are well-modeled by a single Gaussian component, except for the 1232.9 Å absorption feature, which at higher resolution may actually be two features separated by $\sim 45 \text{ km s}^{-1}$. But, at the resolution and S/N of our spectrum, it must be considered as a single absorber. Although this sightline passes through Galactic Radio Loop II, no high-velocity Galactic absorptions are detected. The LSR offset for this spectrum was 0.119 Å or 28.6 km s^{-1} at 1253 Å .

3.10. Markarian 421

This sightline was previously reported in Shull, Stocke, & Penton (1996). The Markarian 421 observation (z2ia0104t) suffered from HST target acquisition anomalies, which resulted in 11 of 42 spectral subexposures being removed from the coaddition. These anomalies were not detected by the default calibration used in our previous report, and as a result there are differences in our detections. Most noticeable is the reduced SL of the “mystery absorber” noted in Shull, Stocke, & Penton (1996) at 1257.1 Å, whose velocity was 1150 km s^{−1} higher than that reported for Mrk 421 itself, if it were Lyα. This feature, and its companion at 1256.9 Å, are now identified as intrinsic Lyα, but with SL < 4σ. Table 9 indicates our new results, which indicate one definite Lyα absorption feature at 1228.0 Å. This “void” absorber was first reported in Shull, Stocke, & Penton (1996).

Although this sightline does not pass through any known Galactic radio loops, it passes between H I-HVC components of the M complex (MI and MII) as discussed in Tufte et al. (1998). Lockman & Savage (1995) report an H I-HVC at $V_{\text{lsr}} = -58$ km s^{−1} with $N_{\text{HI}} = 5.9 \times 10^{19}$ cm^{−2} towards Mrk 421. We detect a HVC in both S II λ1250 ($V_{\text{lsr}} = -52$ km s^{−1}) and S II λ1253 ($V_{\text{lsr}} = -53$ km s^{−1}). The rest EWs for these S II-HVC detections are 28 mÅ and 33 mÅ, respectively. If $b=25$ km s^{−1}, then $N_{\text{SII}} \sim 3.4 \times 10^{14}$ cm^{−2} and $N_{\text{SII}}/N_{\text{HI}} = 6 \times 10^{-6}$, or ~30% of the solar abundance of S/H. Although it is possible that the S II HVC detections could be intrinsic Lyα absorbers, we consider this unlikely due to the presence of absorptions in both components of the S II lines detectable in the observed band.

Also of note is the possibility that the 3σ N V λ1238 detection has a velocity that is more consistent with the detected HVC component. There is an unreported 1.9σ detection at the expected LSR position of N V λ1242. The LSR offset for this spectrum was 0.160 Å or 38.2 km s^{−1} at 1253 Å.

3.11. Markarian 501

The Markarian 501 sightline was previously reported in Stocke et al. (1995, S95) and passes through the Galactic HVC complex C. Along this sightline, the dominant H I-HVC velocity is at $V_{\text{lsr}} \cong -115$ km s^{−1} (Wakker & van Woerden 1991). However, this is one of our lower S/N spectra and we do not detect any HVC absorption. We do detect strong Galactic S II λλ1250, 1253 absorption. Due to improvements in calibration, as previously described, our results have changed slightly since S95. Similar to S95, we report 4 definite Lyα absorptions and no possible ($3\sigma \leq SL < 4\sigma$) detections. Absorber “A” of S95 is essentially unchanged, but absorbers “B” and “C” of S95 have changed somewhat. Previously, the “B” absorber (1239.97 Å) was quoted as having a significance of 3.4σ, while the “C” absorber (1246.18 Å) was quoted as 4.6σ. Our new results place the S95 “B” absorber’s significance at 4.2σ and the “C” absorber’s at 4.0σ. Therefore, we now believe the “B” (1239.97 Å) feature to be definite, however it may be partially contaminated by

Galactic Mg II $\lambda 1239.9$ absorption. No Galactic Mg II $\lambda 1240.4$ absorption is detected at the $80 \text{ m}\text{\AA}$ (4σ) level. Hence, we cannot estimate the amount of Mg II $\lambda 1239.9$ contamination of the 1239.97 \AA feature, if any. We note that, while absorber “C” was identified in S95 as the best example of a Ly α cloud in a void, absorber “B” is located much farther into the void in this region. Therefore, the important conclusions of S95 are unaffected. Calibration improvements have also allowed us to resolve the previously unreported 1251.15 \AA Ly α feature from Galactic S II $\lambda 1250.6$ absorption. We have identified this absorption as Ly α because there is no H I emission seen at positive velocities in this direction. However, Mrk 501 lies behind complex C which has blueshifted H I only (Wakker & van Woerden 1991) which may account for the blueshifted component of S II $\lambda 1253.8$. The LSR offset for this spectrum was 0.232 \AA or 55.4 km s^{-1} at 1253 \AA .

3.12. Markarian 509

The Markarian 509 ($1231.7 \text{ \AA} - 1268.8 \text{ \AA}$) sightline has been previously reported in Savage, Sembach, & Lu (1997) and Sembach et al. (1995, 1999, who focused on the Galactic HVCs). These reports were based solely upon the pre-COSTAR HST/G160M observation z1790208m. We detect one definite intergalactic Ly α along this sightline. Our analysis combines this observation with a post-COSTAR observation at a slightly lower wavelength range ($1219.5 \text{ \AA} - 1255.6 \text{ \AA}$, see Table 1). The flux level of our HST exposure, z3e70704t, was scaled to be consistent with the initial Mrk 509 exposure. The scaling was applied linearly across the overlap region between exposures. The large gradient in the \mathcal{W} detection limit shortward of 1233 \AA is because this portion of the spectrum was observed only with the post-COSTAR exposure. Along this sightline, Sembach et al. (1995, 1999) report C IV-HVCs at -228 km s^{-1} and -283 km s^{-1} , while Anglo-Australian telescope (York 1982) observations of Na I D lines and Ca II H and K lines indicate Galactic velocity components near $V_{\text{lsr}} \approx +5 \text{ km s}^{-1}$ and $+60 \text{ km s}^{-1}$. With our GHRS/G160M data we detect HVC gas in S II $\lambda\lambda 1250, 1253$, N V $\lambda 1238$, Mg II $\lambda 1239$, and possibly in N V $\lambda 1242$ and Mg II $\lambda 1240$. The N V and Mg II Galactic lines show velocity structure over the V_{lsr} range of -65 to $+60 \text{ km s}^{-1}$. We do not have the spectral resolution to confirm the $+5 \text{ km s}^{-1}$ component. We do not detect S II $\lambda\lambda 1250, 1253$ absorption at $V_{\text{lsr}} = -228$ or -283 km s^{-1} . Intrinsic Ly α associated with Mrk 509 prevents us from detecting HVC absorption due to S II $\lambda 1259$ at these velocities ($V_{\text{lsr}} = -228$ and -283 km s^{-1}). Similarly, HVC detection of Si II $\lambda 1260.4 + \text{Fe II } \lambda 1260.5$ at these velocities is not possible due to Galactic S II $\lambda 1259$, and Mg II $\lambda\lambda 1239.9, 1240.4$ detections are complicated by the presence of Galactic and HVC N V $\lambda\lambda 1238, 1242$. We also detect Galactic absorption in N V $\lambda\lambda 1238, 1242$, Mg II $\lambda 1239.9$, S II $\lambda\lambda 1250, 1253, 1259$, and Si II $\lambda 1260.4 + \text{Fe II } \lambda 1260.5$, and possibly C I $\lambda 1260$ (heavily blended with Si II $\lambda 1260.4 + \text{Fe II } \lambda 1260.5$, and Si II $\lambda 1260.4 + \text{Fe II } \lambda 1260.5$ HVC, and a possible intrinsic Ly α absorption in Mrk 509). We detect high-velocity Galactic gas at $+60$ and -65 km s^{-1} in N V $\lambda 1238$, S II $\lambda\lambda 1250, 1253, 1259$ and possibly Si II $\lambda 1260.4 + \text{Fe II } \lambda 1260.5$. The Si II $\lambda 1260.4 + \text{Fe II } \lambda 1260.5$ absorption is apparently heavily blended with H I absorption intrinsic to Mrk 509, and possible Galactic C I $\lambda 1260$. Along with these HVCs, the spectrum of Mrk 509 contains a single definite ($SL \geq 4\sigma$) Ly α absorption feature at 2560 km s^{-1} . The LSR offset for

this spectrum was 0.060 \AA or 14.4 km s^{-1} at 1253 \AA .

Numerous strong intrinsic $\text{Ly}\alpha$ absorption lines are observed in our Mrk 509 spectrum. This absorption shows significant structure over the velocity range of -450 to $+200 \text{ km s}^{-1}$. Our modelling suggests 7-9 separate velocity components. Recent FUSE observations (Kriss et al. 2000) detect these absorbers in $\text{Ly}\beta$, C III $\lambda 977.0$, and O VI $\lambda 1031.9$, which they model with 7 separate components. Efforts are underway to match our $\text{Ly}\alpha$ detections with the FUSE detections to determine the metallicity and b -values of these intrinsic absorbers. These results will be reported elsewhere (Shull et al. 2000).

3.13. Markarian 817

The sightline towards Markarian 817 passes through HVC complex C. The dominant H I-HVC velocity in this direction is -115 km s^{-1} (Wakker & van Woerden 1991). We detect strong Galactic S II $\lambda\lambda 1250, 1253$, two HVCs ($V_{\text{lsr}} \approx -45 \text{ km s}^{-1}$ and -110 km s^{-1}) in S II $\lambda\lambda 1250, 1253$ as well as N V $\lambda\lambda 1238, 1242$ (Galactic+HVCs). The N V $\lambda 1238.8$ and N V $\lambda 1242.8$ regions are both confused with significant structure. The N V $\lambda 1238.8$ result is the combination of LSR+HVC absorptions, while the 1242.5 \AA detection appears to be associated with the HVC at $V_{\text{lsr}} = -45 \text{ km s}^{-1}$. The $V_{\text{lsr}} = -110 \text{ km s}^{-1}$ HVC is also detected in N V $\lambda 1242.8$ at the 2.8σ level. Galactic N V $\lambda 1242.8$ at LSR is also detected, but at the anomalously low 3.1σ level. We do not detect any Galactic Mg II $\lambda\lambda 1239.9, 1240.4$ absorption, although it is possible that the reported 1239.5 \AA feature is contaminated with weak Mg II $\lambda 1239.9$ HVC absorption. Note that, along this sightline the HVC N V and Mg II absorptions are stronger than the LSR Galactic components. In addition to the Galactic detections, this rich sightline contains 9 definite $\text{Ly}\alpha$ absorption features and several $\text{Ly}\alpha$ absorptions identified as intrinsic to Mrk 817. The LSR offset for this spectrum was 0.083 \AA or 19.8 km s^{-1} at 1253 \AA .

3.14. PKS 2155-304

The pre-COSTAR spectrum of PKS 2155-304 contains 8 definite ($SL \geq 4\sigma$) and 4 possible ($3\sigma \leq SL < 4\sigma$) $\text{Ly}\alpha$ absorption features, as well as Galactic Mg II $\lambda\lambda 1239.9, 1240.4$ and S II $\lambda\lambda 1250, 1253$ absorption. An analysis of this sightline has been previously reported in Shull et al. (1998). Improvements in the calibration process since the publication of that paper produce slightly different results. Most notable is the inclusion of the 1235.8 \AA $\text{Ly}\alpha$ feature, which is blended with the 1236.0 \AA and 1236.4 \AA features. Our restriction of $b < 100 \text{ km s}^{-1}$, which was not present in our previous reduction, forced us to add a third component to this blend. As a result, EWs for the 1235.6 \AA and 1236.4 \AA features are slightly different than previously reported. The 1238.7 \AA feature is partially blended with Galactic N V $\lambda 1238$. In our previous paper (Shull et al. 1998) we estimated the N V contribution, while for this paper we have fitted blended components to both

N V $\lambda 1238$ and Ly α . The feature marked as possible Ly α at 1256.7 Å could also be a Galactic S II $\lambda 1253$ HVC. Galactic N V $\lambda\lambda 1238, 1242$, Mg II $\lambda\lambda 1239.9, 1240.4$, and S II $\lambda\lambda 1250, 1253$ are all present and strong. The LSR offset for the pre-COSTAR spectrum was 0.013 Å or 3.0 km s^{−1} at 1253 Å.

The post-COSTAR spectrum of PKS 2155-304 was also reported in Shull et al. (1998) and contains 8 definite and 1 possible Ly α absorption features. As with the pre-COSTAR spectrum, minor improvements to the calibration process produce slightly improved feature modelings. A detailed discussion of the clump of 8 Ly α absorbers near $cz = 17,000$ km s^{−1} is given in Shull et al. (1998). The third (most blueward) component of the 1284–1285 Å Ly α complex is only marginally required by our fitting routines. Relaxing our b -value ≤ 100 km s^{−1} criteria provides an adequate 2 component spectral fit as originally reported in Shull et al. (1998). Galactic S II $\lambda 1259$ is present along with strong Si II $\lambda 1260.4$ + Fe II $\lambda 1260.5$, and a Si II $\lambda 1260.4$ + Fe II $\lambda 1260.5$ HVC detection (Sembach et al. 1999). The post-COSTAR PKS 2155-304 spectrum was corrected to the LSR using the Galactic H I and only the S II line (1259 Å). The LSR offset for the post-COSTAR spectrum was 0.073 Å or 17.4 km s^{−1} at 1253 Å. The PKS 2155-304 sightline does not pass through any known H I-HVCs or Galactic radio loops, although C IV-HVCs were detected by Sembach et al. (1995) at $V_{\text{lsr}} = -260$ and -145 km s^{−1}. We detect the $V_{\text{lsr}} = -145$ km s^{−1} component in Si II $\lambda 1260.4$ + Fe II $\lambda 1260.5$ (at $V_{\text{lsr}} = -154$ km s^{−1}) and report a possible (2.4σ) detection of the $V_{\text{lsr}} = -260$ km s^{−1} component in S II $\lambda 1253$.

3.15. Q1230+0115

The spectrum of the QSO Q1230+0115 contains 6 definite and 4 possible ($3\sigma \leq SL < 4\sigma$) Ly α absorption features. This sightline does not pass through any known radio loops or HVCs and is only 0.91° degrees from the 3C 273 sightline. This sightline shows a cluster of four Ly α absorbers within 1 Å (~ 200 km s^{−1}) of 1222.5 Å (1,700 km s^{−1}) and an additional Ly α absorber at 1225 Å (2,303 km s^{−1}). A possible (3.1σ) Ly α absorber is also present at 1223.9 Å (2037 km s^{−1}). Another possible absorber (2.0σ) at 1221.05 Å is not statistically significant due a minor diode problem close to its location (see the EW detection limit panel in Figure 20). The 3C 273 sightline also contains an absorber at 1,586 km s^{−1} and 2 possible absorbers at 2,200–2,300 km s^{−1} which appear to closely match detections in this sightline. The transverse separations between these sightlines at 1,500 km s^{−1} and 2,300 km s^{−1} are 340 and 520 h_{70}^{-1} kpc, respectively. This sightline pair is investigated further in Paper III. Galactic N V $\lambda 1238$ is detected at the 2.7σ level, while N V $\lambda 1242$ is marginally detected at the 1.7σ level. The N V $\lambda 1242$ absorption is partially blended with the possible absorber at 1242.9 Å. The Mg II $\lambda\lambda 1239.9, 1240.4$ lines are not detected in this sightline. This spectrum has the lowest S/N (~ 9) of our sample and is being reobserved in cycle 7 with HST/STIS. The LSR offset for this spectrum was -0.003 Å or -0.7 km s^{−1} at 1253 Å.

4. Master Lists of Detected Absorption Features

We consider absorption features with significance levels $SL \geq 4\sigma$ to be definite, while absorption lines with $3\sigma \leq SL < 4\sigma$ are classified as possible. Table 5 presents all definite and Table 6 all possible intergalactic Ly α absorptions. Table 7 presents a summary of all definite Galactic HVC clouds. Due to the overlap between the regions of the sky covered by the HVC complex C and the initial CfA slices, we detect Galactic HVCs in 8 of our 15 sightlines. This fraction is considerably larger than the value of 37% found for HVCs seen in 21 cm emission toward AGN sightlines down to $N_{\text{HI}} = 7 \times 10^{17} \text{ cm}^{-2}$. (Murphy, Lockman, & Savage 1995). Hence, we expect that the HVC detection rate will decrease with future observations due to this unintentional overlap. Table 8 shows a list of all definite lines determined to be intrinsic to the observed target.

The first column of each of the master tables indicates the name of the target in which the feature was detected. An asterisk before the target name denotes a detection in pre-COSTAR data. The second column indicates the LSR-adjusted wavelength and wavelength uncertainty for each feature. The third column lists the recession velocity (for Ly α features, Tables 5 and 6), velocity relative to LSR (HVC features, Table 7), or velocity relative to the narrow emission line rest frame of the target (intrinsic features, Table 8). All velocities are quoted as cz , in units of km s^{-1} . Velocity uncertainties based upon the total wavelength uncertainties (see § 2.3.3) are also provided. The fourth column provides the single-component rest-frame Doppler width (b in km s^{-1}) and its 1σ uncertainty for each feature as estimated from the Gaussian width ($\mathbf{W}_G = b_{\text{obs}}/\sqrt{2}$) of the fitted feature, restricted to the range of $12 < b_{\text{obs}} < 100 \text{ km s}^{-1}$. The Doppler widths have been corrected for the spectral resolution of the GHRS (FWHM $\sim 19 \text{ km s}^{-1}$) and our pre-fit smoothing (see § 2.3.1 and eq. 2). As discussed in Paper II, the measured b -values in pre-COSTAR data are occasionally artificially large. The fifth column lists the rest-frame EW (\mathcal{W} in $\text{m}\text{\AA}$) and 1σ uncertainty of each absorption feature. The sixth column indicates the significance level (SL in σ) of each feature. In Tables 7, the seventh column indicates the atomic identification of the detected absorption. In Table 8, the final column gives the redshift of the intrinsic system.

Table 5. Definite ($SL \geq 4\sigma$) Intergalactic Ly α Features

Target	Wavelength (Å)	Velocity (km s ⁻¹)	b (km s ⁻¹)	\mathcal{W} (mÅ)	SL (σ)
*3C273	1219.786 \pm 0.024	1015 \pm 6	69 \pm 5	369 \pm 36	34.8
*3C273	1222.100 \pm 0.023	1586 \pm 6	72 \pm 4	373 \pm 30	42.0
*3C273	1224.954 \pm 0.029	2290 \pm 7	54 \pm 33	35 \pm 30	4.2
*3C273	1247.593 \pm 0.046	7872 \pm 11	34 \pm 17	33 \pm 18	5.8
*3C273	1251.485 \pm 0.032	8832 \pm 8	61 \pm 10	114 \pm 25	14.8
*3C273	1255.542 \pm 0.069	9833 \pm 17	64 \pm 24	46 \pm 22	5.9
*3C273	1275.243 \pm 0.031	14691 \pm 7	61 \pm 8	140 \pm 25	16.3
*3C273	1276.442 \pm 0.059	14987 \pm 14	52 \pm 20	46 \pm 22	5.4
*3C273	1277.474 \pm 0.136	15241 \pm 33	88 \pm 52	52 \pm 40	6.3
*3C273	1280.267 \pm 0.077	15930 \pm 19	71 \pm 28	64 \pm 33	6.4
*3C273	1289.767 \pm 0.098	18273 \pm 24	82 \pm 36	47 \pm 28	6.1
*3C273	1292.851 \pm 0.051	19033 \pm 12	45 \pm 17	47 \pm 22	5.5
*3C273	1296.591 \pm 0.025	19956 \pm 6	62 \pm 4	297 \pm 25	33.0
AKN120	1232.052 \pm 0.034	4040 \pm 8	32 \pm 11	48 \pm 18	5.5
AKN120	1242.972 \pm 0.028	6733 \pm 7	33 \pm 8	53 \pm 13	9.2
AKN120	1247.570 \pm 0.087	7867 \pm 21	34 \pm 35	20 \pm 25	4.3
AKN120	1247.948 \pm 0.023	7960 \pm 5	27 \pm 4	147 \pm 22	31.4
AKN120	1248.192 \pm 0.027	8020 \pm 7	23 \pm 6	65 \pm 17	14.1
FAIRALL9	1240.988 \pm 0.038	6244 \pm 9	35 \pm 13	22 \pm 9	5.3
FAIRALL9	1244.462 \pm 0.034	7100 \pm 8	39 \pm 11	32 \pm 10	8.2
FAIRALL9	1254.139 \pm 0.024	9487 \pm 6	43 \pm 6	84 \pm 13	26.5
FAIRALL9	1262.864 \pm 0.029	11638 \pm 7	28 \pm 13	16 \pm 8	5.2
FAIRALL9	1263.998 \pm 0.041	11918 \pm 10	42 \pm 15	22 \pm 9	7.0
FAIRALL9	1264.684 \pm 0.073	12087 \pm 18	44 \pm 33	30 \pm 28	10.2
FAIRALL9	1265.104 \pm 0.026	12191 \pm 6	23 \pm 7	28 \pm 7	9.5
FAIRALL9	1265.970 \pm 0.117	12404 \pm 29	32 \pm 23	19 \pm 23	7.0
H1821+643	1245.440 \pm 0.023	7342 \pm 5	47 \pm 3	298 \pm 20	42.4
H1821+643	1246.301 \pm 0.036	7554 \pm 9	41 \pm 14	50 \pm 24	7.1
H1821+643	1247.583 \pm 0.029	7870 \pm 7	19 \pm 9	40 \pm 17	5.4
H1821+643	1247.937 \pm 0.033	7957 \pm 8	33 \pm 10	68 \pm 38	9.4
H1821+643	1265.683 \pm 0.025	12334 \pm 6	28 \pm 6	64 \pm 15	11.8
MARK279	1236.942 \pm 0.030	5246 \pm 7	27 \pm 9	30 \pm 10	5.6

Table 5—Continued

Target	Wavelength (Å)	Velocity (km s ⁻¹)	b (km s ⁻¹)	\mathcal{W} (mÅ)	SL (σ)
MARK279	1241.509 \pm 0.029	6372 \pm 7	18 \pm 4	58 \pm 7	14.2
MARK279	1241.805 \pm 0.023	6445 \pm 6	21 \pm 4	40 \pm 7	10.4
MARK279	1243.753 \pm 0.023	6925 \pm 5	26 \pm 3	65 \pm 8	16.8
MARK279	1247.216 \pm 0.024	7779 \pm 6	28 \pm 5	48 \pm 9	15.1
MARK279	1247.533 \pm 0.042	7858 \pm 10	34 \pm 14	21 \pm 10	6.7
MARK290	1234.597 \pm 0.027	4667 \pm 7	26 \pm 8	60 \pm 18	7.2
MARK290	1244.408 \pm 0.032	7087 \pm 8	23 \pm 11	23 \pm 10	4.3
MARK290	1245.536 \pm 0.025	7365 \pm 6	11 \pm 9	21 \pm 7	4.2
*MARK335	1223.637 \pm 0.026	1965 \pm 6	75 \pm 7	229 \pm 30	28.1
*MARK335	1224.974 \pm 0.049	2295 \pm 12	73 \pm 17	81 \pm 26	10.2
*MARK335	1232.979 \pm 0.057	4268 \pm 14	51 \pm 20	33 \pm 16	5.1
*MARK335	1241.093 \pm 0.026	6269 \pm 6	75 \pm 6	130 \pm 14	30.3
MARK421	1227.977 \pm 0.025	3035 \pm 6	35 \pm 5	86 \pm 15	12.4
*MARK501	1234.572 \pm 0.039	4661 \pm 10	60 \pm 13	161 \pm 43	11.1
*MARK501	1239.968 \pm 0.029	5992 \pm 7	59 \pm 39	55 \pm 46	4.2
*MARK501	1246.177 \pm 0.069	7523 \pm 17	48 \pm 26	53 \pm 36	4.0
*MARK501	1251.152 \pm 0.029	8750 \pm 7	77 \pm 49	66 \pm 57	4.9
MARK509	1226.050 \pm 0.025	2560 \pm 6	40 \pm 5	209 \pm 32	14.4
MARK817	1223.507 \pm 0.037	1933 \pm 9	34 \pm 13	29 \pm 13	5.3
MARK817	1224.172 \pm 0.023	2097 \pm 5	40 \pm 4	135 \pm 15	25.3
MARK817	1234.657 \pm 0.041	4682 \pm 10	40 \pm 15	23 \pm 11	5.6
MARK817	1236.303 \pm 0.023	5088 \pm 6	84 \pm 4	207 \pm 14	56.3
MARK817	1236.902 \pm 0.027	5236 \pm 7	24 \pm 7	25 \pm 7	6.6
MARK817	1239.159 \pm 0.029	5793 \pm 7	39 \pm 12	34 \pm 13	8.7
MARK817	1241.034 \pm 0.024	6255 \pm 6	29 \pm 5	37 \pm 8	11.6
MARK817	1245.395 \pm 0.051	7330 \pm 13	51 \pm 18	17 \pm 7	5.9
MARK817	1247.294 \pm 0.044	7799 \pm 11	56 \pm 16	28 \pm 9	10.1
*PKS2155-304	1226.345 \pm 0.060	2632 \pm 15	61 \pm 33	42 \pm 40	9.2
*PKS2155-304	1226.964 \pm 0.065	2785 \pm 16	64 \pm 26	36 \pm 22	7.9
*PKS2155-304	1232.016 \pm 0.049	4031 \pm 12	39 \pm 17	21 \pm 11	4.2
*PKS2155-304	1235.748 \pm 0.029	4951 \pm 7	68 \pm 15	64 \pm 23	14.3
*PKS2155-304	1235.998 \pm 0.029	5013 \pm 7	58 \pm 11	82 \pm 22	18.1

Table 5—Continued

Target	Wavelength (Å)	Velocity (km s ⁻¹)	b (km s ⁻¹)	\mathcal{W} (mÅ)	SL (σ)
*PKS2155-304	1236.426 \pm 0.029	5119 \pm 7	80 \pm 5	218 \pm 20	48.1
*PKS2155-304	1238.451 \pm 0.029	5618 \pm 7	33 \pm 14	29 \pm 15	6.7
*PKS2155-304	1238.673 \pm 0.031	5673 \pm 8	30 \pm 12	39 \pm 16	9.1
PKS2155-304	1270.784 \pm 0.027	13591 \pm 6	39 \pm 6	101 \pm 18	12.5
PKS2155-304	1281.375 \pm 0.024	16203 \pm 5	58 \pm 3	346 \pm 23	44.8
PKS2155-304	1281.867 \pm 0.061	16325 \pm 15	49 \pm 22	62 \pm 34	8.2
PKS2155-304	1284.301 \pm 0.030	16925 \pm 7	19 \pm 13	43 \pm 37	5.7
PKS2155-304	1284.497 \pm 0.039	16973 \pm 9	63 \pm 6	389 \pm 68	50.9
PKS2155-304	1285.086 \pm 0.038	17119 \pm 9	87 \pm 11	448 \pm 79	57.9
PKS2155-304	1287.497 \pm 0.024	17713 \pm 6	35 \pm 5	139 \pm 21	18.4
PKS2155-304	1288.958 \pm 0.029	18073 \pm 7	47 \pm 8	99 \pm 20	13.2
Q1230+0115	1221.711 \pm 0.026	1490 \pm 6	21 \pm 8	138 \pm 42	6.3
Q1230+0115	1222.425 \pm 0.035	1666 \pm 9	54 \pm 10	385 \pm 94	16.9
Q1230+0115	1222.747 \pm 0.029	1745 \pm 7	40 \pm 12	241 \pm 99	10.9
Q1230+0115	1223.211 \pm 0.051	1860 \pm 13	48 \pm 21	142 \pm 81	6.6
Q1230+0115	1225.000 \pm 0.024	2301 \pm 6	55 \pm 6	439 \pm 57	23.9
Q1230+0115	1253.145 \pm 0.031	9242 \pm 8	72 \pm 8	301 \pm 49	24.8

Table 6. Possible ($3\sigma \leq SL < 4\sigma$) Intergalactic Ly α features

Target	Wavelength (Å)	Velocity (km s ⁻¹)	b (km s ⁻¹)	\mathcal{W} (mÅ)	SL (σ)
*3C273	1224.587 \pm 0.150	2199 \pm 37	57 \pm 55	29 \pm 35	3.5
*3C273	1234.704 \pm 0.029	4694 \pm 7	69 \pm 61	25 \pm 29	3.5
*3C273	1265.701 \pm 0.064	12338 \pm 16	33 \pm 26	21 \pm 18	3.3
*3C273	1266.724 \pm 0.084	12590 \pm 21	52 \pm 30	24 \pm 18	3.6
*3C273	1268.969 \pm 0.076	13144 \pm 19	43 \pm 28	18 \pm 15	3.1
AKN120	1223.088 \pm 0.039	1829 \pm 10	25 \pm 17	64 \pm 48	3.7
AKN120	1247.267 \pm 0.104	7792 \pm 26	34 \pm 32	19 \pm 22	3.9
ESO141-G55	1249.932 \pm 0.036	8449 \pm 9	17 \pm 15	12 \pm 8	3.0
ESO141-G55	1252.483 \pm 0.041	9078 \pm 10	23 \pm 16	12 \pm 7	3.1
FAIRALL9	1265.407 \pm 0.029	12265 \pm 7	19 \pm 18	11 \pm 8	3.8
H1821+643	1238.014 \pm 0.036	5510 \pm 9	21 \pm 14	23 \pm 13	3.3
H1821+643	1240.569 \pm 0.036	6140 \pm 9	14 \pm 16	24 \pm 16	3.4
H1821+643	1244.966 \pm 0.031	7225 \pm 8	15 \pm 12	25 \pm 13	3.5
H1821+643	1247.362 \pm 0.029	7815 \pm 7	36 \pm 34	27 \pm 29	3.7
H1821+643	1252.477 \pm 0.042	9077 \pm 10	21 \pm 15	23 \pm 15	3.6
H1821+643	1254.874 \pm 0.099	9668 \pm 24	24 \pm 31	21 \pm 25	3.6
MARK279	1237.915 \pm 0.029	5486 \pm 7	30 \pm 29	17 \pm 18	3.5
MARK279	1238.502 \pm 0.047	5631 \pm 12	21 \pm 23	18 \pm 18	3.7
MARK290	1232.797 \pm 0.064	4224 \pm 16	21 \pm 29	41 \pm 49	3.6
MARK290	1235.764 \pm 0.044	4955 \pm 11	26 \pm 18	28 \pm 19	3.4
MARK290	1245.869 \pm 0.026	7447 \pm 6	8 \pm 12	18 \pm 7	3.6
*PKS2155-304	1234.767 \pm 0.051	4709 \pm 12	32 \pm 24	15 \pm 14	3.3
*PKS2155-304	1246.990 \pm 0.029	7724 \pm 7	31 \pm 35	13 \pm 16	3.0
*PKS2155-304	1247.510 \pm 0.029	7852 \pm 7	30 \pm 31	13 \pm 16	3.1
*PKS2155-304	1255.084 \pm 0.041	9720 \pm 10	24 \pm 16	13 \pm 9	3.0
*PKS2155-304	1256.636 \pm 0.042	10102 \pm 10	25 \pm 15	14 \pm 8	3.3
PKS2155-304	1264.806 \pm 0.058	12117 \pm 14	39 \pm 20	31 \pm 19	3.6
Q1230+0115	1236.045 \pm 0.041	5025 \pm 10	24 \pm 15	53 \pm 31	3.1
Q1230+0115	1242.897 \pm 0.044	6714 \pm 11	19 \pm 19	45 \pm 35	3.2
Q1230+0115	1246.254 \pm 0.049	7542 \pm 12	31 \pm 18	44 \pm 27	3.3

Table 7. Galactic HVC features with $SL \geq 4\sigma$.

Target	Wavelength (Å)	Velocity (km s ⁻¹)	b (km s ⁻¹)	\mathcal{W} (mÅ)	SL (σ)	ID
ESO141-G55	1253.444 \pm 0.038	-85 \pm 9	27 \pm 13	18 \pm 9	4.7	SiII1253.8
ESO141-G55	1259.304 \pm 0.029	-47 \pm 7	48 \pm 23	23 \pm 14	5.8	SiII1259.5
ESO141-G55	1260.204 \pm 0.029	-70 \pm 7	44 \pm 6	83 \pm 73	21.1	SiII+FeII1260.5
FAIRALL9	1251.367 \pm 0.025	188 \pm 6	32 \pm 5	41 \pm 7	11.3	SiII1250.6
FAIRALL9	1254.572 \pm 0.023	182 \pm 5	27 \pm 4	56 \pm 7	17.6	SiII1253.8
FAIRALL9	1260.338 \pm 0.029	199 \pm 7	15 \pm 5	34 \pm 9	8.9	SiII1259.5
FAIRALL9	1261.039 \pm 0.035	128 \pm 8	54 \pm 6	379 \pm 75	105.2	SiII+FeII1260.5
FAIRALL9	1261.300 \pm 0.028	190 \pm 7	36 \pm 4	180 \pm 62	51.3	SiII+FeII1260.5
H1821+643	1238.608 \pm 0.029	-47 \pm 7	38 \pm 22	42 \pm 27	5.9	NV1238.8
H1821+643	1242.616 \pm 0.029	-44 \pm 7	42 \pm 20	56 \pm 30	8.2	NV1242.8
H1821+643	1250.314 \pm 0.029	-65 \pm 7	26 \pm 13	30 \pm 17	4.4	SiII1250.6
H1821+643	1253.314 \pm 0.029	-119 \pm 7	17 \pm 10	31 \pm 13	5.0	SiII1253.8
H1821+643	1259.157 \pm 0.029	-86 \pm 7	59 \pm 10	99 \pm 24	16.2	SiII1259.5
H1821+643	1260.052 \pm 0.029	-107 \pm 7	59 \pm 4	440 \pm 35	74.4	SiII+FeII1260.5
MARK279	1238.260 \pm 0.037	-136 \pm 9	20 \pm 18	22 \pm 16	4.3	NV1238.8
MARK279	1249.933 \pm 0.034	-160 \pm 8	23 \pm 14	12 \pm 8	4.0	SiII1250.6
MARK290	1250.019 \pm 0.029	-139 \pm 7	31 \pm 22	19 \pm 23	5.6	SiII1250.6
MARK290	1253.327 \pm 0.029	-113 \pm 7	28 \pm 5	34 \pm 6	13.7	SiII1253.8
MARK290	1259.058 \pm 0.029	-110 \pm 7	39 \pm 7	72 \pm 16	15.2	SiII1259.5
MARK290	1260.008 \pm 0.029	-117 \pm 7	63 \pm 3	479 \pm 28	97.3	SiII+FeII1260.5
MARK421	1250.385 \pm 0.031	-52 \pm 7	11 \pm 16	28 \pm 31	4.5	SiII1250.6
MARK421	1253.578 \pm 0.031	-53 \pm 8	11 \pm 13	33 \pm 29	4.8	SiII1253.8
*MARK501	1253.069 \pm 0.264	-175 \pm 63	99 \pm 3	64 \pm 33	4.7	SiII1253.8
MARK509	1239.182 \pm 0.029	-180 \pm 7	21 \pm 18	24 \pm 29	5.1	MgII1239.9
MARK509	1243.060 \pm 0.734	62 \pm 177	35 \pm 38	17 \pm 21	4.3	NV1242.8
MARK509	1250.314 \pm 0.029	-69 \pm 7	24 \pm 9	20 \pm 7	7.2	SiII1250.6
MARK509	1250.819 \pm 0.029	56 \pm 7	42 \pm 5	58 \pm 8	21.3	SiII1250.6
MARK509	1253.561 \pm 0.029	-57 \pm 7	41 \pm 9	27 \pm 7	11.7	SiII1253.8
MARK509	1254.079 \pm 0.032	64 \pm 8	40 \pm 6	85 \pm 19	37.5	SiII1253.8
*MARK509	1258.365 \pm 0.029	-270 \pm 7	53 \pm 13	237 \pm 151	122.7	SiII1259.5
*MARK509	1258.565 \pm 0.029	-222 \pm 7	33 \pm 8	43 \pm 46	22.6	SiII1259.5
*MARK509	1259.858 \pm 0.029	85 \pm 7	34 \pm 19	30 \pm 37	16.1	SiII1259.5

Table 7—Continued

Target	Wavelength (Å)	Velocity (km s ⁻¹)	b (km s ⁻¹)	\mathcal{W} (mÅ)	SL (σ)	ID
*MARK509	1260.257 \pm 0.029	-48 \pm 7	68 \pm 64	43 \pm 52	22.2	SiII+FeII1260.5
*MARK509	1260.710 \pm 0.029	50 \pm 7	72 \pm 4	372 \pm 73	186.9	SiII+FeII1260.5
MARK817	1238.529 \pm 0.029	-65 \pm 7	75 \pm 28	54 \pm 41	13.5	NV1238.8
MARK817	1239.509 \pm 0.029	-101 \pm 7	46 \pm 18	25 \pm 12	6.3	MgII1239.9
MARK817	1250.071 \pm 0.034	-127 \pm 8	24 \pm 13	13 \pm 6	5.1	SII1250.6
MARK817	1250.415 \pm 0.029	-44 \pm 7	30 \pm 11	26 \pm 9	9.8	SII1250.6
MARK817	1253.355 \pm 0.027	-106 \pm 6	27 \pm 12	32 \pm 13	12.9	SII1253.8
MARK817	1253.653 \pm 0.029	-35 \pm 7	27 \pm 8	53 \pm 16	21.7	SII1253.8
PKS2155-304	1259.848 \pm 0.028	-155 \pm 7	31 \pm 9	76 \pm 23	8.5	SiII+FeII1260.5

Table 8. Intrinsic Ly α features with $SL \geq 4\sigma$.

Target	Wavelength (Å)	Velocity (km s ⁻¹)	b (km s ⁻¹)	\mathcal{W} (mÅ)	SL (σ)	z
AKN120	1252.135 \pm 0.034	-907 \pm 8	28 \pm 11	18 \pm 7	5.1	0.03000 \pm 0.00003
ESO141-G55	1257.716 \pm 0.029	-733 \pm 7	53 \pm 38	18 \pm 20	5.7	0.03459 \pm 0.00002
ESO141-G55	1258.093 \pm 0.023	-643 \pm 5	46 \pm 3	353 \pm 11	116.3	0.03490 \pm 0.00002
FAIRALL9	1268.850 \pm 0.029	-688 \pm 7	81 \pm 22	32 \pm 12	11.2	0.04375 \pm 0.00002
FAIRALL9	1269.351 \pm 0.029	-570 \pm 7	46 \pm 19	16 \pm 9	5.4	0.04416 \pm 0.00002
FAIRALL9	1269.731 \pm 0.029	-480 \pm 7	99 \pm 3	74 \pm 7	26.7	0.04447 \pm 0.00002
FAIRALL9	1270.288 \pm 0.032	-349 \pm 8	89 \pm 12	93 \pm 16	32.2	0.04493 \pm 0.00003
FAIRALL9	1270.746 \pm 0.027	-241 \pm 6	11 \pm 11	11 \pm 6	4.2	0.04531 \pm 0.00002
FAIRALL9	1270.955 \pm 0.029	-191 \pm 7	42 \pm 5	55 \pm 9	20.3	0.04548 \pm 0.00002
MARK279	1249.023 \pm 0.036	-923 \pm 9	43 \pm 12	22 \pm 8	7.5	0.02744 \pm 0.00003
MARK279	1251.056 \pm 0.025	-436 \pm 6	99 \pm 3	646 \pm 18	240.5	0.02911 \pm 0.00002
MARK279	1251.261 \pm 0.029	-387 \pm 7	19 \pm 10	17 \pm 10	6.6	0.02928 \pm 0.00002
MARK279	1251.694 \pm 0.023	-284 \pm 5	71 \pm 3	322 \pm 14	123.9	0.02963 \pm 0.00002
MARK279	1253.051 \pm 0.023	41 \pm 6	25 \pm 5	115 \pm 65	45.3	0.03075 \pm 0.00002
MARK279	1253.284 \pm 0.031	97 \pm 7	51 \pm 12	375 \pm 117	146.8	0.03094 \pm 0.00003
MARK279	1253.861 \pm 0.040	235 \pm 10	26 \pm 6	94 \pm 53	35.4	0.03142 \pm 0.00003
MARK290	1248.079 \pm 0.028	-850 \pm 7	20 \pm 9	22 \pm 9	4.9	0.02666 \pm 0.00002
MARK290	1249.349 \pm 0.029	-545 \pm 7	50 \pm 26	25 \pm 23	6.4	0.02770 \pm 0.00002
MARK290	1249.579 \pm 0.029	-490 \pm 7	97 \pm 12	225 \pm 48	60.4	0.02789 \pm 0.00002
MARK290	1251.115 \pm 0.039	-122 \pm 9	99 \pm 3	475 \pm 37	185.6	0.02916 \pm 0.00003
MARK290	1251.664 \pm 0.025	9 \pm 6	50 \pm 4	105 \pm 17	45.2	0.02961 \pm 0.00002
MARK290	1252.109 \pm 0.029	116 \pm 7	61 \pm 12	71 \pm 17	31.3	0.02997 \pm 0.00002
MARK290	1252.479 \pm 0.029	204 \pm 7	35 \pm 6	33 \pm 10	14.5	0.03028 \pm 0.00002
MARK290	1254.353 \pm 0.029	653 \pm 7	81 \pm 29	50 \pm 24	17.3	0.03182 \pm 0.00002
MARK290	1254.653 \pm 0.029	725 \pm 7	35 \pm 14	24 \pm 12	7.8	0.03207 \pm 0.00002
MARK290	1254.953 \pm 0.029	797 \pm 7	23 \pm 13	16 \pm 10	4.8	0.03231 \pm 0.00002
*MARK501	1254.773 \pm 0.029	-434 \pm 7	99 \pm 3	70 \pm 28	5.4	0.03217 \pm 0.00002
*MARK509	1255.795 \pm 0.029	-403 \pm 7	46 \pm 5	132 \pm 67	64.4	0.03301 \pm 0.00002
*MARK509	1256.065 \pm 0.029	-339 \pm 7	44 \pm 14	76 \pm 92	37.9	0.03323 \pm 0.00002
*MARK509	1256.285 \pm 0.029	-286 \pm 7	93 \pm 31	505 \pm 425	147.7	0.03341 \pm 0.00002
*MARK509	1257.165 \pm 0.029	-76 \pm 7	69 \pm 21	191 \pm 229	61.9	0.03413 \pm 0.00002
*MARK509	1257.365 \pm 0.029	-29 \pm 7	65 \pm 62	265 \pm 318	121.5	0.03430 \pm 0.00002

Table 8—Continued

Target	Wavelength (Å)	Velocity (km s ⁻¹)	b (km s ⁻¹)	\mathcal{W} (mÅ)	SL (σ)	z
*MARK509	1257.605 \pm 0.029	29 \pm 7	44 \pm 16	140 \pm 168	73.7	0.03450 \pm 0.00002
*MARK509	1257.785 \pm 0.029	71 \pm 7	28 \pm 17	26 \pm 32	13.9	0.03464 \pm 0.00002
*MARK509	1257.985 \pm 0.029	119 \pm 7	72 \pm 25	449 \pm 240	238.6	0.03481 \pm 0.00002
MARK817	1249.477 \pm 0.041	-1023 \pm 10	26 \pm 9	36 \pm 17	13.8	0.02781 \pm 0.00003
MARK817	1249.694 \pm 0.077	-971 \pm 18	28 \pm 21	20 \pm 19	7.7	0.02799 \pm 0.00006
MARK817	1251.752 \pm 0.025	-479 \pm 6	18 \pm 7	14 \pm 4	6.0	0.02968 \pm 0.00002

5. CfA Galaxy pie diagrams

The very local redshift range of this absorption line survey ($cz \leq 20,000 \text{ km s}^{-1}$), allows us to present an immediate “first look” at the relationship between local Ly α absorbers and galaxies using bright galaxy redshift information currently available. Several surveys are complete to $m_B \leq 15.5$ over large sky areas (e.g., Huchra et al. 1992; Marzke, Huchra, & Geller 1996; Grogin & Geller 1998; Huchra, Vogele, & Geller 1999; Da Costa et al. 1998). Seven of our targets lie in the sky areas of these surveys (3C 273, IZW1, Mrk 335, Mrk 421, Mrk 501, Q 1230+011 and PKS 2155-304). All of these redshifts surveys are included in the latest (Feb 8, 2000) on-line version of the CfA Redshift Catalogue (Huchra et al. 1992) so that the environments of the Ly α absorbers found along these sightlines can be investigated using available data. Also, pencil-beam surveys have been conducted along several sightlines to address the relationship between galaxies and Ly α clouds using smaller numbers of absorbers than presented herein (e.g., Morris et al. 1993; Tripp, Lu, & Savage 1998a). In Paper III, we will use our Ly α survey and all available galaxy redshift survey data to investigate the relationship between Ly α clouds and galaxies. One advantage of the current work is that the absorber redshifts are known to much better accuracy (i.e., $\pm 10 \text{ km s}^{-1}$ compared to $\pm 200 \text{ km s}^{-1}$) than the absorbers detected in the QSO Absorption Line Key Project, which used the FOS at 1 Å resolution.

In Figures 21-35, we present heliocentric “pie diagrams” (right ascension [RA, α] or declination [DEC, δ] versus heliocentric radial velocity) for all 15 HST targets in our GHRS survey. These pie diagrams indicate the spatial positions of the CfA Redshift Catalogue galaxies relative to our target sightlines and the detected Ly α absorbers, assuming a pure Hubble flow. The 2000 February 8 version of this catalog (Huchra et al. 1992) contains $\sim 120,000$ galaxies with velocities less than $100,000 \text{ km s}^{-1}$. We present pie diagram in $\pm 7^\circ$ extent as a 2D representation of the 3D distribution of the known low- z galaxy distribution. The sightline towards each target is indicated by the dashed line that starts at the apex of each pie diagram (the Sun) and terminates with either a large circle, indicating the position of the HST target, or with a dashed arrow indicating that target lies off the pie diagram. Each CfA galaxy is indicated by a “c”. CfA galaxies that have a sightline impact parameter less than $1 h_{70}^{-1} \text{ Mpc}$ are indicated by “v”s (the **v** indicates that the galaxy is **very** close to the sightline). The orientation of the ‘v’'s and ‘c’'s are preserved between the RA and DEC versions of the pie diagrams.

In the previous sections, all Ly α absorber velocities were reported in the LSR velocity scale, established by aligning the velocity centroids of the Galactic S II $\lambda\lambda 1250, 1253, 1259$ absorption lines with the dominant Galactic H I emission. We selected this velocity scale instead of the HST+GHRS wavelength solution due to the possibility of an improper wavelength scale caused by poor target centering in the large science aperture (LSA). To convert our LSR Ly α absorber velocities to heliocentric velocities, we assumed that the solar velocity with respect to LSR is $+20.0 \text{ km s}^{-1}$ towards ($\alpha=18:03:50.3$; $\delta=+30:00:17$, J2000). The heliocentric velocities of our definite Ly α absorbers ($SL \geq 4\sigma$), if present, are indicated on the pie diagrams by medium-sized

dashed circles. Possible Ly α absorbers ($3\sigma \leq SL < 4\sigma$), if present, are indicated by small dashed circles. If the target is present within the pie diagram, its location is given by a large circle; otherwise a dashed arrow indicates that the target is beyond the limit of the pie diagram.

Also in Appendix B, Table 10 lists the nearest 3 galaxies for all Ly α absorbers in our $SL \geq 3\sigma$ sample. For each absorber, we indicate absorber type (D=definite, or P=possible), heliocentric absorber velocity in km s $^{-1}$, name of the nearest galaxy, distance (D_{\perp}) from the galaxy to the line of sight (LOS) in h_{70}^{-1} Mpc, heliocentric recession velocity (cz) of the galaxy, distance (D_{cz}) along the LOS from the absorber to the galaxy allowing for peculiar velocities of ± 300 km s $^{-1}$, the Euclidean 3D absorber-galaxy distance (D_{tot}), and the Zwicky blue (B) magnitude of the galaxy (if available). All information on galaxy location, velocity, or magnitude is taken from the CfA redshift survey unless otherwise indicated. The use of a “retarded” Hubble flow accounts for peculiar galaxy motion and galaxy rotation and always decreases the reported LOS and total absorber-galaxy distances. With our “retarded Hubble flow” peculiar velocity allowance, we consider any Galaxy within ± 300 km s $^{-1}$ of the recession velocity of an absorber to be at the same distance as the absorber (see S95 for justification of this somewhat arbitrary ± 300 km s $^{-1}$ allowance). In Paper III, we will use the data presented here to quantify the environment of local Ly α clouds.

6. Conclusion

This paper is the first in a series devoted to a detailed study of the “local Ly α forest” using observations obtained with the Hubble Space Telescope (HST) and Goddard High Resolution Spectrometer (GHRS) in its medium resolution mode (G160M grating). The current paper has presented a detailed description of the target selection, observational strategy and data reduction (§ 2), along with a presentation of the reduced spectra and lists of the all absorption lines detected (§ 4 and Appendix A). We discovered 81 definite ($\geq 4\sigma$) and 30 possible ($3 - 4\sigma$) intervening Ly α absorption lines along with numerous Galactic metal lines, including metal absorption from several “high-velocity clouds”, and a few absorption systems judged to be “intrinsic” to the target AGN. In Paper II of this series we will present a detailed analysis of the absorption line data presented herein, including the “ b -value” distribution, the column density distribution, and the two-point correlation function for local Ly α absorbers. In Paper III we will present an analysis of the relationship between these Ly α absorbing clouds and galaxies based upon the bright galaxy survey data also presented herein. The low- z galaxy redshift survey data presented in the form of “pie diagrams” in § 5 and Appendix B provide a valuable “first look” at the relationship between the local Ly α clouds and bright galaxies. In Paper IV we will present the two-point correlation function of the low- z Ly α forest based upon the HST/GHRS data presented here and 13 additional HST/STIS sightlines obtained in Cycle 7.

The GHRS+G160M observing combination has two primary advantages for doing this study: (1) it is sensitive to the weakest Ly α absorbers detected at low- z thus far ($\log N_{\text{HI}} \geq 12.5$; comparable to the weakest lines found in the high- z Ly α forest with the Keck Telescope); and (2) the

$\sim 19 \text{ km s}^{-1}$ spectral resolution resolves almost all of the $\text{Ly}\alpha$ lines detected. This combination also yields extremely accurate velocities for detected absorbers ($\leq 10 \text{ km s}^{-1}$). The disadvantages of this approach are that only the UV-brightest AGN in the sky are possible targets for this work (typically $V \leq 14.5$) and that only a small pathlength can be observed with this spectrograph configuration. The fifteen GHRS target sightlines sample only $116,000 \text{ km s}^{-1}$ of total pathlength for $\text{Ly}\alpha$ absorber detection (details of the pathlength surveyed as a function of H I column density are presented in Paper II). However, the discovery of a large number of $\text{Ly}\alpha$ absorbers by this GHRS survey makes it clear that the observational approach adopted here of obtaining the highest resolution spectra possible to investigate the local $\text{Ly}\alpha$ forest has been successful. Furthermore, even though the total observed pathlength is small compared to other $\text{Ly}\alpha$ surveys, the pathlength observed by this work is the most important piece of any individual sightline, the nearest $\sim 10,000 \text{ km s}^{-1}$. This has enabled the discovery of the nearest $\text{Ly}\alpha$ absorbers and given us the opportunity to relate these clouds to the nearest known galaxies.

Owing to the success of this GHRS survey, our group has obtained HST + Space Telescope Imaging Spectrograph (STIS) spectra of an additional 13 UV bright targets to complete our survey of the low- z , low- N_{HI} local $\text{Ly}\alpha$ forest. The STIS observations will be presented in a later paper.

For their assistance in obtaining the HST/GHRS data over several cycles, we are grateful to the staff at the Space Telescope Science Institute, particularly Ray Lucas. We would like to thank Brad Gibson for his assistance in deciphering the HVCs and his helpful discussions on b -values. In addition, we would like to thank Mark Giroux and Greg Bothun for their helpful comments on this manuscript. This work was supported by HST guest observer grant GO-06593.01-95A, the HST COS project (NAS5-98043), and by the Astrophysical Theory Program (NASA grant NAGW-766 and NSF grant AST96-17073).

A. GHRS/G160M Spectra and Absorption Line Lists

In this Appendix we present composite HST/GHRS/G160M spectra, and line lists (Table 9) describing the detected absorption features. Descriptions of features in these data unique to individual objects are presented in § 3 of the text.

The GHRS/G160M spectra, error vectors, and pathlength accountings are presented in Figures 5–20 for all targets. The upper panel of each figure presents the composite HST/GHRS/G160M spectrum and the 1σ error values, which are plotted below the flux vector. As discussed in § 2.3.5, our list of intergalactic Ly α absorbers is restricted to those more than 1,200 km s $^{-1}$ blueward of the target Ly α emission. This limit is indicated by the dashed vertical line in the upper and middle panels of the figures. All non-Galactic features redward of this line are classified as intrinsic absorbers. All otherwise unidentified absorption features blueward are taken to be intergalactic Ly α absorption features, and are indicated by a solid vertical line above the feature. Ly α absorbers with significance level (SL) $> 4\sigma$ (definite absorbers) are plotted with a longer vertical line than the $3\sigma \leq SL < 4\sigma$ absorbers. Galactic and high-velocity cloud (HVC) absorption lines are similarly represented with a dotted line, intrinsic absorption lines with a dashed line, and intervening higher- z absorption lines with a dot-dashed line. The solid line is the global continuum fit as described in § 2.3.2.

Note specifically that in several cases where Ly α emission occurs in the observed band, the portion of the spectrum redward of the proximity limit (vertical dashed line) is excluded from the region best fitted by the continuum. Thus, any intrinsic or Galactic absorptions redward of the “proximity limit” may not have their EWs most accurately represented. A different continuum fitting procedure will be used to address these specific features in later publications. The middle panel shows the 4σ rest-frame EW (\mathcal{W}) sensitivity detection limit, per resolution element, as a function of wavelength for each target. As with the upper panel, we include in our statistics only the portion of the spectrum that lies $> 1,200$ km s $^{-1}$ blueward of the target Ly α emission. Finally, the bottom panel of each figure summarizes the available pathlength for inclusion in our sample and line statistics. The row marked ‘**I**’ indicates the portion of the spectrum removed due to specific features intrinsic to the target or non-Ly α lines associated with known intervening systems at higher redshift not associated with the target AGN. The pathlength removed due to higher redshift intervening absorbers is indicated by a double line to differentiate it from that removed due to intrinsic absorption features. The other rows are marked as follows: ‘**G**’ indicates pathlength attributed to non-HVC Galactic features such as S II $\lambda\lambda$ 1250, 1253, 1259, ‘**H**’ indicates pathlength attributed to HVCs, ‘**L**’ indicates the portion of the spectrum that is redward of $cz_{\text{em}} - 1,200$ km s $^{-1}$, and ‘**F**’ indicates those regions of the spectrum that are available for the detection of intergalactic Ly α absorbers. The ‘**F**’ row also corrects for our inability to correctly detect and model features near the edge of our wavelength coverage; we remove 10 pixels on the edges of our wavelength coverage. Only for H 1821+643 does the intrinsic/intervening ‘**I**’ accounting remove any significant pathlength not already removed by the ‘**L**’ row.

For a few objects, the $cz_{\text{em}} - 1,200 \text{ km s}^{-1}$ “proximity limit” lies within the observed spectral band and is indicated by a dashed vertical line. For targets with strong intrinsic Ly α emission (Akn 120, ESO 141-G55, Fairall 9, Mrk 279, Mrk 290, Mrk 335, and Mrk 509), fluxes are scaled differently above and below this convenient breakpoint. For these spectra, the left axis corresponds to flux blueward of the proximity limit, while the right axis corresponds to flux redward of this limit.

The line lists for each individual spectrum are presented sequentially in Table 9. The first column of Table 9 indicates the LSR-adjusted wavelength and wavelength uncertainty for each feature. The wavelength scale of each spectrum was corrected to the LSR using the Galactic H I and S II lines (1250, 1253, and 1259 Å, if available). The second column lists the non-relativistic velocity (cz in km s^{-1}) relative to the LSR. For Ly α absorbers judged to be intrinsic to the AGN, velocities are listed relative to the AGN narrow-line region (see § 2.3.5). For intervening non-Ly α absorbers, such as those found in H 1821+643, this column reports the redshift (z) of the absorber. We also provide velocity or redshift uncertainties, based upon the total wavelength uncertainties (see § 2.3.3). The third column provides the single-component Doppler widths (b in km s^{-1}), and uncertainties, for each feature as estimated from the Gaussian width (\mathbf{W}_G). As explained previously, the Doppler widths have been corrected for the spectral resolution of the GHRS and the single-component Gaussian fits were restricted to the range $12 < b_{\text{obs}} < 100 \text{ km s}^{-1}$. The fourth column lists the rest-frame EW (\mathcal{W} in mÅ) and its uncertainty for each absorption feature. This uncertainty includes both the statistical error of the χ^2 fit and our conservative estimate of the systematic error in the continuum placement (see § 2.3.2). The fifth column indicates the significance level (SL in σ) of each feature. The SL is calculated by integrating the S/N (per RE) of the best fit Gaussian for each feature. The final two columns present the identification (Id) and alternative identification (Alt Id) if applicable for each feature. Absorption lines that are determined not to be intergalactic Ly α have their identifications prefaced by **g:** (Galactic), **h:** (HVC), **i:** (intrinsic), or **z:** (intervening). Alternate line identifications that lie between 0.2–0.4 Å from the expected location are indicated as speculative by the inclusion of a ? following the identification.

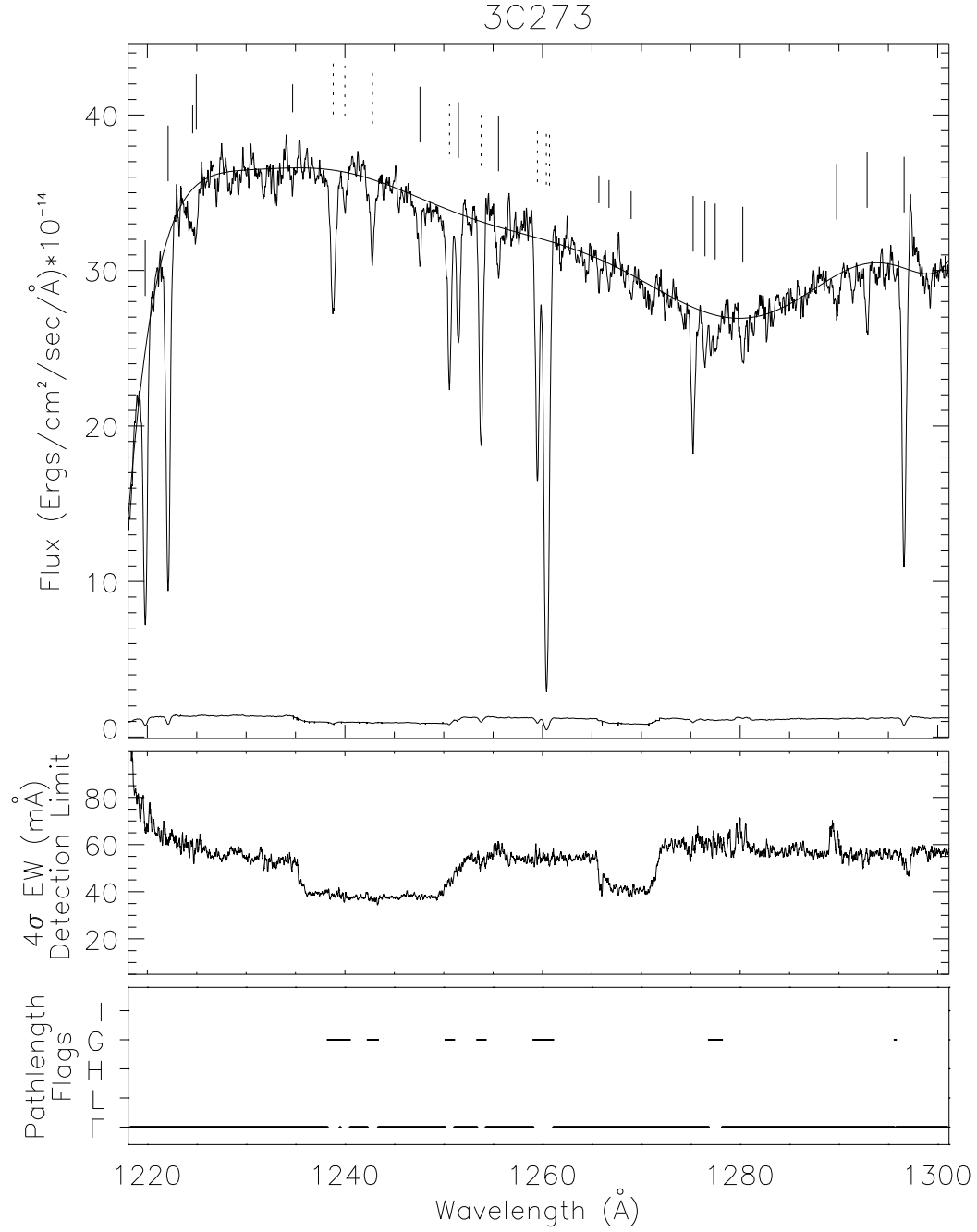


Fig. 5.— GHR/G160M 3C 273 spectrum, sensitivity limits, and pathlength flags.

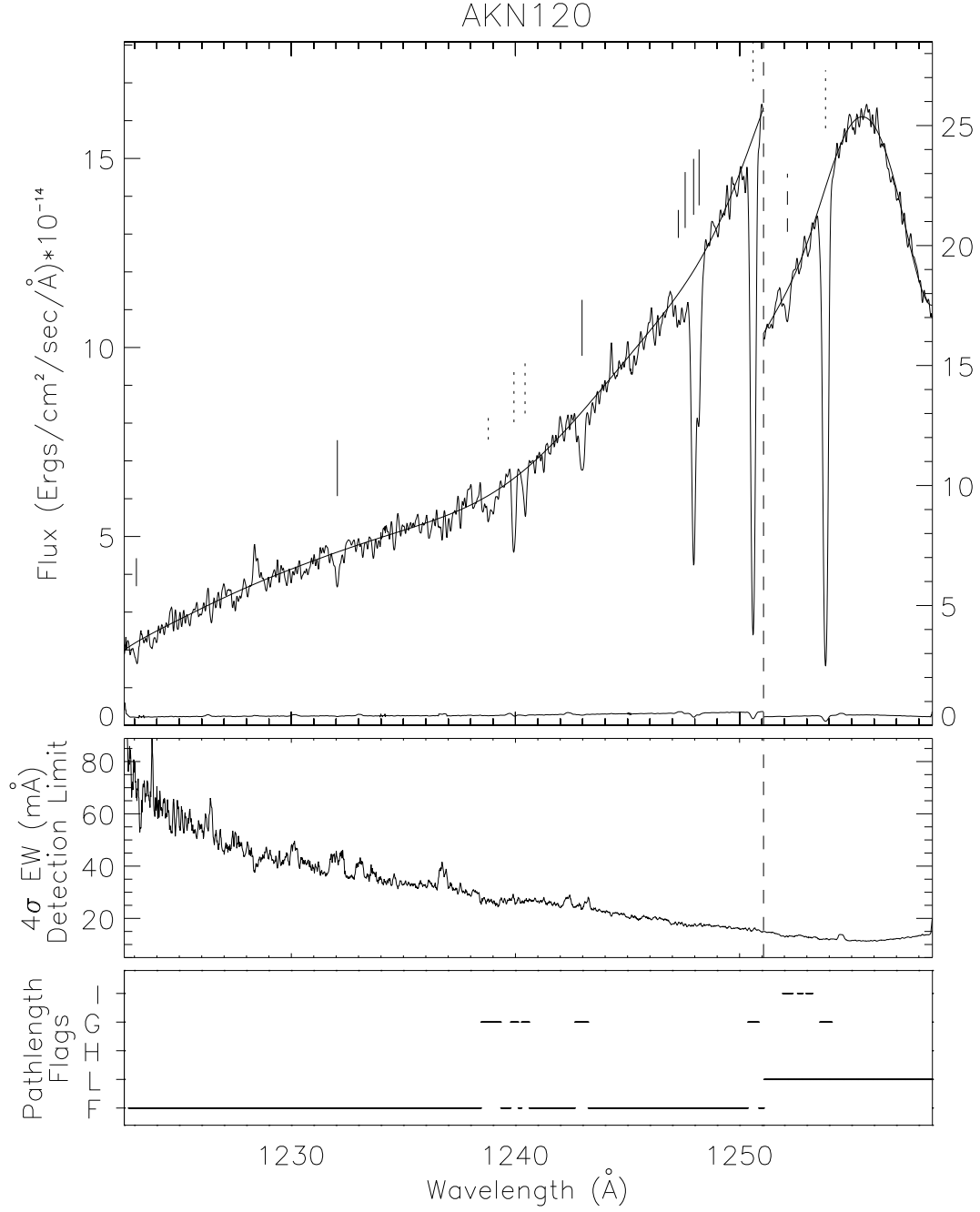


Fig. 6.— GHR/G160M Arakelian 120 spectrum. The dashed vertical line indicates the proximity limit as explained in § 2.3.5. In the upper panel, the left axis corresponds to flux blueward of the proximity limit, while the right axis corresponds to flux redward of this convenient breakpoint.

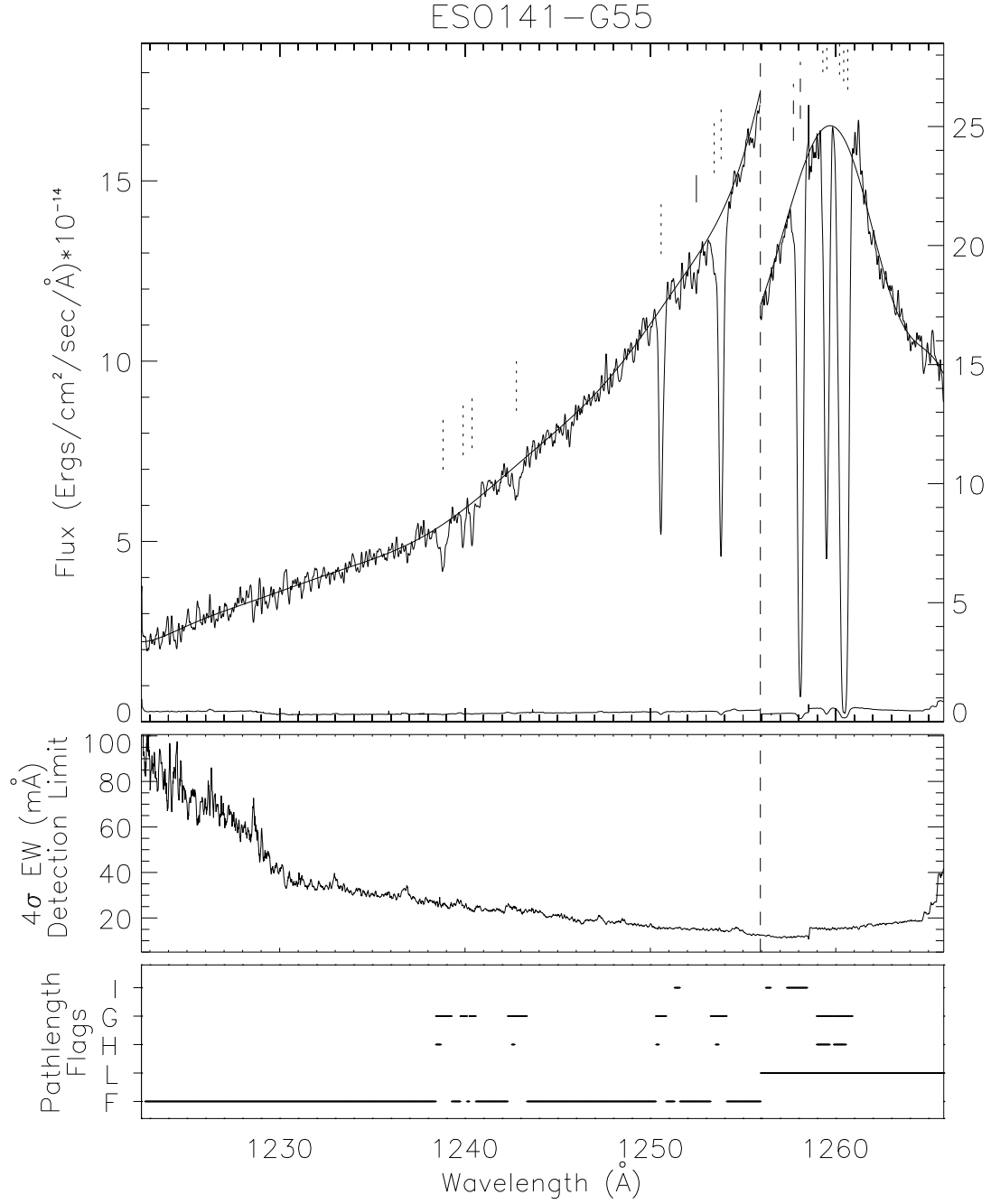


Fig. 7.— GHR/G160M ESO 141-G55 spectrum, sensitivity limits, and pathlength flags.

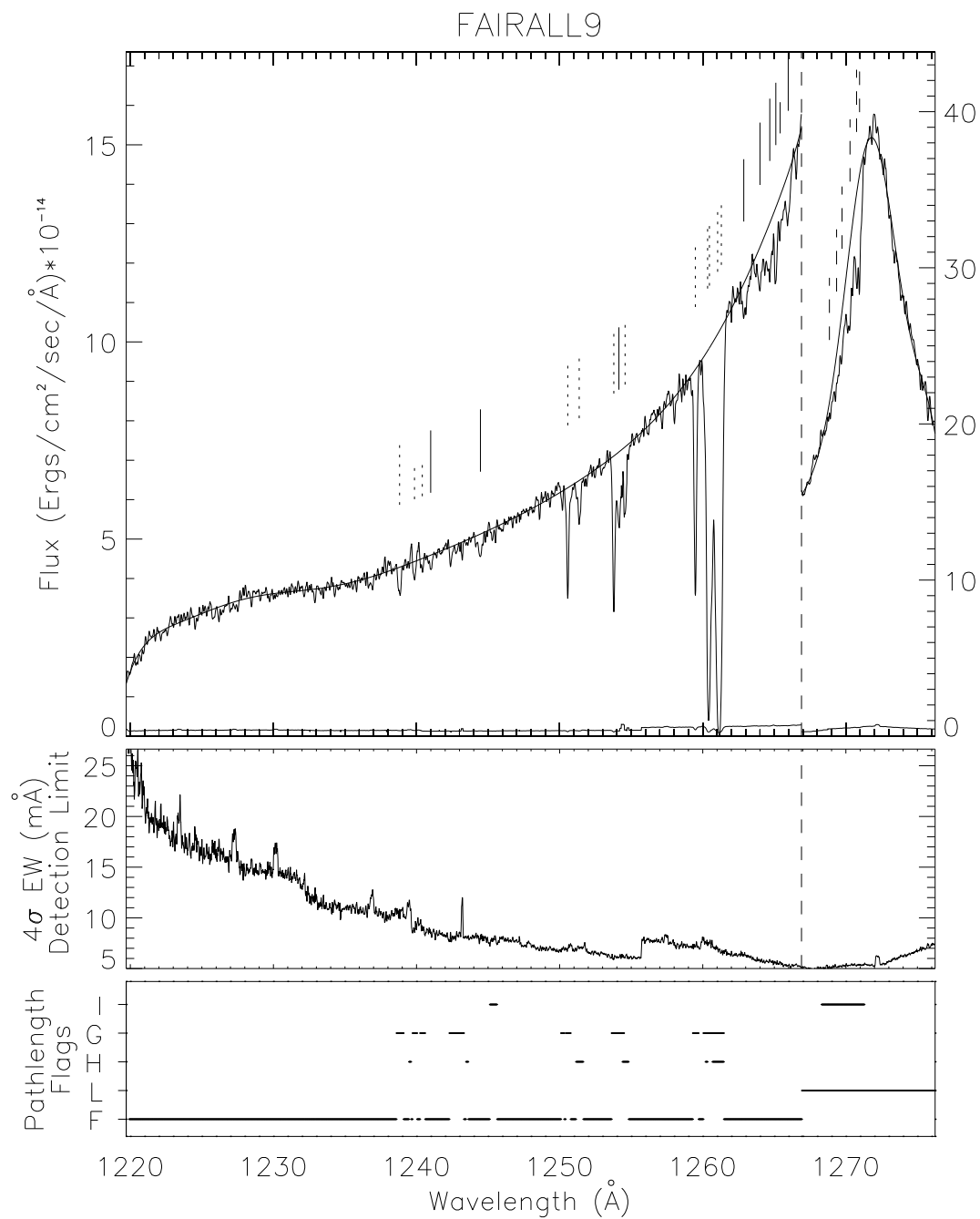


Fig. 8.— GHR/G160M Fairall 9 spectrum, sensitivity limits, and pathlength flags.

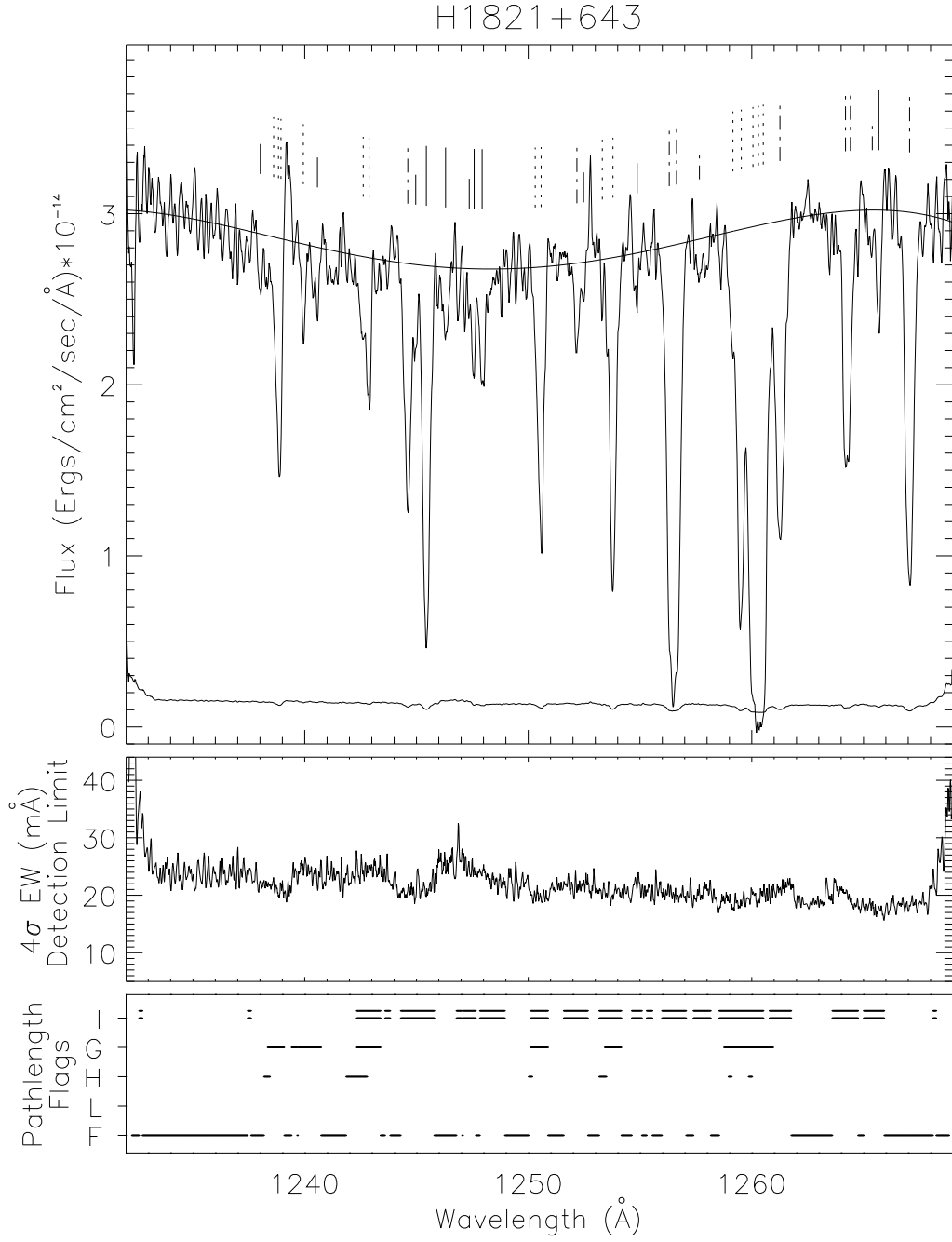


Fig. 9.— GHR/G160M H 1821+643 spectrum. Features indicated in the upper panel by a dot-dashed line are determined to be intergalactic non-Ly α lines. The double lines in the “I” row of the Pathlength Flags denotes pathlength excluded due to these intergalactic non-Ly α lines at higher cz .

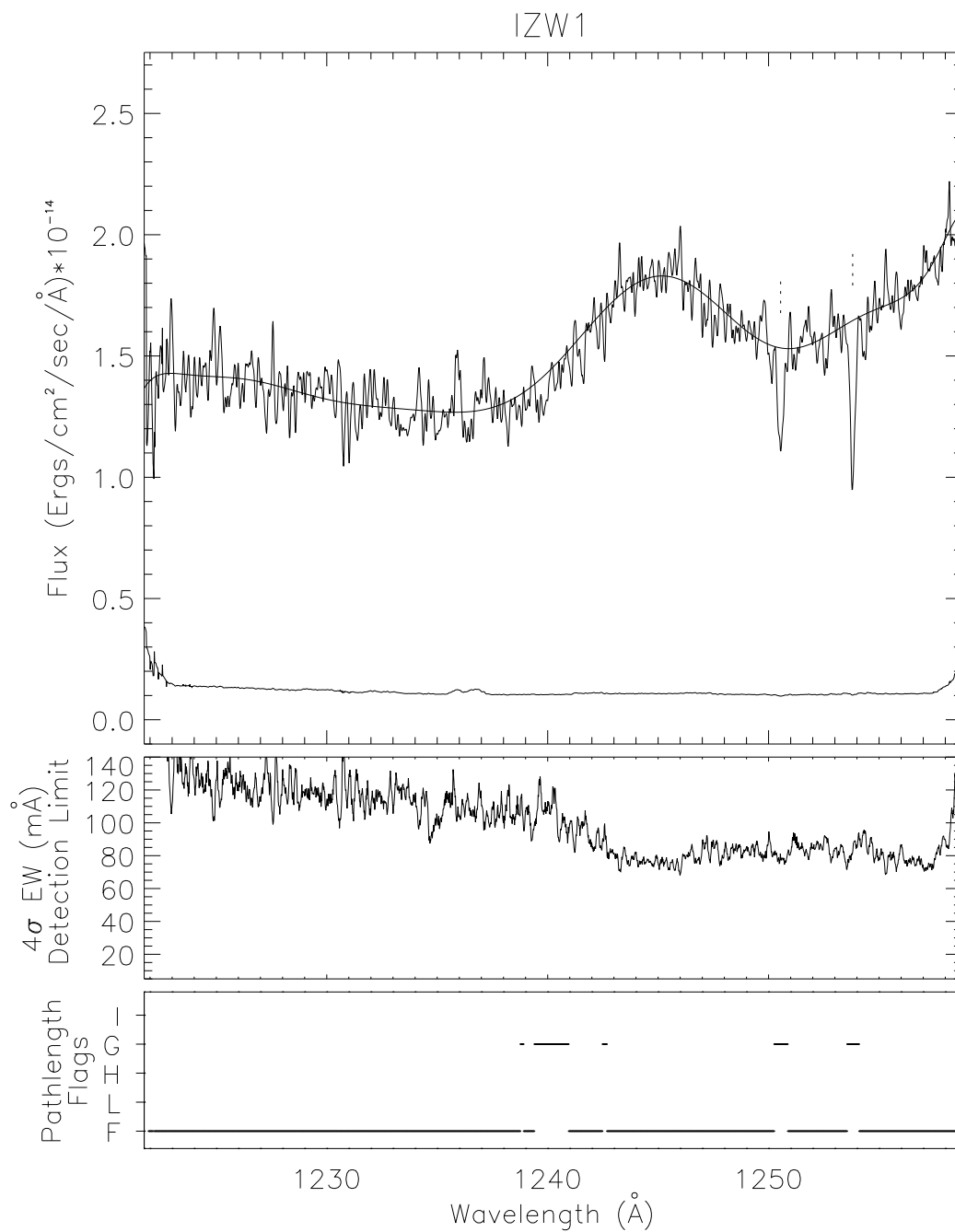


Fig. 10.— GHR/G160M I ZW 1 spectrum, sensitivity limits, and pathlength flags.

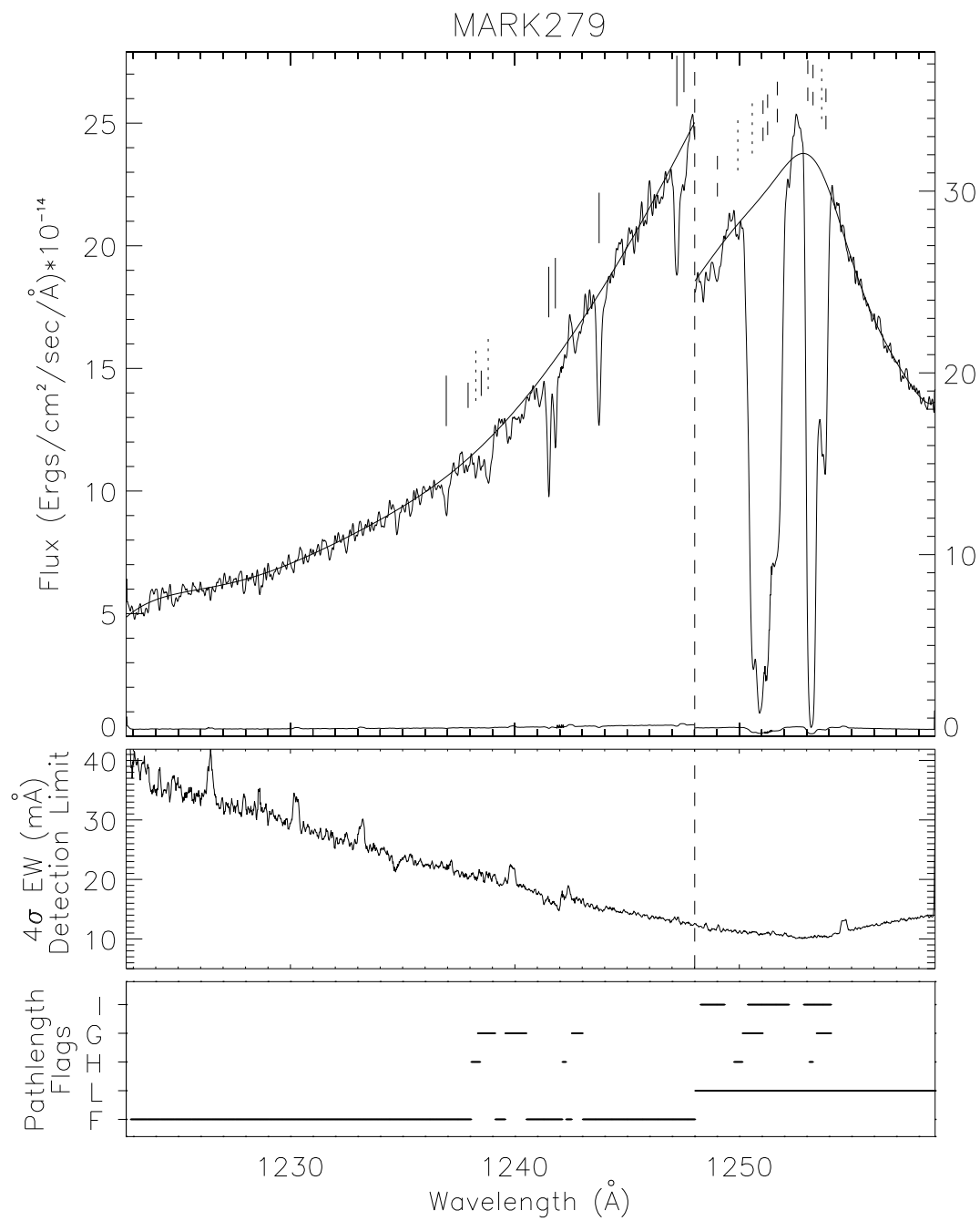


Fig. 11.— GHR/G160M Markarian 279 spectrum, sensitivity limits, and pathlength flags.

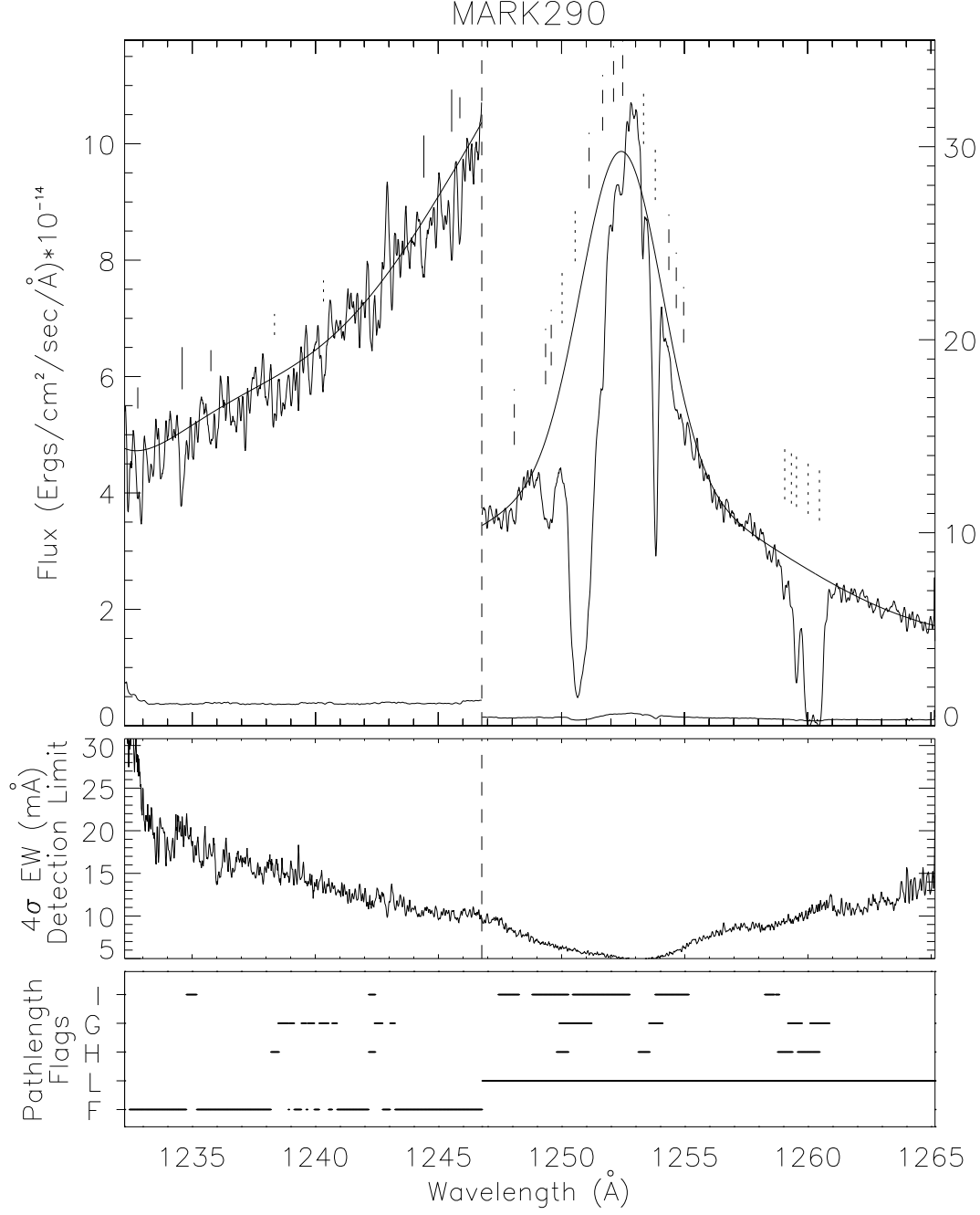


Fig. 12.— GHR/G160M Markarian 290 spectrum, sensitivity limits, and pathlength flags.

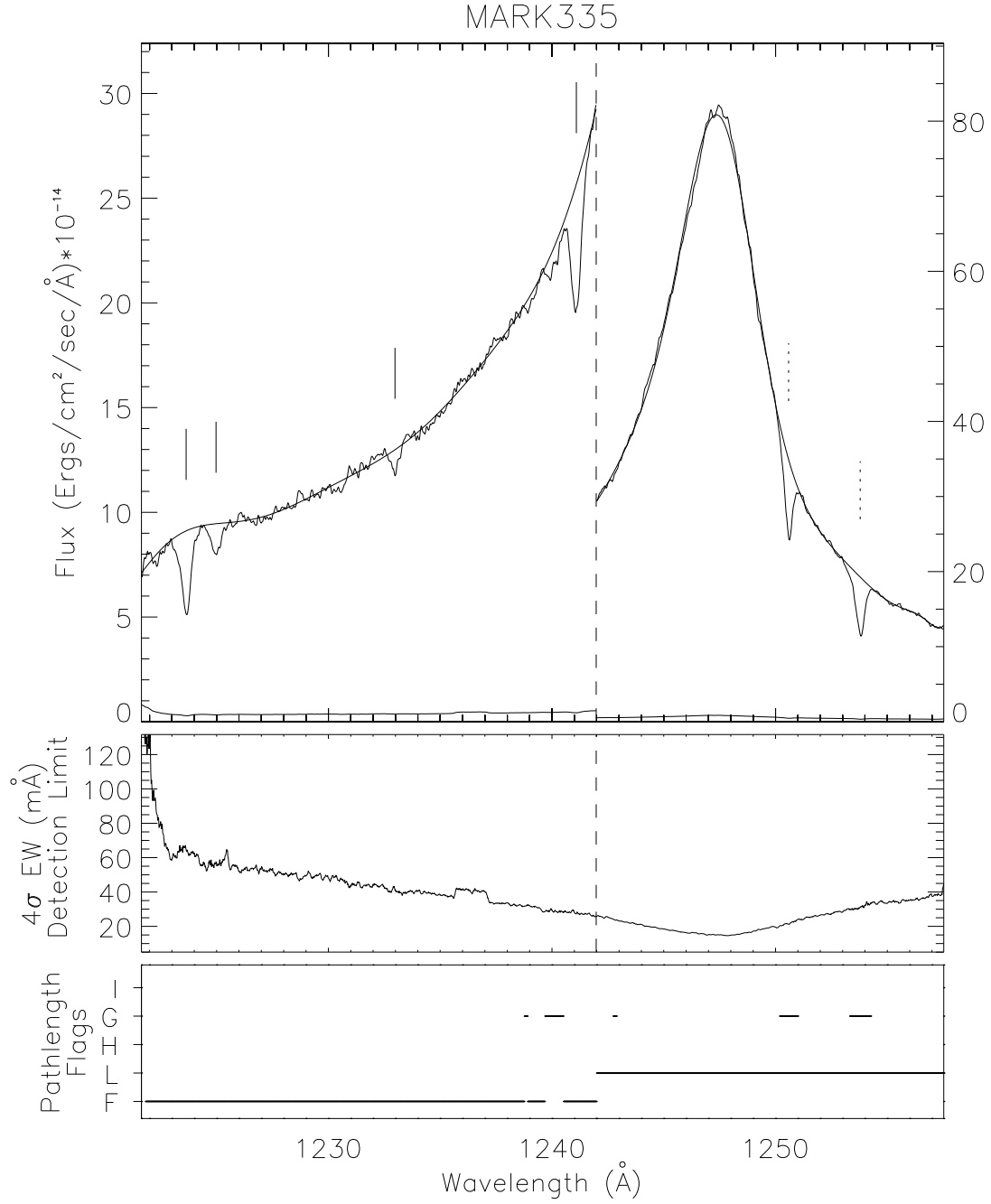


Fig. 13.— GHR/G160M Markarian 335 spectrum, sensitivity limits, and pathlength flags.

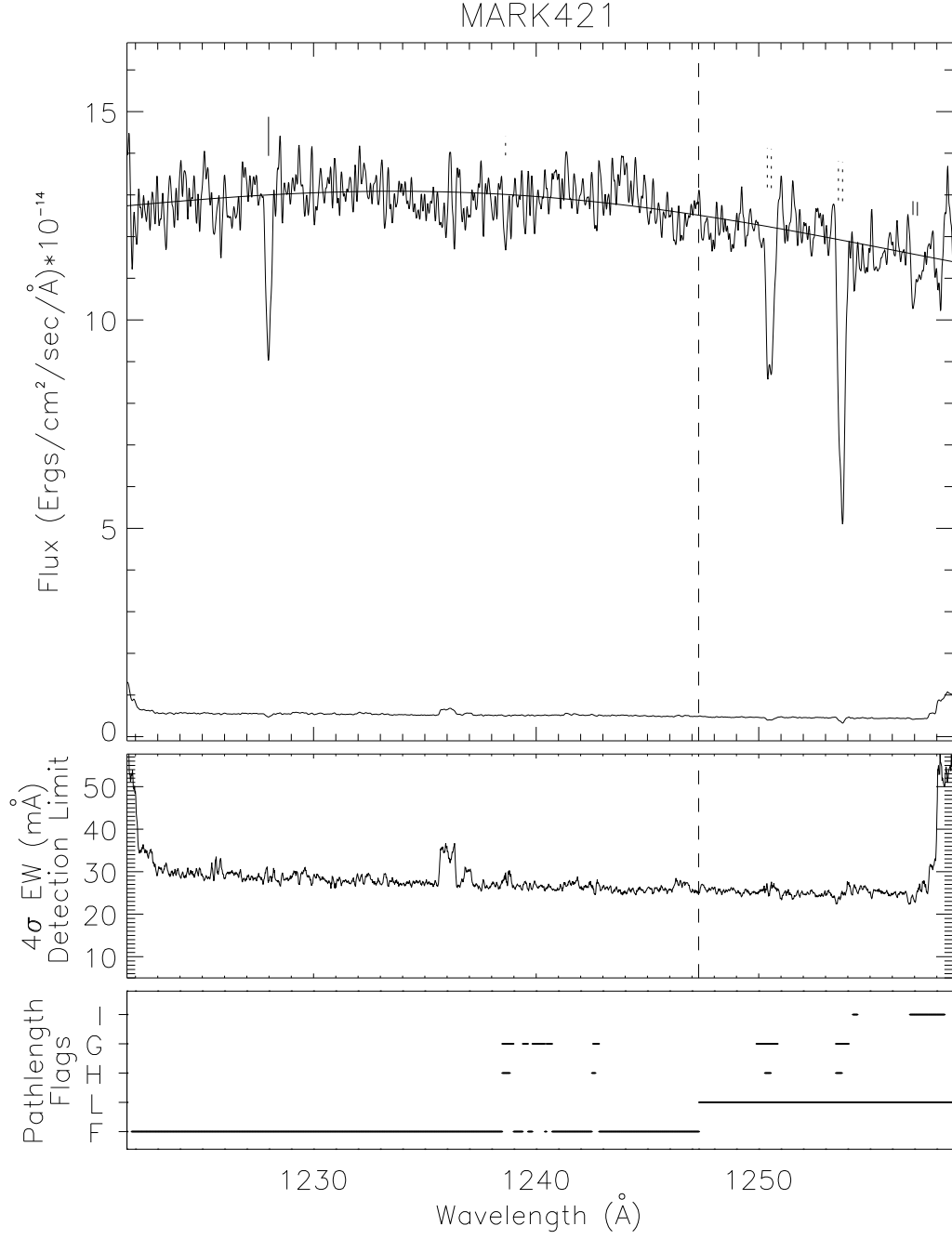


Fig. 14.— GHRS/G160M Markarian 421 spectrum, sensitivity limits, and pathlength flags.

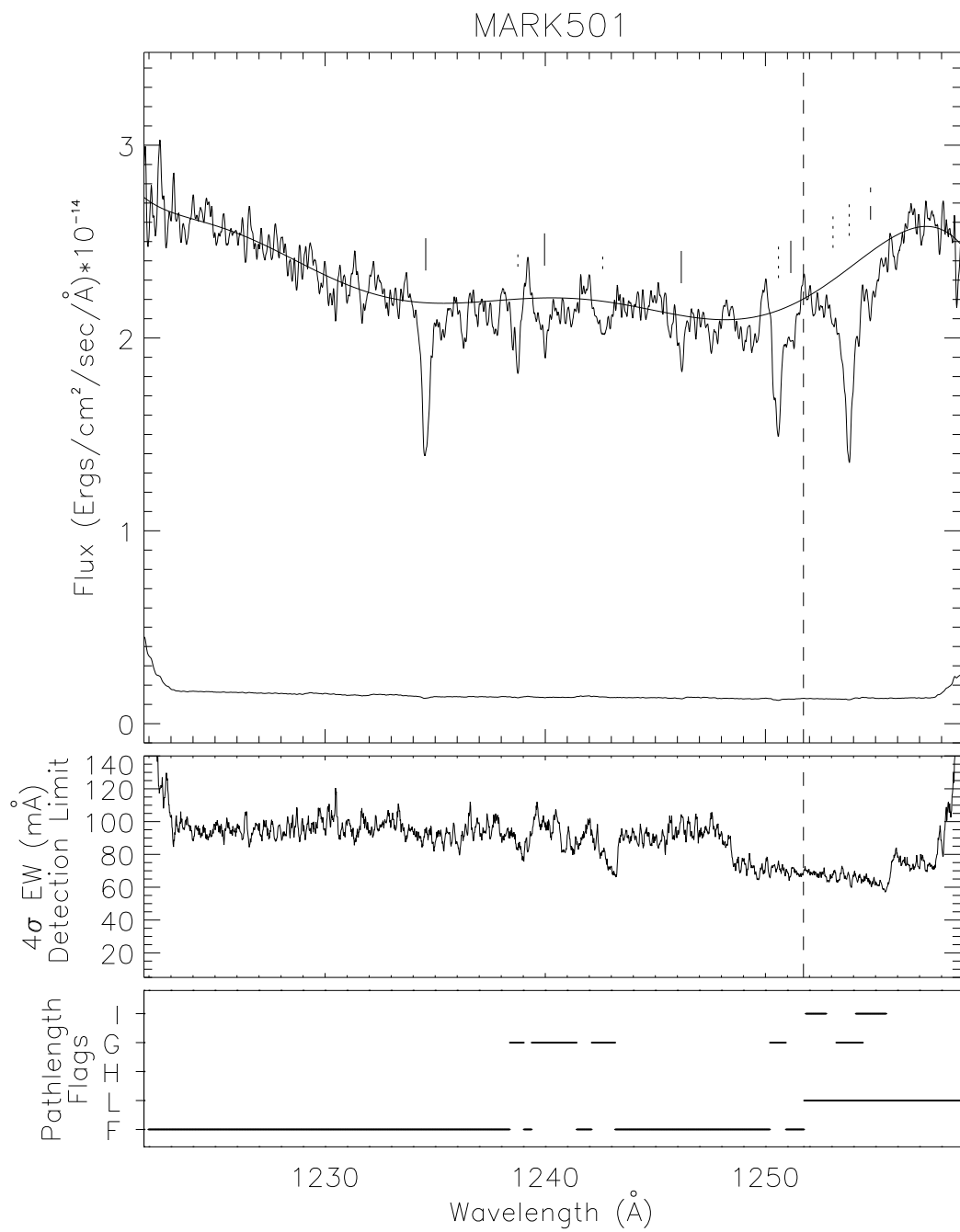


Fig. 15.— GHR/G160M Markarian 501 spectrum, sensitivity limits, and pathlength flags.

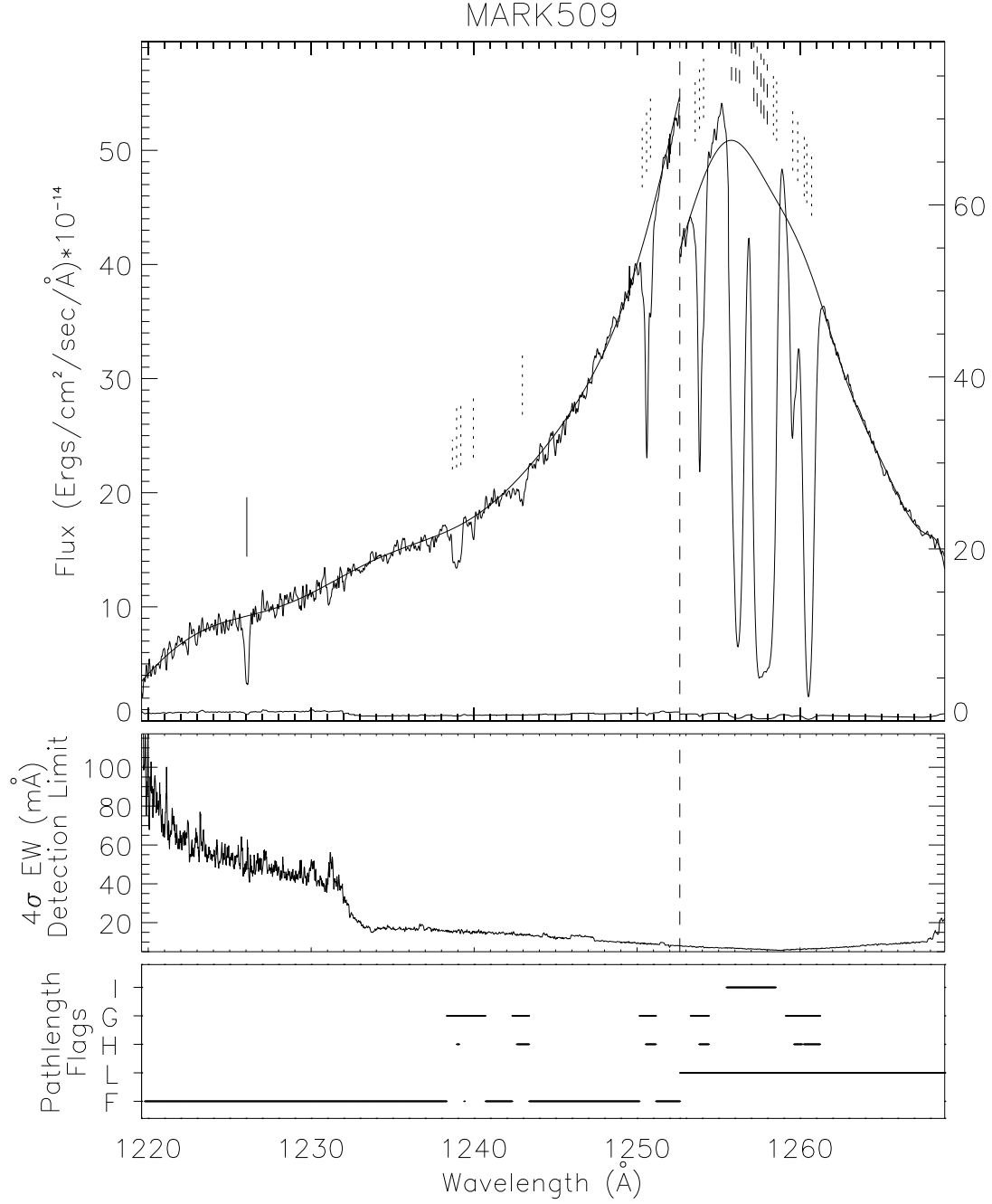


Fig. 16.— GHR/G160M Markarian 509 spectrum, sensitivity limits, and pathlength flags.

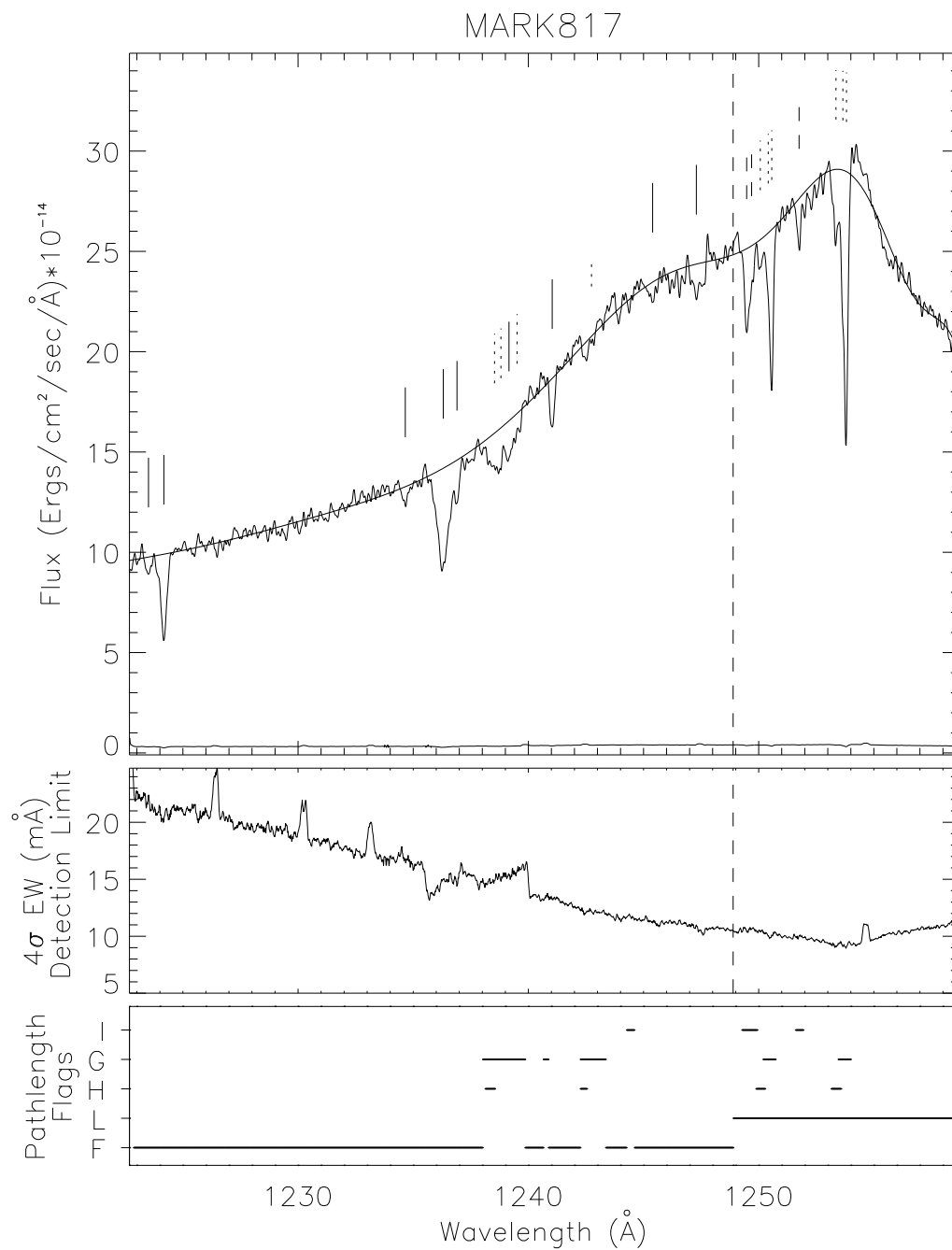


Fig. 17.— GHRs/G160M Markarian 817 spectrum, sensitivity limits, and pathlength flags.

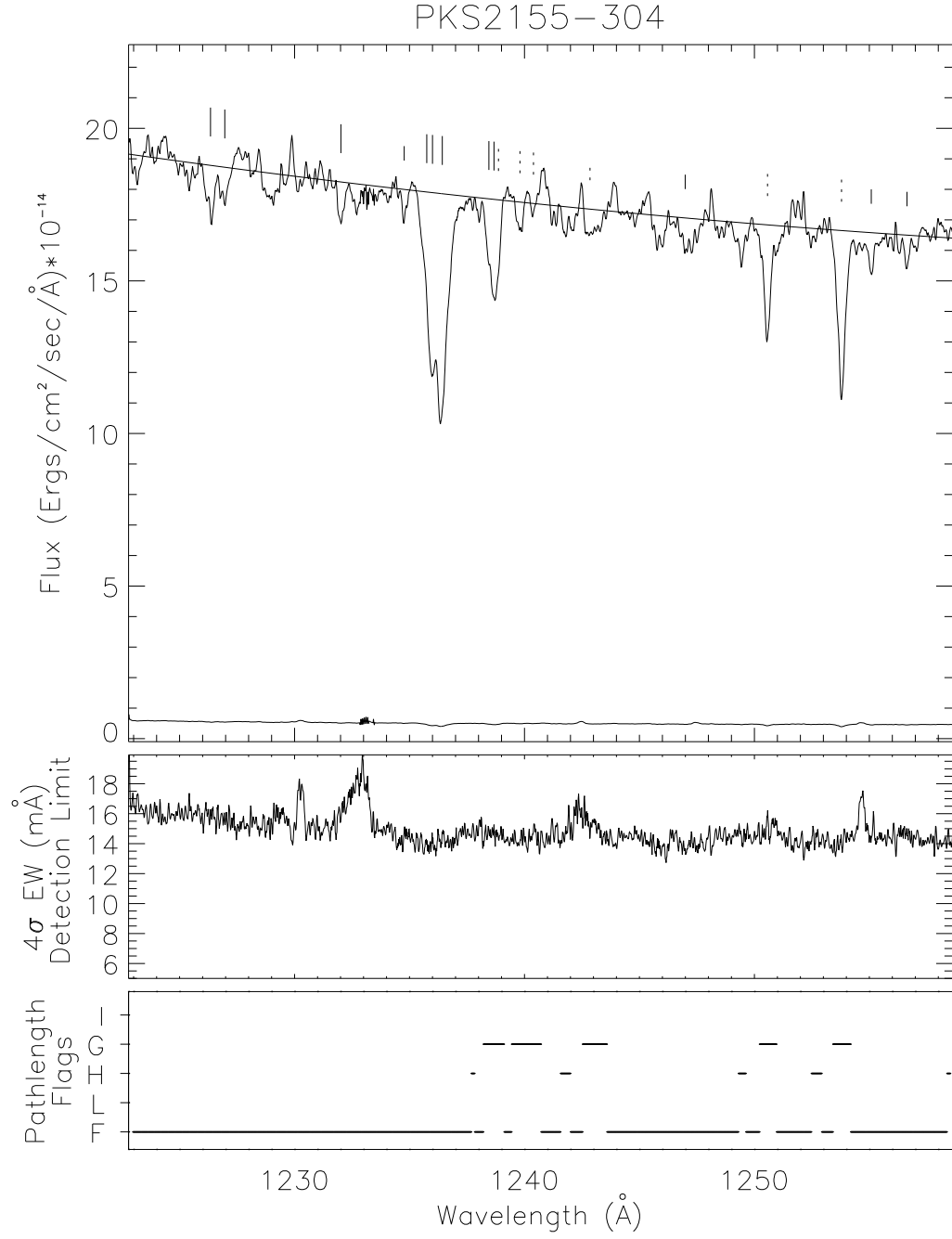


Fig. 18.— Pre-COSTAR GHRS/G160M PKS 2155-304 spectrum, sensitivity limits, and pathlength flags.

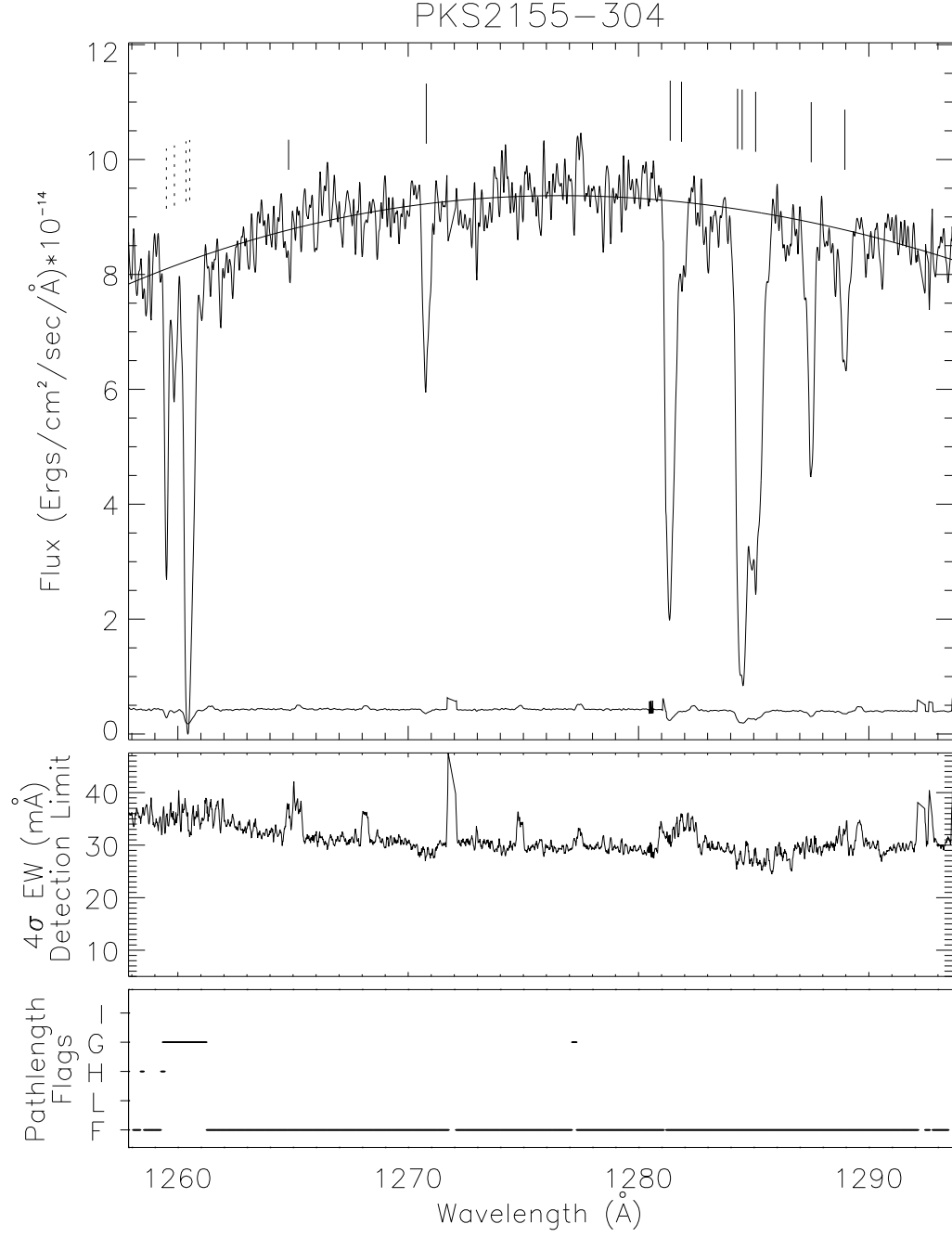


Fig. 19.— Post-COSTAR GHRS/G160M PKS 2155-304 spectrum, sensitivity limits, and path-length flags.

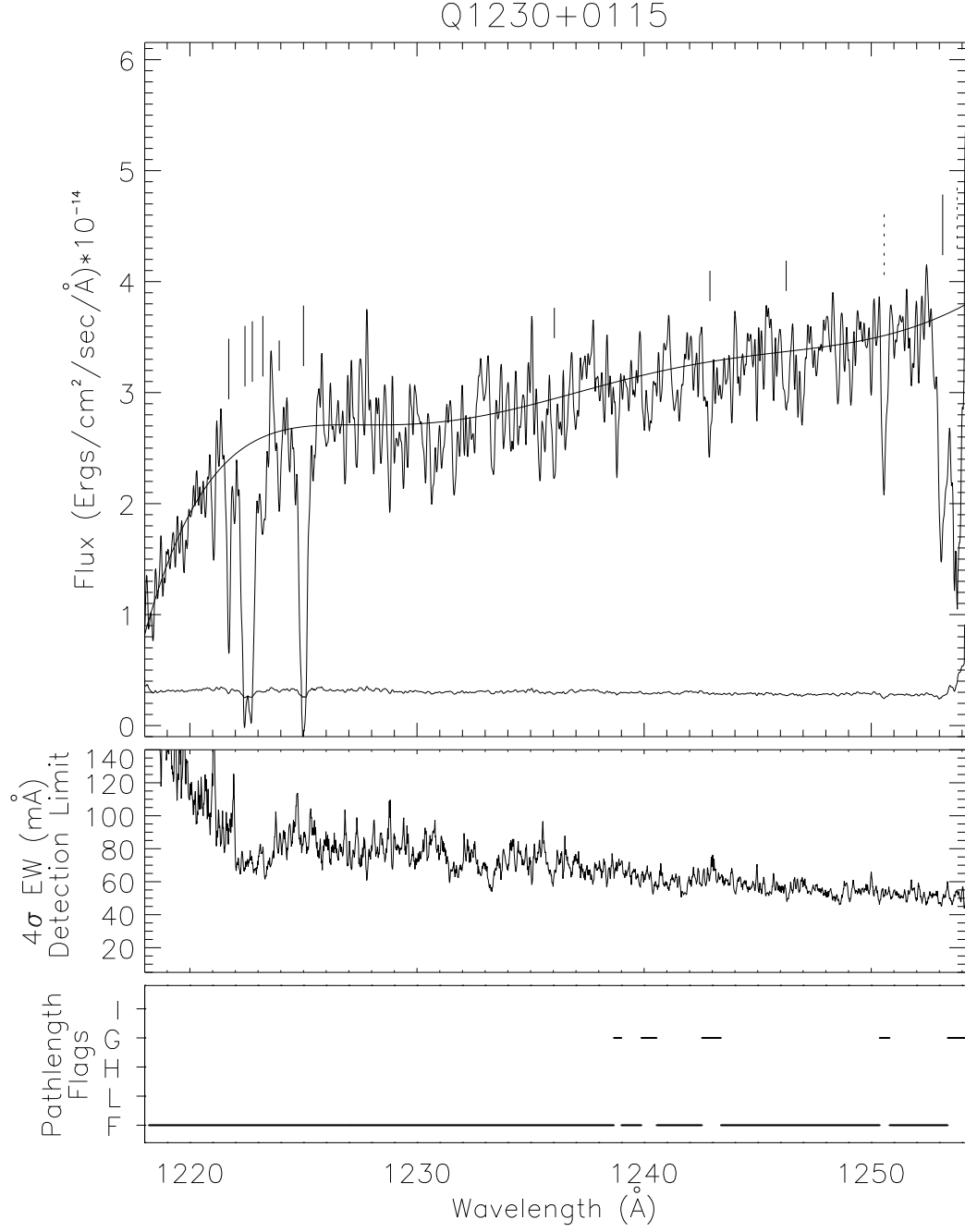


Fig. 20.— GHR/G160M Q 1230+0115 spectrum, sensitivity limits, and pathlength flags.

Table 9—Continued

Wavelength (Å)	Velocity (km s ⁻¹)	b (km s ⁻¹)	\mathcal{W} (mÅ)	SL (σ)	Id	Alt Id
1223.088 \pm 0.039	1829 \pm 10	25 \pm 17	64 \pm 48	3.7	Ly α	...
1232.052 \pm 0.034	4040 \pm 8	32 \pm 11	48 \pm 18	5.5	Ly α	...
1238.789 \pm 0.029	-8 \pm 7	28 \pm 19	29 \pm 20	3.9	g:NV1238.8	Ly α
1239.934 \pm 0.023	2 \pm 6	19 \pm 5	60 \pm 12	8.5	g:MgII1239.9	Ly α
1240.427 \pm 0.028	8 \pm 7	20 \pm 8	34 \pm 12	5.0	g:MgII1240.4	...
1242.972 \pm 0.028	6733 \pm 7	33 \pm 8	53 \pm 13	9.2	Ly α	g:NV1242.8
1247.267 \pm 0.104	7792 \pm 26	34 \pm 32	19 \pm 22	3.9	Ly α	...
1247.570 \pm 0.087	7867 \pm 21	34 \pm 35	20 \pm 25	4.3	Ly α	...
1247.948 \pm 0.023	7960 \pm 5	27 \pm 4	147 \pm 22	31.4	Ly α	...
1248.192 \pm 0.027	8020 \pm 7	23 \pm 6	65 \pm 17	14.1	Ly α	...
1250.602 \pm 0.023	4 \pm 5	31 \pm 3	224 \pm 8	57.2	g:SiII1250.6	...
1252.135 \pm 0.034	-907 \pm 8	28 \pm 11	18 \pm 7	5.1	i:Ly α	...
1253.835 \pm 0.023	6 \pm 5	34 \pm 3	258 \pm 8	80.2	g:SiII1253.8	i:Ly α
ESO 141-G55						
1238.815 \pm 0.034	-1 \pm 8	43 \pm 15	75 \pm 29	10.9	g:NV1238.8	...
1239.899 \pm 0.028	-6 \pm 7	21 \pm 9	34 \pm 12	5.0	g:MgII1239.9	...
1240.379 \pm 0.026	-4 \pm 6	19 \pm 7	36 \pm 11	5.6	g:MgII1240.4	...
1242.772 \pm 0.043	-8 \pm 10	44 \pm 15	46 \pm 19	7.2	g:NV1242.8	...
1249.932 \pm 0.036	8449 \pm 9	17 \pm 15	12 \pm 8	3.0	Ly α	...
1250.578 \pm 0.023	-2 \pm 5	33 \pm 3	146 \pm 9	35.6	g:SiII1250.6	...
1252.483 \pm 0.041	9078 \pm 10	23 \pm 16	12 \pm 7	3.1	Ly α	...
1253.444 \pm 0.038	-85 \pm 9	27 \pm 13	18 \pm 9	4.7	h:SiII1253.8	...
1253.815 \pm 0.023	1 \pm 5	37 \pm 3	199 \pm 10	50.4	g:SiII1253.8	...
1257.716 \pm 0.029	-733 \pm 7	53 \pm 38	18 \pm 20	5.7	i:Ly α	...
1258.093 \pm 0.023	-643 \pm 5	46 \pm 3	353 \pm 11	116.3	i:Ly α	...
1259.304 \pm 0.029	-47 \pm 7	48 \pm 23	23 \pm 14	5.8	h:SiII1259.5	...
1259.521 \pm 0.029	1 \pm 7	38 \pm 3	217 \pm 11	55.4	g:SiII1259.5	...
1260.204 \pm 0.029	-70 \pm 7	44 \pm 6	83 \pm 73	21.1	h:SiII+FeII1260.5	...
1260.429 \pm 0.049	-7 \pm 12	59 \pm 12	408 \pm 144	102.8	g:SiII+FeII1260.5	...
1260.650 \pm 0.026	36 \pm 6	28 \pm 8	100 \pm 71	24.8	g:SiII+FeII1260.5	g:CI1260.7

Table 9—Continued

Wavelength (Å)	Velocity (km s ⁻¹)	b (km s ⁻¹)	\mathcal{W} (mÅ)	SL (σ)	Id	Alt Id
Fairall 9						
1238.818 \pm 0.026	-1 \pm 6	32 \pm 6	48 \pm 11	9.7	g:NV1238.8	...
1239.855 \pm 0.029	-17 \pm 7	17 \pm 10	21 \pm 9	3.9	g:MgII1239.9	h:NV1238.8
1240.402 \pm 0.036	2 \pm 9	19 \pm 13	15 \pm 8	3.0	g:MgII1240.4	...
1240.988 \pm 0.038	6244 \pm 9	35 \pm 13	22 \pm 9	5.3	Ly α	h:MgII1239.9
1244.462 \pm 0.034	7100 \pm 8	39 \pm 11	32 \pm 10	8.2	Ly α	...
1250.569 \pm 0.023	-4 \pm 5	20 \pm 4	80 \pm 6	22.4	g:SiII1250.6	...
1251.367 \pm 0.025	188 \pm 6	32 \pm 5	41 \pm 7	11.3	h:SiII1250.6	Ly α
1253.787 \pm 0.023	-6 \pm 5	21 \pm 4	106 \pm 7	32.2	g:SiII1253.8	...
1254.139 \pm 0.024	9487 \pm 6	43 \pm 6	84 \pm 13	26.5	Ly α	...
1254.572 \pm 0.023	182 \pm 5	27 \pm 4	56 \pm 7	17.6	h:SiII1253.8	...
1259.483 \pm 0.023	-9 \pm 5	24 \pm 3	130 \pm 7	36.7	g:SiII1259.5	...
1260.338 \pm 0.029	199 \pm 7	15 \pm 5	34 \pm 9	8.9	h:SiII1259.5	g:SiII+FeII1260.5
1260.468 \pm 0.029	2 \pm 7	61 \pm 3	406 \pm 19	106.6	g:SiII+FeII1260.5	h:SiII1259.5
1261.039 \pm 0.035	128 \pm 8	54 \pm 6	379 \pm 75	105.2	h:SiII+FeII1260.5	g:CI1260.7?
1261.300 \pm 0.028	190 \pm 7	36 \pm 4	180 \pm 62	51.3	h:SiII+FeII1260.5	...
1262.864 \pm 0.029	11638 \pm 7	28 \pm 13	16 \pm 8	5.2	Ly α	...
1263.998 \pm 0.041	11918 \pm 10	42 \pm 15	22 \pm 9	7.0	Ly α	...
1264.684 \pm 0.073	12087 \pm 18	44 \pm 33	30 \pm 28	10.2	Ly α	...
1265.104 \pm 0.026	12191 \pm 6	23 \pm 7	28 \pm 7	9.5	Ly α	...
1265.407 \pm 0.029	12265 \pm 7	19 \pm 18	11 \pm 8	3.8	Ly α	...
1265.970 \pm 0.117	12404 \pm 29	32 \pm 23	19 \pm 23	7.0	Ly α	...
1268.850 \pm 0.029	-688 \pm 7	81 \pm 22	32 \pm 12	11.2	i:Ly α	...
1269.351 \pm 0.029	-570 \pm 7	46 \pm 19	16 \pm 9	5.4	i:Ly α	...
1269.731 \pm 0.029	-480 \pm 7	99 \pm 3	74 \pm 7	26.7	i:Ly α	...
1270.288 \pm 0.032	-349 \pm 8	89 \pm 12	93 \pm 16	32.2	i:Ly α	...
1270.746 \pm 0.027	-241 \pm 6	11 \pm 11	11 \pm 6	4.2	i:Ly α	...
1270.955 \pm 0.029	-191 \pm 7	42 \pm 5	55 \pm 9	20.3	i:Ly α	...

H 1821+643

Table 9—Continued

Wavelength (Å)	Velocity (km s ⁻¹)	b (km s ⁻¹)	\mathcal{W} (mÅ)	SL (σ)	Id	Alt Id
1238.014 \pm 0.036	5510 \pm 9	21 \pm 14	23 \pm 13	3.3	Ly α	...
1238.608 \pm 0.029	-47 \pm 7	38 \pm 22	42 \pm 27	5.9	h:NV1238.8	...
1238.826 \pm 0.029	1 \pm 7	28 \pm 8	93 \pm 29	13.1	g:NV1238.8	Ly α
1238.938 \pm 0.029	28 \pm 7	10 \pm 10	34 \pm 15	4.7	g:NV1238.8	h:MgII1239.9?
1239.938 \pm 0.029	3 \pm 7	34 \pm 9	59 \pm 18	8.5	g:MgII1239.9	h:MgII1240.4
1240.569 \pm 0.036	6140 \pm 9	14 \pm 16	24 \pm 16	3.4	Ly α	g:MgII1240.4
1242.616 \pm 0.029	-44 \pm 7	42 \pm 20	56 \pm 30	8.2	h:NV1242.8	g:NV1242.8
1242.880 \pm 0.025	18 \pm 6	23 \pm 5	65 \pm 17	9.5	g:NV1242.8	z:Ly β
1244.611 \pm 0.023	0.21340 \pm 0.00002	46 \pm 4	153 \pm 18	25.4	z:Ly β	...
1244.966 \pm 0.031	7225 \pm 8	15 \pm 12	25 \pm 13	3.5	Ly α	...
1245.440 \pm 0.023	7342 \pm 5	47 \pm 3	298 \pm 20	42.4	Ly α	z:NIII989.8
1246.301 \pm 0.036	7554 \pm 9	41 \pm 14	50 \pm 24	7.1	Ly α	...
1247.362 \pm 0.029	7815 \pm 7	36 \pm 34	27 \pm 29	3.7	Ly α	z:Ly β ?
1247.583 \pm 0.029	7870 \pm 7	19 \pm 9	40 \pm 17	5.4	Ly α	...
1247.937 \pm 0.033	7957 \pm 8	33 \pm 10	68 \pm 38	9.4	Ly α	...
1250.314 \pm 0.029	-65 \pm 7	26 \pm 13	30 \pm 17	4.4	h:SII1250.6	z:OVI1031.9
1250.577 \pm 0.023	-2 \pm 5	39 \pm 3	190 \pm 19	28.0	g:SII1250.6	z:OVI1031.9
1252.177 \pm 0.032	0.21344 \pm 0.00003	34 \pm 11	51 \pm 17	9.3	z:OVI1031.9	...
1252.477 \pm 0.042	9077 \pm 10	21 \pm 15	23 \pm 15	3.6	Ly α	...
1253.314 \pm 0.029	-119 \pm 7	17 \pm 10	31 \pm 13	5.0	h:SII1253.8	g:SII1253.8?
1253.792 \pm 0.023	-4 \pm 5	47 \pm 3	263 \pm 22	41.6	g:SII1253.8	z:NIII989.8
1254.874 \pm 0.099	9668 \pm 24	24 \pm 31	21 \pm 25	3.6	Ly α	z:OVI1031.9?
1256.309 \pm 0.029	0.22480 \pm 0.00003	47 \pm 3	199 \pm 19	38.4	z:Ly β	...
1256.635 \pm 0.023	0.22512 \pm 0.00002	57 \pm 3	310 \pm 21	58.9	z:Ly β	...
1257.659 \pm 0.029	0.22612 \pm 0.00002	31 \pm 22	19 \pm 14	3.8	z:Ly β	...
1259.157 \pm 0.029	-86 \pm 7	59 \pm 10	99 \pm 24	16.2	h:SII1259.5	g:SII1259.5?
1259.532 \pm 0.029	3 \pm 7	46 \pm 3	275 \pm 24	45.6	g:SII1259.5	...
1260.052 \pm 0.029	-107 \pm 7	59 \pm 4	440 \pm 35	74.4	h:SiII+FeII1260.5	...
1260.298 \pm 0.036	-48 \pm 9	23 \pm 22	39 \pm 47	6.6	g:SiII+FeII1260.5	...
1260.514 \pm 0.047	3 \pm 6	57 \pm 9	407 \pm 102	70.0	g:SiII+FeII1260.5	g:CI1260.7?
1261.262 \pm 0.029	0.29688 \pm 0.00003	67 \pm 4	252 \pm 19	57.8	z:Ly γ	...

Table 9—Continued

Wavelength (Å)	Velocity (km s ⁻¹)	b (km s ⁻¹)	\mathcal{W} (mÅ)	SL (σ)	Id	Alt Id
1264.194 \pm 0.029	0.22511 \pm 0.00003	39 \pm 5	113 \pm 20	24.8	z:OVI1031.9	...
1264.413 \pm 0.037	0.22533 \pm 0.00003	43 \pm 11	77 \pm 24	16.7	z:OVI1031.9	...
1265.394 \pm 0.029	0.22624 \pm 0.00002	18 \pm 18	16 \pm 12	3.5	z:OVI1031.9	Ly α
1265.683 \pm 0.025	12334 \pm 6	28 \pm 6	64 \pm 15	11.8	Ly α	...
1267.061 \pm 0.023	0.29689 \pm 0.00002	58 \pm 3	259 \pm 13	59.2	z:CIII977.0	...
I ZW 1						
1250.545 \pm 0.037	-9 \pm 9	40 \pm 11	91 \pm 30	6.8	g:SII1250.6	...
1253.808 \pm 0.028	-1 \pm 7	34 \pm 7	115 \pm 26	9.1	g:SII1253.8	...
Markarian 279						
1236.942 \pm 0.030	5246 \pm 7	27 \pm 9	30 \pm 10	5.6	Ly α	...
1237.915 \pm 0.029	5486 \pm 7	30 \pm 29	17 \pm 18	3.5	Ly α	...
1238.260 \pm 0.037	-136 \pm 9	20 \pm 18	22 \pm 16	4.3	h:NV1238.8	Ly α
1238.502 \pm 0.047	5631 \pm 12	21 \pm 23	18 \pm 18	3.7	Ly α	g:NV1238.8?
1238.811 \pm 0.035	-2 \pm 8	39 \pm 16	50 \pm 24	10.3	g:NV1238.8	...
1241.509 \pm 0.029	6372 \pm 7	18 \pm 4	58 \pm 7	14.2	Ly α	...
1241.805 \pm 0.023	6445 \pm 6	21 \pm 4	40 \pm 7	10.4	Ly α	...
1243.753 \pm 0.023	6925 \pm 5	26 \pm 3	65 \pm 8	16.8	Ly α	i:SiIII1206.5?
1247.216 \pm 0.024	7779 \pm 6	28 \pm 5	48 \pm 9	15.1	Ly α	...
1247.533 \pm 0.042	7858 \pm 10	34 \pm 14	21 \pm 10	6.7	Ly α	...
1248.410 \pm 0.029	-1070 \pm 7	18 \pm 12	11 \pm 6	3.6	i:Ly α	...
1249.023 \pm 0.036	-923 \pm 9	43 \pm 12	22 \pm 8	7.5	i:Ly α	...
1249.933 \pm 0.034	-160 \pm 8	23 \pm 14	12 \pm 8	4.0	h:SII1250.6	...
1250.576 \pm 0.029	-2 \pm 7	62 \pm 3	282 \pm 17	99.5	g:SII1250.6	...
1251.056 \pm 0.025	-436 \pm 6	99 \pm 3	646 \pm 18	240.5	i:Ly α	...
1251.261 \pm 0.029	-387 \pm 7	19 \pm 10	17 \pm 10	6.6	i:Ly α	...
1251.694 \pm 0.023	-284 \pm 5	71 \pm 3	322 \pm 14	123.9	i:Ly α	...
1253.051 \pm 0.023	41 \pm 6	25 \pm 5	115 \pm 65	45.3	i:Ly α	...
1253.284 \pm 0.031	97 \pm 7	51 \pm 12	375 \pm 117	146.8	i:Ly α	h:SII1253.8

Table 9—Continued

Wavelength (Å)	Velocity (km s ⁻¹)	b (km s ⁻¹)	\mathcal{W} (mÅ)	SL (σ)	Id	Alt Id
1253.669 \pm 0.045	-34 \pm 11	32 \pm 16	107 \pm 83	39.8	g:SiII1253.8	...
1253.861 \pm 0.040	235 \pm 10	26 \pm 6	94 \pm 53	35.4	i:Ly α	...
Markarian 290						
1232.797 \pm 0.064	4224 \pm 16	21 \pm 29	41 \pm 49	3.6	Ly α	...
1234.597 \pm 0.027	4667 \pm 7	26 \pm 8	60 \pm 18	7.2	Ly α	i:NI1199.5?
1235.764 \pm 0.044	4955 \pm 11	26 \pm 18	28 \pm 19	3.4	Ly α	...
1238.346 \pm 0.035	-110 \pm 8	18 \pm 14	23 \pm 13	3.0	h:NV1238.8	g:NV1238.8?
1240.335 \pm 0.035	-14 \pm 8	22 \pm 12	26 \pm 13	3.6	g:MgII1240.4	...
1242.289 \pm 0.028	25 \pm 7	10 \pm 13	22 \pm 10	3.5	i:SiIII1206.5	h:NV1242.8
1244.408 \pm 0.032	7087 \pm 8	23 \pm 11	23 \pm 10	4.3	Ly α	...
1245.536 \pm 0.025	7365 \pm 6	11 \pm 9	21 \pm 7	4.2	Ly α	...
1245.869 \pm 0.026	7447 \pm 6	8 \pm 12	18 \pm 7	3.6	Ly α	...
1248.079 \pm 0.028	-850 \pm 7	20 \pm 9	22 \pm 9	4.9	i:Ly α	...
1249.349 \pm 0.029	-545 \pm 7	50 \pm 26	25 \pm 23	6.4	i:Ly α	...
1249.579 \pm 0.029	-490 \pm 7	97 \pm 12	225 \pm 48	60.4	i:Ly α	...
1250.019 \pm 0.029	-139 \pm 7	31 \pm 22	19 \pm 23	5.6	h:SiII1250.6	i:Ly α
1250.549 \pm 0.031	-8 \pm 7	94 \pm 6	558 \pm 65	186.2	g:SiII1250.6	...
1251.115 \pm 0.039	-122 \pm 9	99 \pm 3	475 \pm 37	185.6	i:Ly α	...
1251.664 \pm 0.025	9 \pm 6	50 \pm 4	105 \pm 17	45.2	i:Ly α	...
1252.109 \pm 0.029	116 \pm 7	61 \pm 12	71 \pm 17	31.3	i:Ly α	...
1252.479 \pm 0.029	204 \pm 7	35 \pm 6	33 \pm 10	14.5	i:Ly α	...
1253.327 \pm 0.029	-113 \pm 7	28 \pm 5	34 \pm 6	13.7	h:SiII1253.8	...
1253.804 \pm 0.023	-2 \pm 5	36 \pm 3	181 \pm 10	67.8	g:SiII1253.8	...
1254.353 \pm 0.029	653 \pm 7	81 \pm 29	50 \pm 24	17.3	i:Ly α	...
1254.653 \pm 0.029	725 \pm 7	35 \pm 14	24 \pm 12	7.8	i:Ly α	...
1254.953 \pm 0.029	797 \pm 7	23 \pm 13	16 \pm 10	4.8	i:Ly α	...
1259.058 \pm 0.029	-110 \pm 7	39 \pm 7	72 \pm 16	15.2	h:SiII1259.5	...
1259.328 \pm 0.029	-46 \pm 7	17 \pm 6	40 \pm 13	8.4	g:SiII1259.5	i:Ly α
1259.535 \pm 0.023	4 \pm 5	24 \pm 3	153 \pm 14	31.7	g:SiII1259.5	...
1260.008 \pm 0.029	-117 \pm 7	63 \pm 3	479 \pm 28	97.3	h:SiII+FeII1260.5	g:SiII+FeII1260.5?

Table 9—Continued

Wavelength (Å)	Velocity (km s ⁻¹)	b (km s ⁻¹)	\mathcal{W} (mÅ)	SL (σ)	Id	Alt Id
1260.464 \pm 0.027	-9 \pm 6	55 \pm 4	399 \pm 45	79.5	g:SiII+FeII1260.5	...
Markarian 335						
1223.637 \pm 0.026	1965 \pm 6	75 \pm 7	229 \pm 30	28.1	Ly α	...
1224.974 \pm 0.049	2295 \pm 12	73 \pm 17	81 \pm 26	10.2	Ly α	...
1232.979 \pm 0.057	4268 \pm 14	51 \pm 20	33 \pm 16	5.1	Ly α	...
1241.093 \pm 0.026	6269 \pm 6	75 \pm 6	130 \pm 14	30.3	Ly α	...
1250.584 \pm 0.023	0 \pm 6	58 \pm 4	126 \pm 13	35.6	g:SiII1250.6	...
1253.786 \pm 0.023	-6 \pm 6	67 \pm 4	197 \pm 15	41.3	g:SiII1253.8	...
Markarian 421						
1227.977 \pm 0.025	3035 \pm 6	35 \pm 5	86 \pm 15	12.4	Ly α	...
1238.626 \pm 0.034	-47 \pm 8	19 \pm 13	20 \pm 11	3.2	g:NV1238.8	h:NV1238.8
1250.385 \pm 0.031	-52 \pm 7	11 \pm 16	28 \pm 31	4.5	h:SiII1250.6	...
1250.564 \pm 0.052	-5 \pm 12	35 \pm 14	83 \pm 40	13.2	g:SiII1250.6	...
1253.578 \pm 0.031	-53 \pm 8	11 \pm 13	33 \pm 29	4.8	h:SiII1253.8	...
1253.764 \pm 0.031	-11 \pm 7	33 \pm 7	155 \pm 38	22.7	g:SiII1253.8	...
1256.928 \pm 0.051	1140 \pm 12	17 \pm 15	23 \pm 27	3.7	i:Ly α	...
1257.127 \pm 0.029	1188 \pm 7	30 \pm 35	22 \pm 27	3.7	i:Ly α	...
Markarian 501						
1234.572 \pm 0.039	4661 \pm 10	60 \pm 13	161 \pm 43	11.1	Ly α	Absorber ‘A’
1238.757 \pm 0.062	-16 \pm 15	31 \pm 25	47 \pm 41	3.4	g:NV1238.8	Ly α
1239.968 \pm 0.029	5992 \pm 7	59 \pm 39	55 \pm 46	4.2	Ly α	Absorber ‘B’
1242.610 \pm 0.243	-47 \pm 59	74 \pm 70	46 \pm 55	3.1	g:NV1242.8	Ly α
1246.177 \pm 0.069	7523 \pm 17	48 \pm 26	53 \pm 36	4.0	Ly α	Absorber ‘C’
1250.592 \pm 0.063	2 \pm 15	42 \pm 22	99 \pm 64	7.1	g:SiII1250.6	...
1251.152 \pm 0.029	8750 \pm 7	77 \pm 49	66 \pm 57	4.9	Ly α	h:SiII1250.6
1253.069 \pm 0.264	-175 \pm 63	99 \pm 3	64 \pm 33	4.7	h:SiII1253.8	i:Ly α

Table 9—Continued

Wavelength (Å)	Velocity (km s ⁻¹)	<i>b</i> (km s ⁻¹)	\mathcal{W} (mÅ)	SL (σ)	Id	Alt Id
1253.803 \pm 0.051	-2 \pm 12	85 \pm 16	235 \pm 61	17.5	g:SiII1253.8	...
1254.773 \pm 0.029	-434 \pm 7	99 \pm 3	70 \pm 28	5.4	i:Ly α	h:SiII1253.8
Markarian 509						
1226.050 \pm 0.025	2560 \pm 6	40 \pm 5	209 \pm 32	14.4	Ly α	...
1238.669 \pm 0.029	-32 \pm 7	16 \pm 29	14 \pm 17	3.0	h:NV1238.8	g:NV1238.8
1238.924 \pm 0.029	25 \pm 7	56 \pm 48	100 \pm 111	21.1	g:NV1238.8	h:MgII1239.9
1239.182 \pm 0.029	-180 \pm 7	21 \pm 18	24 \pm 29	5.1	h:MgII1239.9	...
1239.951 \pm 0.029	6 \pm 7	18 \pm 9	24 \pm 9	5.1	g:MgII1239.9	h:MgII1240.4
1242.874 \pm 1.206	17 \pm 291	45 \pm 46	29 \pm 35	7.2	g:NV1242.8	h:NV1242.8
1243.060 \pm 0.734	62 \pm 177	35 \pm 38	17 \pm 21	4.3	h:NV1242.8	g:NV1242.8?
1250.314 \pm 0.029	-69 \pm 7	24 \pm 9	20 \pm 7	7.2	h:SiII1250.6	...
1250.583 \pm 0.023	0 \pm 5	23 \pm 3	86 \pm 7	31.1	g:SiII1250.6	...
1250.819 \pm 0.029	56 \pm 7	42 \pm 5	58 \pm 8	21.3	h:SiII1250.6	g:SiII1250.6?
1253.561 \pm 0.029	-57 \pm 7	41 \pm 9	27 \pm 7	11.7	h:SiII1253.8	g:SiII1253.8?
1253.832 \pm 0.023	5 \pm 5	28 \pm 3	115 \pm 17	50.5	g:SiII1253.8	h:SiII1253.8?
1254.079 \pm 0.032	64 \pm 8	40 \pm 6	85 \pm 19	37.5	h:SiII1253.8	g:SiII1253.8?
1255.795 \pm 0.029	-403 \pm 7	46 \pm 5	132 \pm 67	64.4	i:Ly α	...
1256.065 \pm 0.029	-339 \pm 7	44 \pm 14	76 \pm 92	37.9	i:Ly α	...
1256.285 \pm 0.029	-286 \pm 7	93 \pm 31	505 \pm 425	147.7	i:Ly α	...
1256.535 \pm 0.029	-227 \pm 7	63 \pm 60	47 \pm 56	3.3	i:Ly α	...
1257.165 \pm 0.029	-76 \pm 7	69 \pm 21	191 \pm 229	61.9	i:Ly α	...
1257.365 \pm 0.029	-29 \pm 7	65 \pm 62	265 \pm 318	121.5	i:Ly α	...
1257.605 \pm 0.029	29 \pm 7	44 \pm 16	140 \pm 168	73.7	i:Ly α	...
1257.785 \pm 0.029	71 \pm 7	28 \pm 17	26 \pm 32	13.9	i:Ly α	...
1257.985 \pm 0.029	119 \pm 7	72 \pm 25	449 \pm 240	238.6	i:Ly α	...
1258.365 \pm 0.029	-270 \pm 7	53 \pm 13	237 \pm 151	122.7	h:SiII1259.5	i:Ly α
1258.565 \pm 0.029	-222 \pm 7	33 \pm 8	43 \pm 46	22.6	h:SiII1259.5	i:Ly α
1259.550 \pm 0.026	7 \pm 6	60 \pm 4	201 \pm 21	107.8	g:SiII1259.5	...
1259.858 \pm 0.029	85 \pm 7	34 \pm 19	30 \pm 37	16.1	h:SiII1259.5	h:CI1260.7
1260.257 \pm 0.029	-48 \pm 7	68 \pm 64	43 \pm 52	22.2	h:SiII+FeII1260.5	g:CI1260.7?

Table 9—Continued

Wavelength (Å)	Velocity (km s ⁻¹)	b (km s ⁻¹)	\mathcal{W} (mÅ)	SL (σ)	Id	Alt Id
1260.347 \pm 6.901	-36 \pm 37	71 \pm 68	332 \pm 398	170.8	g:SiII+FeII1260.5	...
1260.710 \pm 0.029	50 \pm 7	72 \pm 4	372 \pm 73	186.9	h:SiII+FeII1260.5	g:CI1260.7
Markarian 817						
1223.507 \pm 0.037	1933 \pm 9	34 \pm 13	29 \pm 13	5.3	Ly α	...
1224.172 \pm 0.023	2097 \pm 5	40 \pm 4	135 \pm 15	25.3	Ly α	...
1234.657 \pm 0.041	4682 \pm 10	40 \pm 15	23 \pm 11	5.6	Ly α	...
1236.303 \pm 0.023	5088 \pm 6	84 \pm 4	207 \pm 14	56.3	Ly α	...
1236.902 \pm 0.027	5236 \pm 7	24 \pm 7	25 \pm 7	6.6	Ly α	...
1238.529 \pm 0.029	-65 \pm 7	75 \pm 28	54 \pm 41	13.5	h:NV1238.8	g:NV1238.8?
1238.809 \pm 0.029	2 \pm 5	40 \pm 26	21 \pm 23	5.2	g:NV1238.8	h:NV1238.8
1239.159 \pm 0.029	5793 \pm 7	39 \pm 12	34 \pm 13	8.7	Ly α	...
1239.509 \pm 0.029	-101 \pm 7	46 \pm 18	25 \pm 12	6.3	h:MgII1239.9	g:MgII1239.9?
1241.034 \pm 0.024	6255 \pm 6	29 \pm 5	37 \pm 8	11.6	Ly α	...
1242.740 \pm 0.029	-15 \pm 7	25 \pm 32	10 \pm 12	3.2	g:NV1242.8	h:NV1242.8
1245.395 \pm 0.051	7330 \pm 13	51 \pm 18	17 \pm 7	5.9	Ly α	...
1247.294 \pm 0.044	7799 \pm 11	56 \pm 16	28 \pm 9	10.1	Ly α	...
1249.477 \pm 0.041	-1023 \pm 10	26 \pm 9	36 \pm 17	13.8	i:Ly α	...
1249.694 \pm 0.077	-971 \pm 18	28 \pm 21	20 \pm 19	7.7	i:Ly α	...
1250.071 \pm 0.034	-127 \pm 8	24 \pm 13	13 \pm 6	5.1	h:SII1250.6	...
1250.415 \pm 0.029	-44 \pm 7	30 \pm 11	26 \pm 9	9.8	h:SII1250.6	...
1250.568 \pm 0.023	-4 \pm 5	16 \pm 4	47 \pm 6	18.0	g:SII1250.6	...
1251.752 \pm 0.025	-479 \pm 6	18 \pm 7	14 \pm 4	6.0	i:Ly α	...
1253.355 \pm 0.027	-106 \pm 6	27 \pm 12	32 \pm 13	12.9	h:SII1253.8	...
1253.653 \pm 0.029	-35 \pm 7	27 \pm 8	53 \pm 16	21.7	h:SII1253.8	...
1253.810 \pm 0.023	0 \pm 5	19 \pm 4	76 \pm 8	31.3	g:SII1253.8	...
PKS 2155-304: PRE-COSTAR						
1226.345 \pm 0.060	2632 \pm 15	61 \pm 33	42 \pm 40	9.2	Ly α	...
1226.964 \pm 0.065	2785 \pm 16	64 \pm 26	36 \pm 22	7.9	Ly α	z:SiIII1206.5

Table 9—Continued

Wavelength (Å)	Velocity (km s ⁻¹)	b (km s ⁻¹)	\mathcal{W} (mÅ)	SL (σ)	Id	Alt Id
1232.016 \pm 0.049	4031 \pm 12	39 \pm 17	21 \pm 11	4.2	Ly α	...
1234.767 \pm 0.051	4709 \pm 12	32 \pm 24	15 \pm 14	3.3	Ly α	...
1235.748 \pm 0.029	4951 \pm 7	68 \pm 15	64 \pm 23	14.3	Ly α	...
1235.998 \pm 0.029	5013 \pm 7	58 \pm 11	82 \pm 22	18.1	Ly α	...
1236.426 \pm 0.029	5119 \pm 7	80 \pm 5	218 \pm 20	48.1	Ly α	...
1238.451 \pm 0.029	5618 \pm 7	33 \pm 14	29 \pm 15	6.7	Ly α	...
1238.673 \pm 0.031	5673 \pm 8	30 \pm 12	39 \pm 16	9.1	Ly α	...
1238.869 \pm 0.029	17 \pm 7	31 \pm 11	31 \pm 13	7.2	g:NV1238.8	...
1239.802 \pm 0.045	-30 \pm 11	52 \pm 16	32 \pm 13	7.3	g:MgII1239.9	...
1240.392 \pm 0.055	-1 \pm 13	41 \pm 21	18 \pm 12	4.2	g:MgII1240.4	Ly α
1242.849 \pm 0.029	11 \pm 7	47 \pm 30	20 \pm 16	4.0	g:NV1242.8	Ly α
1246.990 \pm 0.029	7724 \pm 7	31 \pm 35	13 \pm 16	3.0	Ly α	...
1247.510 \pm 0.029	7852 \pm 7	30 \pm 31	13 \pm 16	3.1	Ly α	...
1250.572 \pm 0.026	-3 \pm 6	51 \pm 6	80 \pm 11	18.4	g:SII1250.6	...
1253.790 \pm 0.023	-5 \pm 6	53 \pm 4	126 \pm 13	27.9	g:SII1253.8	...
1255.084 \pm 0.041	9720 \pm 10	24 \pm 16	13 \pm 9	3.0	Ly α	...
1256.636 \pm 0.042	10102 \pm 10	25 \pm 15	14 \pm 8	3.3	Ly α	...
PKS 2155-304: POST-COSTAR						
1259.502 \pm 0.023	-4 \pm 5	21 \pm 4	133 \pm 19	14.9	g:SII1259.5	h:CI1260.7
1259.848 \pm 0.028	-155 \pm 7	31 \pm 9	76 \pm 23	8.5	h:SiII+FeII1260.5	g:SII1259.5?
1260.351 \pm 0.028	-35 \pm 7	22 \pm 12	68 \pm 59	7.7	g:SiII+FeII1260.5	...
1260.513 \pm 0.036	3 \pm 6	61 \pm 6	412 \pm 77	46.2	g:SiII+FeII1260.5	g:CI1260.7?
1264.806 \pm 0.058	12117 \pm 14	39 \pm 20	31 \pm 19	3.6	Ly α	...
1270.784 \pm 0.027	13591 \pm 6	39 \pm 6	101 \pm 18	12.5	Ly α	...
1281.375 \pm 0.024	16203 \pm 5	58 \pm 3	346 \pm 23	44.8	Ly α	...
1281.867 \pm 0.061	16325 \pm 15	49 \pm 22	62 \pm 34	8.2	Ly α	...
1284.301 \pm 0.030	16925 \pm 7	19 \pm 13	43 \pm 37	5.7	Ly α	...
1284.497 \pm 0.039	16973 \pm 9	63 \pm 6	389 \pm 68	50.9	Ly α	...
1285.086 \pm 0.038	17119 \pm 9	87 \pm 11	448 \pm 79	57.9	Ly α	...
1287.497 \pm 0.024	17713 \pm 6	35 \pm 5	139 \pm 21	18.4	Ly α	...

Table 9—Continued

Wavelength (Å)	Velocity (km s ⁻¹)	b (km s ⁻¹)	\mathcal{W} (mÅ)	SL (σ)	Id	Alt Id
1288.958 \pm 0.029	18073 \pm 7	47 \pm 8	99 \pm 20	13.2	Ly α	...
Q 1230+0115						
1221.711 \pm 0.026	1490 \pm 6	21 \pm 8	138 \pm 42	6.3	Ly α	...
1222.425 \pm 0.035	1666 \pm 9	54 \pm 10	385 \pm 94	16.9	Ly α	...
1222.747 \pm 0.029	1745 \pm 7	40 \pm 12	241 \pm 99	10.9	Ly α	...
1223.211 \pm 0.051	1860 \pm 13	48 \pm 21	142 \pm 81	6.6	Ly α	...
1225.000 \pm 0.024	2301 \pm 6	55 \pm 6	439 \pm 57	23.9	Ly α	...
1236.045 \pm 0.041	5025 \pm 10	24 \pm 15	53 \pm 31	3.1	Ly α	...
1242.897 \pm 0.044	6714 \pm 11	19 \pm 19	45 \pm 35	3.2	Ly α	g:NV1242.8
1246.254 \pm 0.049	7542 \pm 12	31 \pm 18	44 \pm 27	3.3	Ly α	z:NV1238.8
1250.570 \pm 0.028	-3 \pm 7	27 \pm 7	94 \pm 25	7.0	g:SII1250.6	...
1253.145 \pm 0.031	9242 \pm 8	72 \pm 8	301 \pm 49	24.8	Ly α	...
1253.783 \pm 0.029	-7 \pm 7	61 \pm 8	327 \pm 69	26.1	g:SII1253.8	...

B. CfA Pie Diagrams and Nearest Neighbor Distances

In this Appendix we present $\pm 7^\circ$ “pie diagrams” of our sightlines, and Table 10 which describes the three nearest known galaxies to each of our Ly α absorbers. In Figures 21–35, the coordinate along the slice of a pie diagram is the heliocentric recession velocity in km s^{-1} . The dashed line in each diagram marks the sightline. Sightlines terminating with dashed arrows indicate that the target lies beyond the extent of the pie diagram (3C 273, H 1821+643, and PKS 2155-304). Objects whose positions are included by the pie diagram are marked with a large circle indicating the AGN target. The smaller circles indicate the positions along the sight line of the Ly α absorbers; the middle-sized circles are the definite ($SL \geq 4\sigma$) detections, and the smallest circles are the possible ($3\sigma \leq SL < 4\sigma$) detections. Each symbol “c” is an individual galaxy in the merged CfA redshift catalog; the orientation of the “c” for each galaxy is conserved between the wedges. The “v” symbols indicate CfA catalog galaxies within 2° of the sight line and are oriented consistently between the α and δ diagrams. Galaxies at $cz < 500 \text{ km s}^{-1}$ have been deleted from these plots.

Table 10 includes the following information by column: (1) the absorber type where D=Definite ($SL \geq 4\sigma$) or P=Possible ($3\sigma \leq SL < 4\sigma$); (2) the heliocentric recession velocity of the absorber (non-relativistic cz) converted from LSR using the standard value for the local standard of rest (see § 5); (3) the nearest galaxy name as given in the CfA catalog (Huchra et al. 1992); (4) the absorber-galaxy distance perpendicular to the line-of-sight (LOS) in h_{70}^{-1} Mpc; (5) the non-relativistic heliocentric recession velocity (cz , in km s^{-1}) of the nearest galaxy as given in the CfA catalog; (6) the absorber-galaxy distance (in h_{70}^{-1} Mpc) along the LOS, assuming a retarded Hubble flow ($\pm 300 \text{ km s}^{-1}$); (7) the Euclidean 3D absorber-galaxy distance (in h_{70}^{-1} Mpc), assuming a retarded Hubble flow ($\pm 300 \text{ km s}^{-1}$; see § 5 and Stocke et al. (1995)); and (8) the galaxy blue magnitude as given in the CfA Catalog.

As discussed in Paper III, the completeness of the CfA catalog varies with position on the sky. Therefore, direct conclusions about galaxy-absorber connections and “void” absorbers should not be derived from Table 10. However, if one adopts the very liberal definition of an “association” as any absorber within $500h_{70}^{-1} \text{ kpc}$ of a CfA galaxy, and a “void” absorber as any galaxy whose nearest neighboring galaxy is $> 6h_{70}^{-1} \text{ Mpc}$ away, our $SL \geq 4\sigma$ sample contains 20 galaxy-absorber “associations” and 21 galaxy “void” Ly α absorbers (using the total absorber-galaxy distances of column 7 in Table 10). Our $3\sigma \leq SL < 4\sigma$ sample contains an additional two absorber-galaxy “associations” and four “void” absorbers.

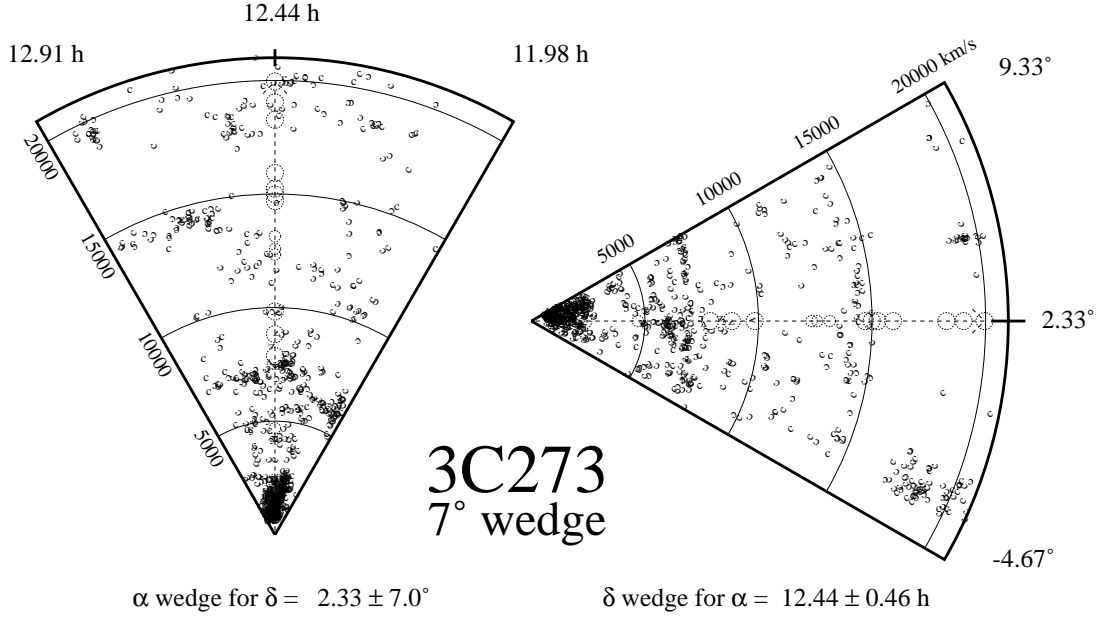


Fig. 21.— Right ascension (α) and declination (δ) pie diagram for the 3C 273 sightline.

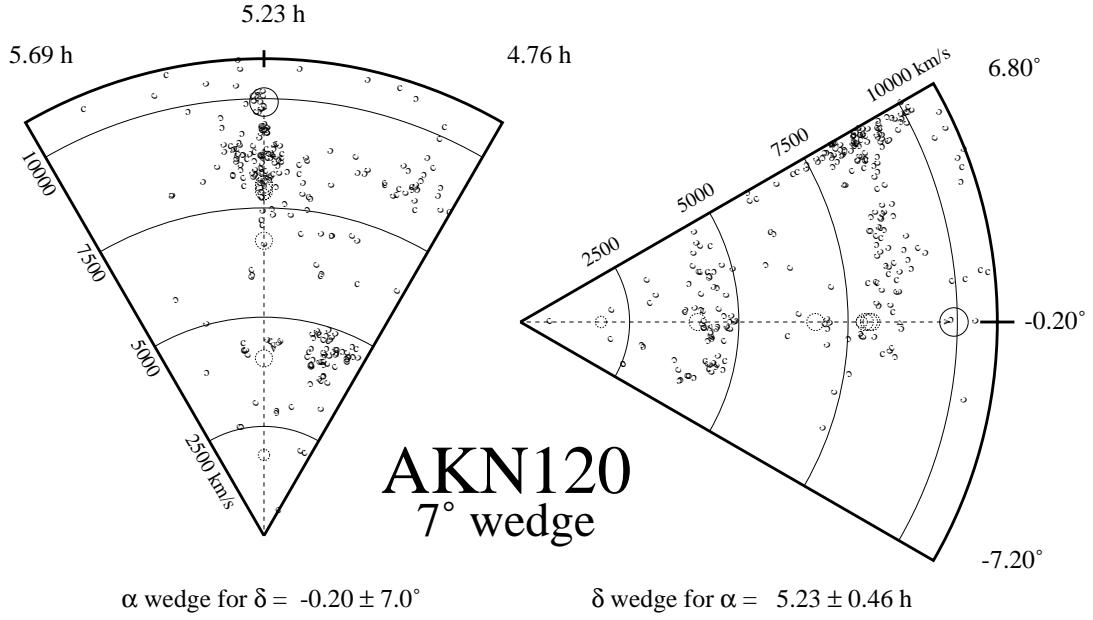


Fig. 22.— Right ascension (α) and declination (δ) pie diagram for the Arakelian 120 sightline.

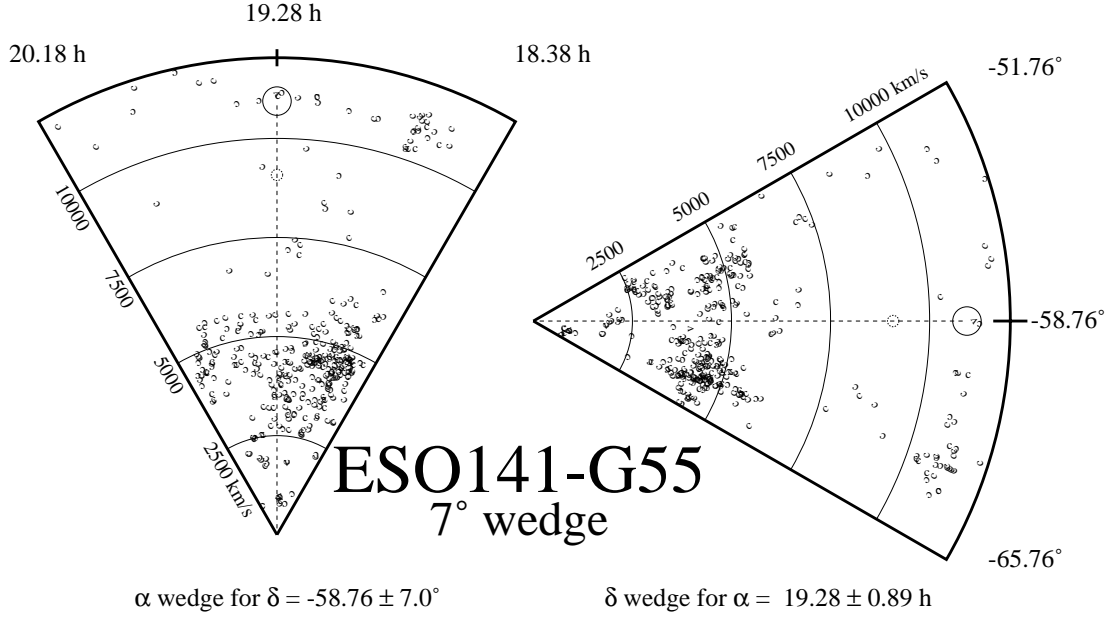


Fig. 23.— Right ascension (α) and declination (δ) pie diagram for the ESO 141-G55 sightline.

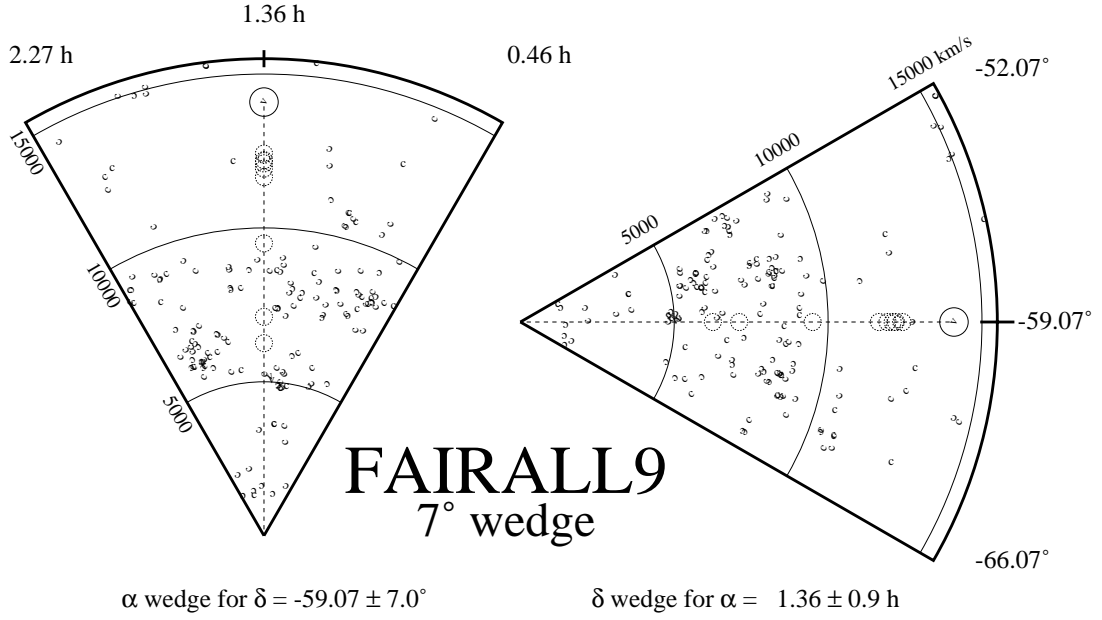


Fig. 24.— Right ascension (α) and declination (δ) pie diagram for the FAIRALL 9 sightline.

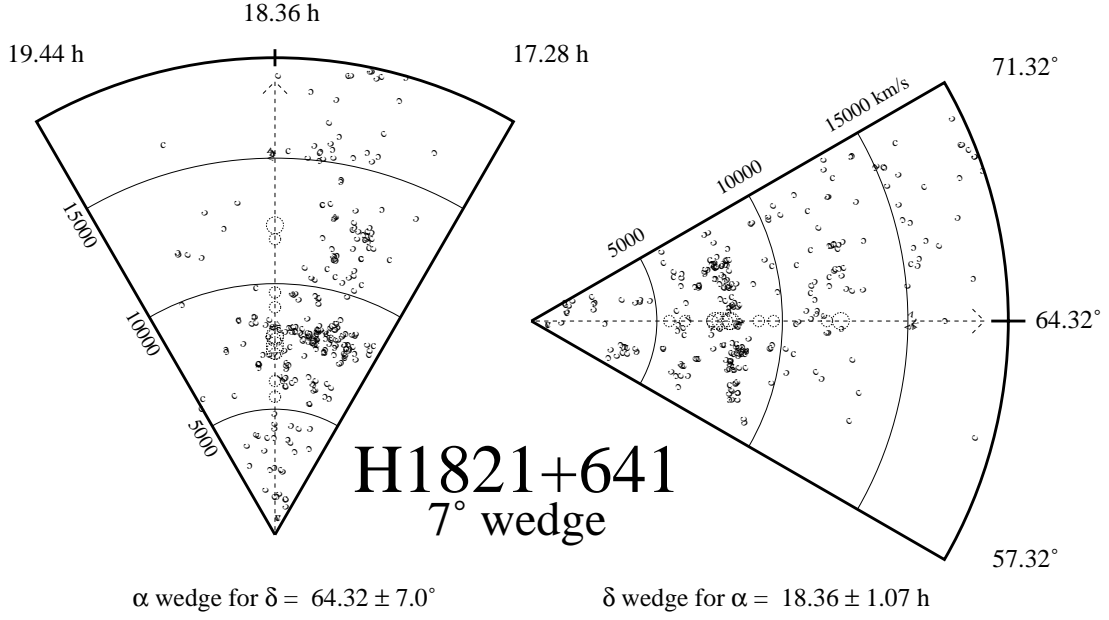


Fig. 25.— Right ascension (α) and declination (δ) pie diagram for the H 1821+643 sightline.

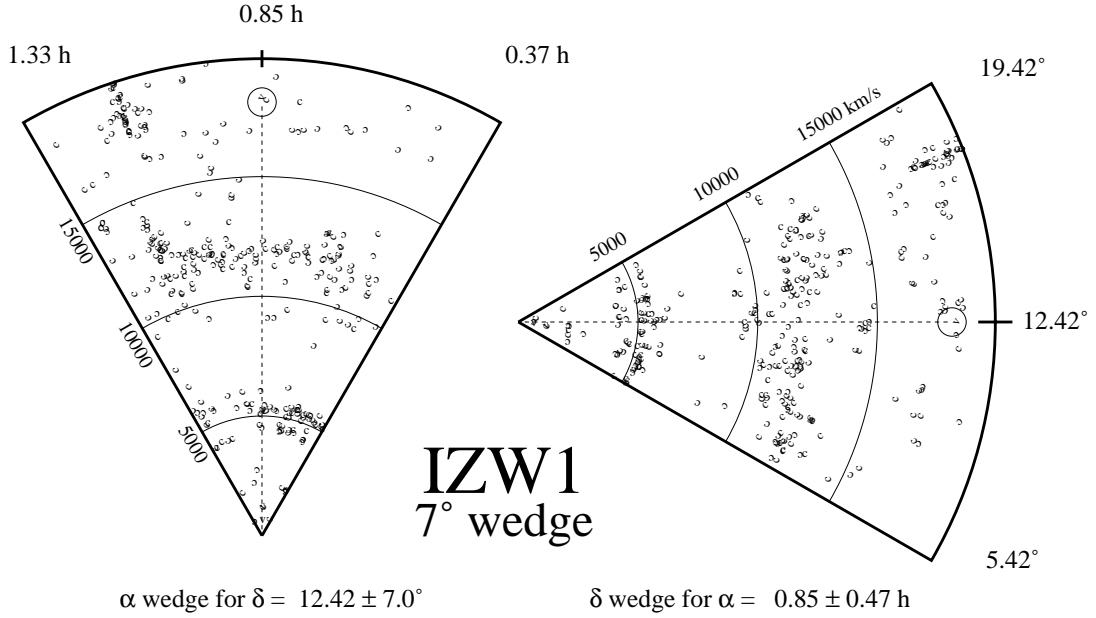


Fig. 26.— Right ascension (α) and declination (δ) pie diagram for the I ZW 1 sightline.

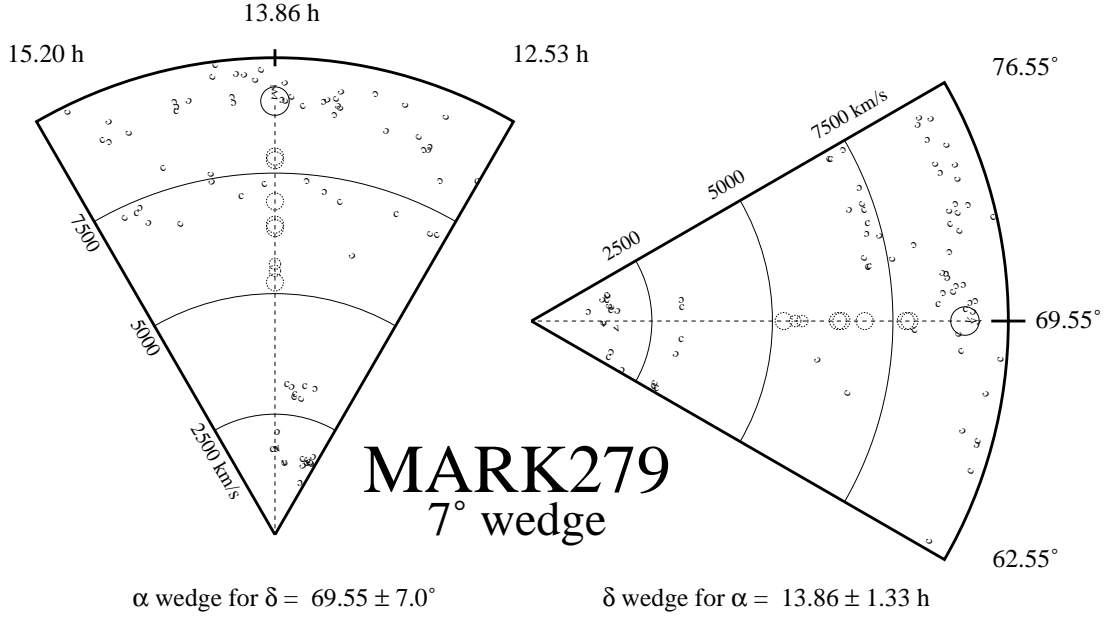


Fig. 27.— Right ascension (α) and declination (δ) pie diagram for the Markarian 279 sightline.

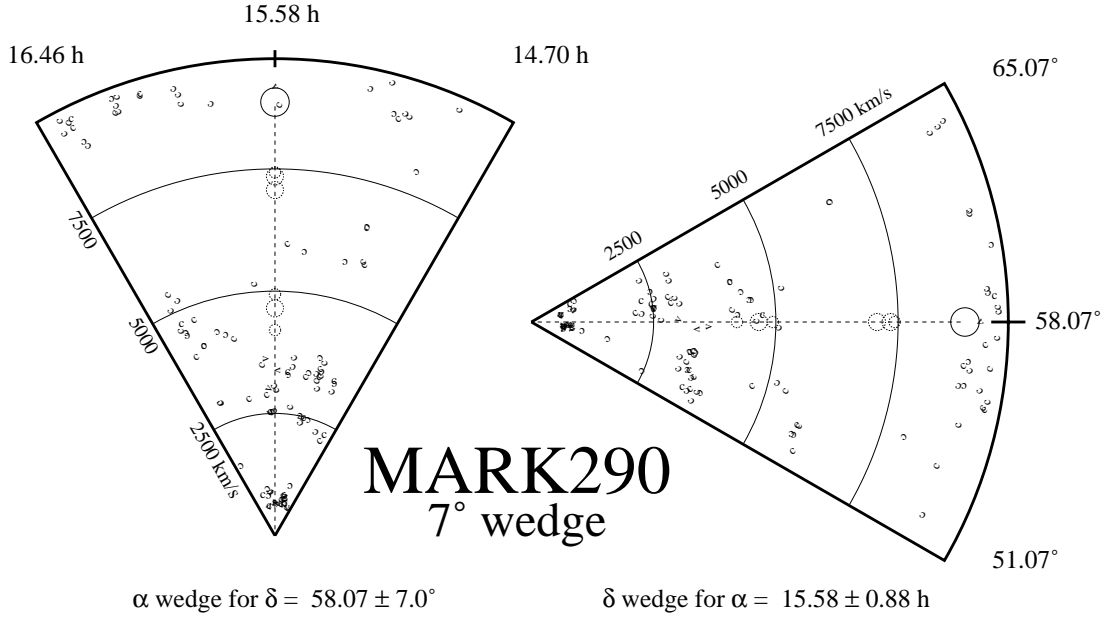


Fig. 28.— Right ascension (α) and declination (δ) pie diagram for the Markarian 290 sightline.

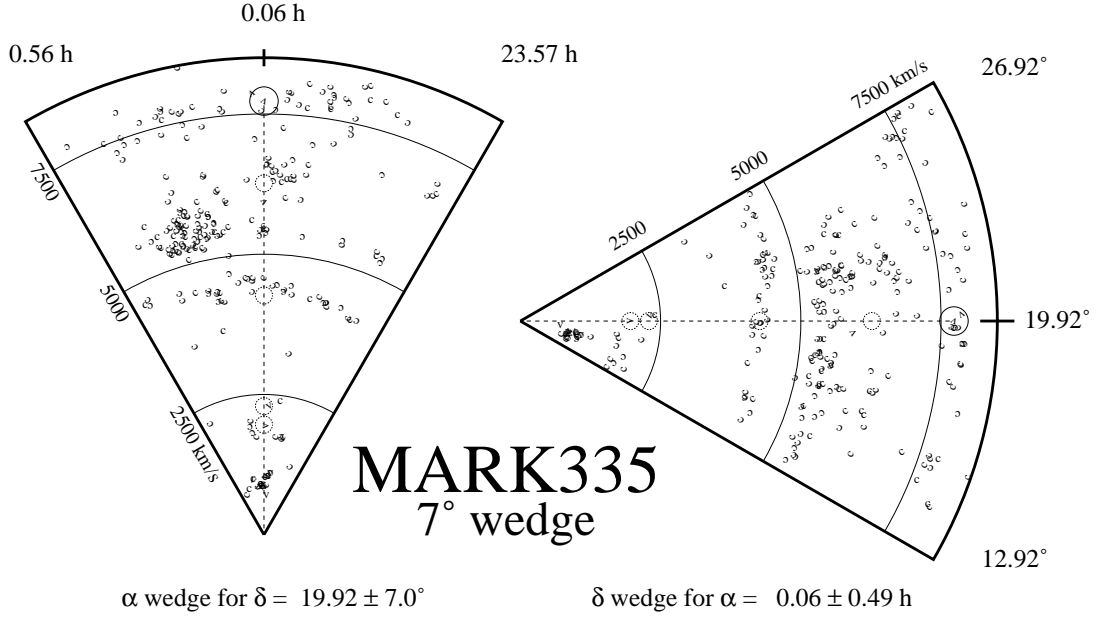


Fig. 29.— Right ascension (α) and declination (δ) pie diagram for the Markarian 335 sightline.

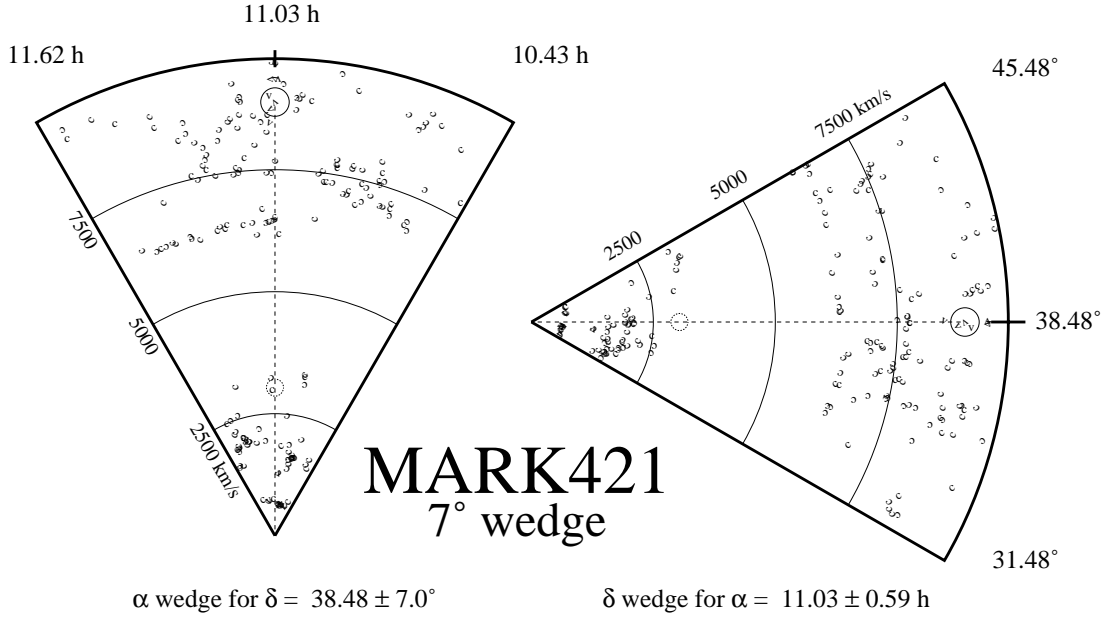


Fig. 30.— Right ascension (α) and declination (δ) pie diagram for the Markarian 421 sightline.

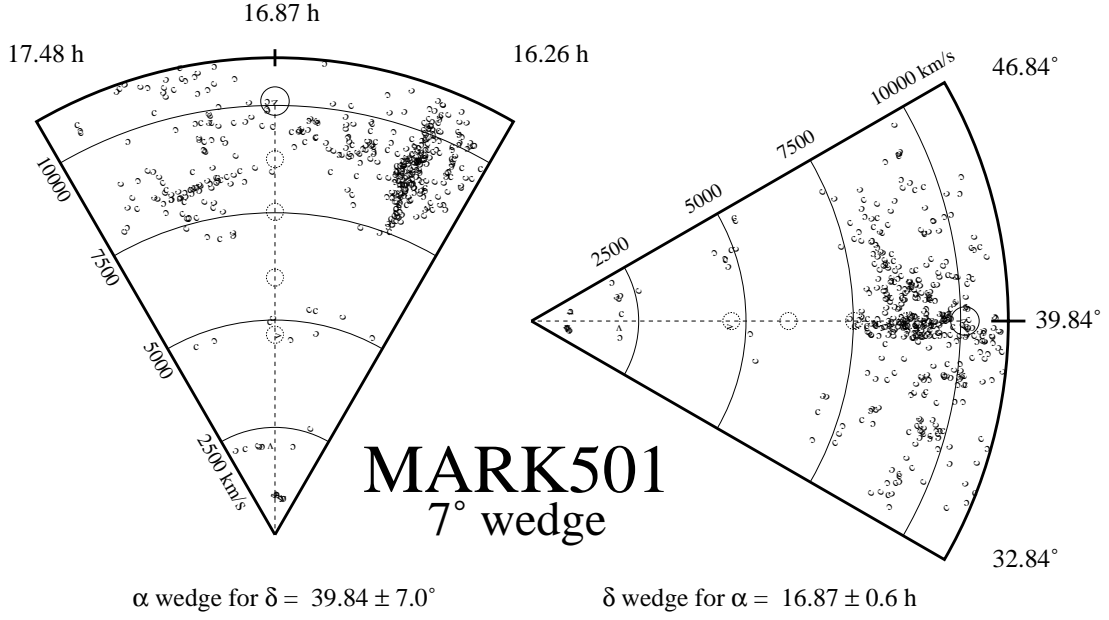


Fig. 31.— Right ascension (α) and declination (δ) pie diagram for the Markarian 501 sightline.

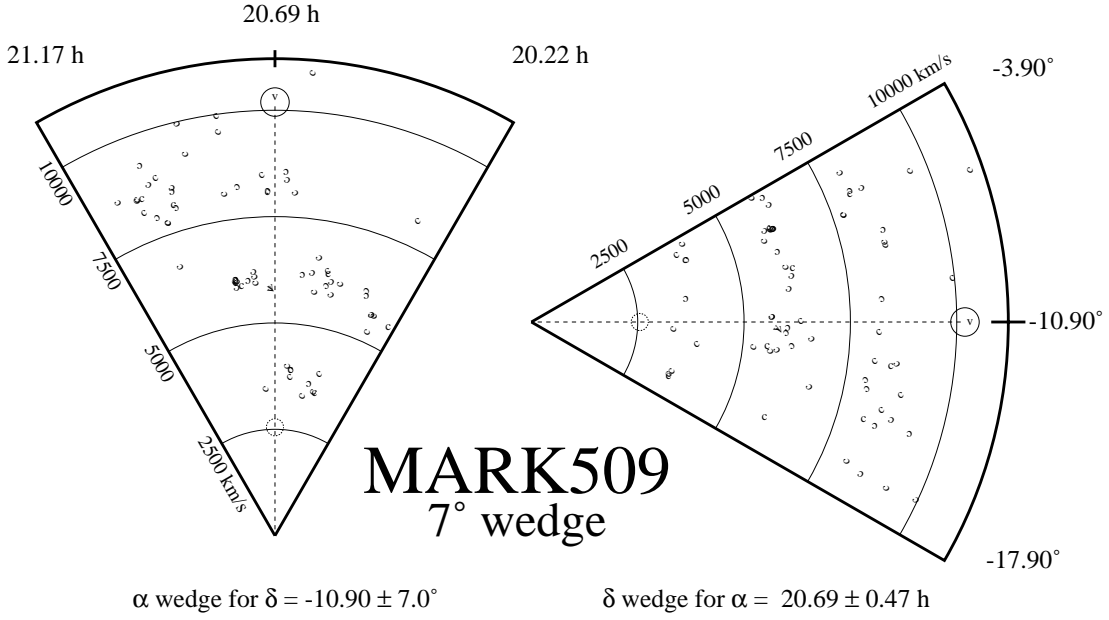


Fig. 32.— Right ascension (α) and declination (δ) pie diagram for the Markarian 509 sightline.

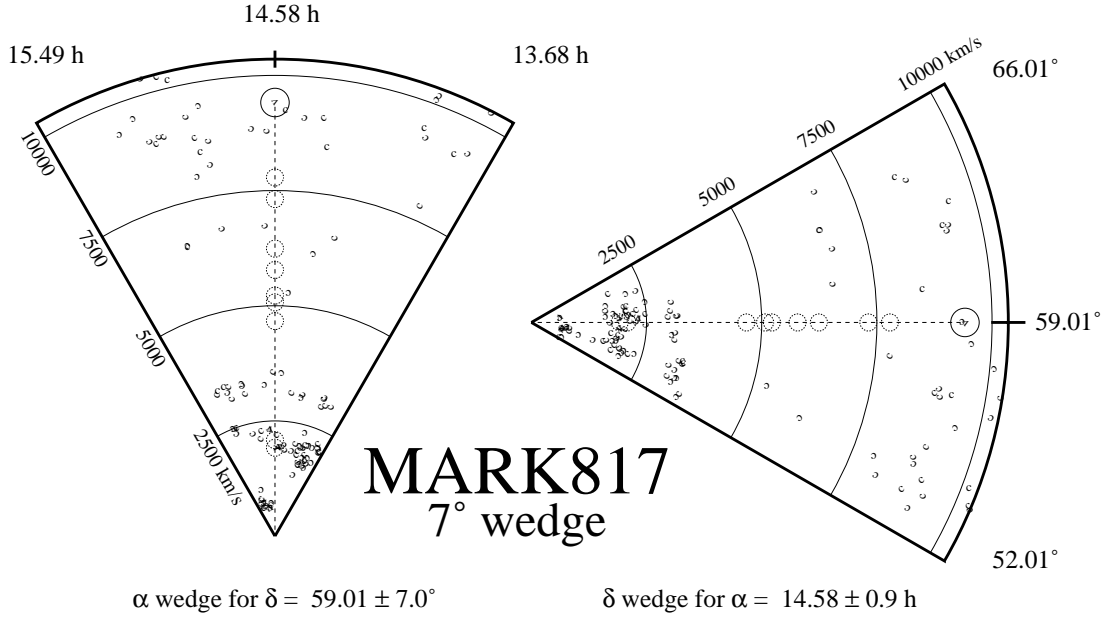


Fig. 33.— Right ascension (α) and declination (δ) pie diagram for the Markarian 817 sightline.

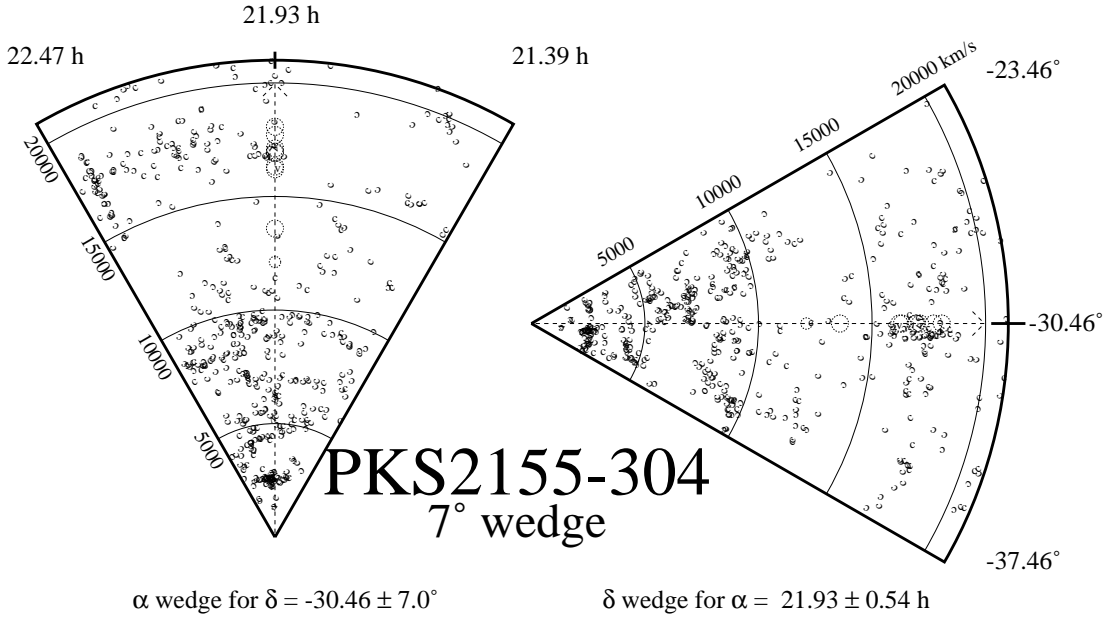


Fig. 34.— Right ascension (α) and declination (δ) pie diagram for the PKS2155-304 sightline. The arrow indicates that PKS 2155-304 lies beyond the extent of the pie diagram at $z = 0.1165$.

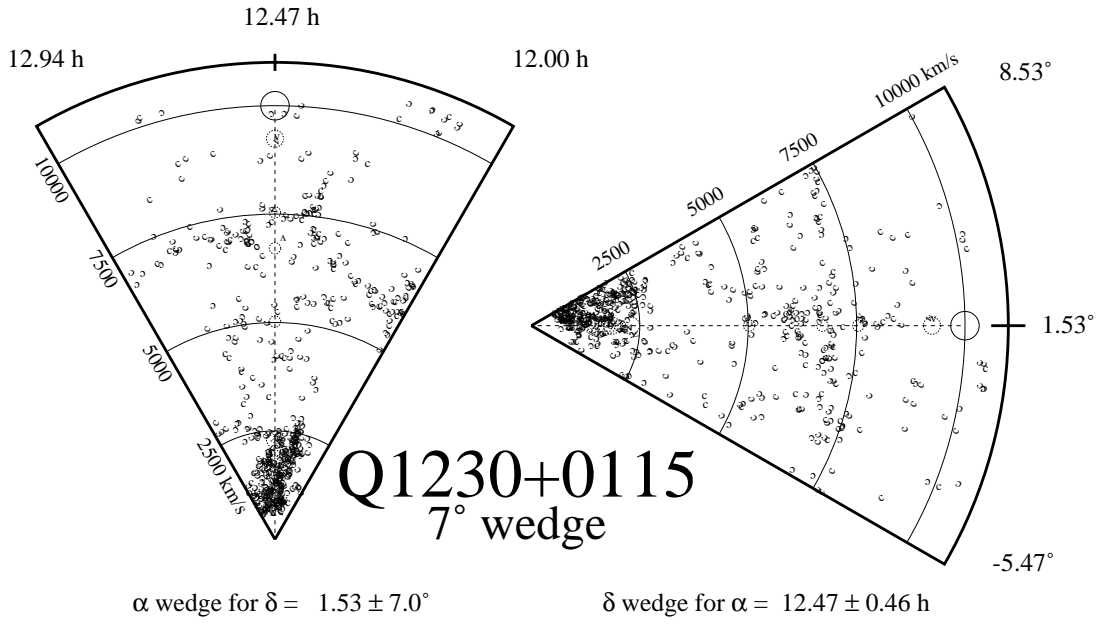


Fig. 35.— Right ascension (α) and declination (δ) pie diagram for the Q 1230+0115 sightline.

Table 10. Nearest three galaxies to each Ly α absorber.

Abs ^a Type (1)	Abs Vel (km s ⁻¹) (2)	Nearest Galaxy (3)	D_{\perp} ^b (h_{70}^{-1} Mpc) (4)	Gal Vel (km s ⁻¹) (5)	D_{cz} ^c (h_{70}^{-1} Mpc) (6)	D_{tot} ^d (h_{70}^{-1} Mpc) (7)	m_B (8)
3C 273							
D	1012	12285+0157	0.170	1105	0.000	0.170	15.6
D	1012	A1225+0152	0.182	1298	0.000	0.182	16.3
D	1012	A1224+0146	0.232	1275	0.000	0.232	...
D	1583	A1225+0152	0.182	1298	0.000	0.182	16.3
D	1583	12277+0254	0.260	1635	0.000	0.260	15.3
D	1583	A1224+0146	0.232	1275	0.121	0.261	...
P	2196	A1225+0258	0.396	2329	0.000	0.396	16.3
P	2196	12270+0107	0.677	2234	0.000	0.677	17.0
P	2196	A1228+0116	0.678	2289	0.000	0.678	18.3
D	2287	A1225+0258	0.396	2329	0.000	0.396	16.3
D	2287	12270+0107	0.677	2234	0.000	0.677	17.0
D	2287	A1228+0116	0.678	2289	0.000	0.678	18.3
P	4691	12303+0334	1.932	4985	0.000	1.932	15.3
P	4691	A1232+0317	1.962	4605	0.000	1.962	16.5
P	4691	N4496B	2.244	4546	0.000	2.244	14.0
D	7870	A1228+0205	0.944	7593	0.000	0.944	18.5
D	7870	A1228+0155	1.127	7587	0.000	1.127	18.8
D	7870	A1228+0147	1.432	7611	0.000	1.432	17.5
D	8829	A1226+0211	0.401	8807	0.000	0.401	18.1
D	8829	A1227+0246A	1.046	9059	0.000	1.046	17.6
D	8829	A1227+0246B	1.065	9164	0.484	1.170	19.1
D	9830	A1225+0223	0.394	9752	0.000	0.394	17.3
D	9830	A1227+0144	1.582	9281	3.572	3.907	17.7
D	9830	A1228+0146A	1.515	9176	5.072	5.293	19.1
P	12335	A1221+0122	4.515	11841	2.842	5.334	18.9
P	12335	A1224+0159	1.957	13115	6.837	7.112	18.6
P	12335	12316+0045E	6.447	12887	3.477	7.325	15.5
P	12587	A1224+0159	1.957	13115	3.235	3.781	18.6
P	12587	12316+0045E	6.447	12887	0.000	6.447	15.5

Table 10—Continued

Abs ^a Type (1)	Abs Vel (km s ⁻¹) (2)	Nearest Galaxy (3)	D_{\perp} ^b (h_{70}^{-1} Mpc) (4)	Gal Vel (km s ⁻¹) (5)	D_{cz} ^c (h_{70}^{-1} Mpc) (6)	D_{tot} ^d (h_{70}^{-1} Mpc) (7)	m_B (8)
P	12587	A1222+0207	3.705	13268	5.395	6.544	17.2
P	13141	A1224+0159	1.957	13115	0.000	1.957	18.6
P	13141	A1222+0207	3.705	13268	0.000	3.705	17.2
P	13141	12316+0045E	6.447	12887	0.000	6.447	15.5
D	14688	A1224+0230B	1.896	14860	0.000	1.896	18.5
D	14688	A1223+0238	3.407	14986	0.000	3.407	17.1
D	14688	12249+0332	4.637	14625	0.000	4.637	15.4
D	14984	A1224+0230B	1.896	14860	0.000	1.896	18.5
D	14984	A1223+0238	3.407	14986	0.000	3.407	17.1
D	14984	12249+0332	4.637	14625	0.900	4.724	15.4
D	15238	A1224+0230B	1.896	14860	1.137	2.210	18.5
D	15238	A1223+0238	3.407	14986	0.000	3.407	17.1
D	15238	12248+0334	4.810	14665	3.969	6.236	15.4
D	15927	A1223+0238	3.407	14986	9.196	9.807	17.1
D	15927	A1224+0230B	1.896	14860	10.977	11.140	18.5
D	15927	12248+0334	4.810	14665	13.810	14.623	15.4
D	18270	A1229+0222	3.906	18889	4.522	5.975	18.9
D	18270	A1226+0000	10.690	18415	0.000	10.690	...
D	18270	12285-0204	19.433	17642	5.443	20.181	15.5
D	19031	A1229+0222	3.906	18889	0.000	3.906	18.9
D	19031	A1226+0000	10.690	18415	4.732	11.691	...
D	19031	A1222+0249	5.609	20661	18.946	19.759	18.0
D	19953	A1222+0249	5.609	20661	5.770	8.047	18.0
D	19953	A1229+0222	3.906	18889	10.948	11.624	18.9
D	19953	12168-0020W	18.639	20613	4.547	19.185	16.7
Arakelian 120							
P	1846	04517+0135	3.017	2100	0.000	3.017	15.5
P	1846	04491-0239	3.448	2100	0.000	3.448	15.1
P	1846	A0547+0252	3.963	1776	0.000	3.963	...
D	4056	A0510-0036	0.865	4284	0.000	0.865	...

Table 10—Continued

Abs ^a Type (1)	Abs Vel (km s ⁻¹) (2)	Nearest Galaxy (3)	D_{\perp} ^b (h_{70}^{-1} Mpc) (4)	Gal Vel (km s ⁻¹) (5)	D_{cz} ^c (h_{70}^{-1} Mpc) (6)	D_{tot} ^d (h_{70}^{-1} Mpc) (7)	m_B (8)
D	4056	A0510-0037	0.864	4363	0.081	0.868	...
D	4056	05152-0113	1.245	4505	2.104	2.445	16.5
D	6749	05071-0018	2.837	6961	0.000	2.837	15.6
D	6749	05036-0006	4.388	7027	0.000	4.388	15.7
D	6749	05017-0029	5.224	7031	0.000	5.224	15.7
P	7808	A0509-0045	2.319	7888	0.000	2.319	...
P	7808	A0514+0052	2.012	7403	1.532	2.529	16.9
P	7808	05076-0046	3.152	7858	0.000	3.152	15.2
D	7883	A0509-0045	2.319	7888	0.000	2.319	...
D	7883	05076-0046	3.152	7858	0.000	3.152	15.2
D	7883	05077-0047	3.222	8115	0.000	3.222	15.7
D	7977	A0509-0045	2.319	7888	0.000	2.319	...
D	7977	05076-0046	3.152	7858	0.000	3.152	15.2
D	7977	05077-0047	3.222	8115	0.000	3.222	15.7
D	8037	A0509-0045	2.319	7888	0.000	2.319	...
D	8037	05076-0046	3.152	7858	0.000	3.152	15.2
D	8037	05077-0047	3.222	8115	0.000	3.222	15.7
ESO 141-G55							
P	9078	I4815	7.398	8441	5.048	8.956	14.4
P	9078	A1901-6129	6.871	8300	7.034	9.833	...
P	9078	I4849	9.930	9292	0.000	9.930	...
Fairall 9							
D	6255	A0105-5820	3.259	5914	0.651	3.323	16.1
D	6255	A0142-6122	5.600	6529	0.000	5.600	14.4
D	6255	A0147-5618	6.767	6151	0.000	6.767	13.4
D	7111	A0106-5837	4.043	7796	5.414	6.757	...
D	7111	A0142-6122	5.600	6529	4.209	7.006	14.4
D	7111	A0158-6014	8.046	6743	1.321	8.154	17.1

Table 10—Continued

Abs ^a Type (1)	Abs Vel (km s ⁻¹) (2)	Nearest Galaxy (3)	D_{\perp} ^b (h_{70}^{-1} Mpc) (4)	Gal Vel (km s ⁻¹) (5)	D_{cz} ^c (h_{70}^{-1} Mpc) (6)	D_{tot} ^d (h_{70}^{-1} Mpc) (7)	m_B (8)
D	9498	A0114-6153	6.536	8818	5.609	8.613	14.4
D	9498	A0127-6143	5.934	8657	7.881	9.866	...
D	9498	A0116-6146	5.973	8641	8.112	10.074	16.4
D	11649	A0101-5726	8.726	11114	3.611	9.444	...
D	11649	A0130-5554	10.189	12200	3.274	10.702	...
D	11649	A0103-5636	10.558	12200	3.252	11.047	...
D	11929	A0120-5934	1.722	12927	9.956	10.104	16.3
D	11929	A0104-5903	7.141	12745	7.224	10.158	15.4
D	11929	A0130-5554	10.189	12200	0.000	10.189	...
D	12098	A0120-5934	1.722	12927	7.538	7.732	16.3
D	12098	A0104-5903	7.141	12745	4.806	8.608	15.4
D	12098	A0130-5554	10.189	12200	0.000	10.189	...
D	12202	A0120-5934	1.722	12927	6.060	6.300	16.3
D	12202	A0104-5903	7.141	12745	3.328	7.878	15.4
D	12202	A0117-6006	3.876	13095	8.428	9.276	16.8
P	12277	A0120-5934	1.722	12927	4.992	5.280	16.3
P	12277	A0104-5903	7.141	12745	2.260	7.490	15.4
P	12277	A0117-6006	3.876	13095	7.360	8.318	16.8
D	12415	A0120-5934	1.722	12927	3.008	3.466	16.3
D	12415	A0117-6006	3.876	13095	5.376	6.628	16.8
D	12415	A0104-5903	7.141	12745	0.276	7.146	15.4
H 1821+643							
P	5493	18079+6341	2.480	6058	3.740	4.487	15.5
P	5493	18102+6402	1.956	6114	4.554	4.956	15.1
P	5493	N6493	6.073	5373	0.000	6.073	15.5
P	6123	Tripp0	0.871	6262	0.000	0.871	...
P	6123	18102+6402	1.956	6114	0.000	1.956	15.1
P	6123	18079+6341	2.480	6058	0.000	2.480	15.5
P	7208	Tripp1	0.869	7207	0.000	0.869	17.4
P	7208	18197+6340W	1.292	7364	0.000	1.292	15.7

Table 10—Continued

Abs ^a Type (1)	Abs Vel (km s ⁻¹) (2)	Nearest Galaxy (3)	D_{\perp} ^b (h_{70}^{-1} Mpc) (4)	Gal Vel (km s ⁻¹) (5)	D_{cz} ^c (h_{70}^{-1} Mpc) (6)	D_{tot} ^d (h_{70}^{-1} Mpc) (7)	m_B (8)
P	7208	18194+6340	1.294	7365	0.000	1.294	15.0
D	7325	Tripp1	0.869	7207	0.000	0.869	17.4
D	7325	18197+6340W	1.292	7364	0.000	1.292	15.7
D	7325	18194+6340	1.294	7365	0.000	1.294	15.0
D	7538	Tripp1	0.869	7207	0.447	0.978	17.4
D	7538	18197+6340W	1.292	7364	0.000	1.292	15.7
D	7538	18194+6340	1.294	7365	0.000	1.294	15.0
P	7798	18197+6340E	1.344	7756	0.000	1.344	15.7
P	7798	Tripp2	0.309	8250	2.163	2.185	20.6
P	7798	18194+6340	1.294	7365	1.921	2.316	15.0
D	7853	18197+6340E	1.344	7756	0.000	1.344	15.7
D	7853	Tripp2	0.309	8250	1.384	1.418	20.6
D	7853	Tripp123	0.615	8256	1.469	1.592	16.6
D	7941	Tripp2	0.309	8250	0.132	0.336	20.6
D	7941	Tripp123	0.615	8256	0.216	0.652	16.6
D	7941	18197+6340E	1.344	7756	0.000	1.344	15.7
P	9060	A1803+6312	5.045	8694	1.050	5.153	...
P	9060	Tripp124	0.435	8358	5.746	5.762	18.5
P	9060	18424+6226	6.435	8662	1.573	6.625	15.5
P	9651	18009+6301	6.358	9652	0.000	6.358	15.7
P	9651	17593+6246	6.994	9560	0.000	6.994	15.6
P	9651	A1759+6247	7.020	9598	0.000	7.020	...
P	11776	A1801+6553	7.777	11962	0.000	7.777	...
P	11776	17560+6439	7.814	11360	1.851	8.030	16.5
P	11776	18421+6358	6.942	12369	4.044	8.034	15.7
D	12323	18421+6358	6.942	12369	0.000	6.942	15.7
D	12323	A1801+6553	7.777	11962	1.061	7.849	...
D	12323	17583+6243	9.828	12881	3.411	10.403	15.7
Markarian 279							
D	5233	A1310+6745	6.229	5994	6.349	8.894	16.0

Table 10—Continued

Abs ^a Type (1)	Abs Vel (km s ⁻¹) (2)	Nearest Galaxy (3)	D_{\perp} ^b (h_{70}^{-1} Mpc) (4)	Gal Vel (km s ⁻¹) (5)	D_{cz} ^c (h_{70}^{-1} Mpc) (6)	D_{tot} ^d (h_{70}^{-1} Mpc) (7)	m_B (8)
D	5233	14010+6943	1.277	6293	10.838	10.913	15.5
D	5233	A1325+5945	12.321	4882	1.836	12.457	...
P	5473	A1310+6745	6.229	5994	2.922	6.880	16.0
P	5473	14010+6943	1.277	6293	7.411	7.520	15.5
P	5473	A1401+7005	1.532	6430	9.364	9.489	16.3
P	5618	14010+6943	1.277	6293	5.343	5.493	15.5
P	5618	A1310+6745	6.229	5994	0.853	6.287	16.0
P	5618	A1401+7005	1.532	6430	7.296	7.455	16.3
D	6359	14010+6943	1.277	6293	0.000	1.277	15.5
D	6359	A1401+7005	1.532	6430	0.000	1.532	16.3
D	6359	A1310+6745	6.229	5994	1.169	6.338	16.0
D	6432	14010+6943	1.277	6293	0.000	1.277	15.5
D	6432	A1401+7005	1.532	6430	0.000	1.532	16.3
D	6432	A1310+6745	6.229	5994	2.210	6.609	16.0
D	6913	A1401+7005	1.532	6430	2.631	3.045	16.3
D	6913	14010+6943	1.277	6293	4.584	4.759	15.5
D	6913	13300+7256	6.835	7187	0.000	6.835	15.3
D	7767	N5607	6.004	7595	0.000	6.004	13.9
D	7767	14189+7246	7.178	7434	0.717	7.214	15.4
D	7767	I1046	7.904	7948	0.000	7.904	14.7
D	7845	N5607	6.004	7595	0.000	6.004	13.9
D	7845	14189+7246	7.178	7434	1.834	7.409	15.4
D	7845	I1046	7.904	7948	0.000	7.904	14.7
Markarian 290							
P	4207	15436+5732	1.305	3957	0.000	1.305	16.5
P	4207	A1542+5722	1.360	4287	0.000	1.360	16.0
P	4207	15554+5851	2.892	4115	0.000	2.892	17.0
D	4651	A1542+5722	1.360	4287	0.939	1.652	16.0
D	4651	15592+5832	3.411	4223	1.934	3.921	14.8
D	4651	A1543+5951	2.682	5156	2.870	3.928	18.5

Table 10—Continued

Abs ^a Type (1)	Abs Vel (km s ⁻¹) (2)	Nearest Galaxy (3)	D_{\perp} ^b (h_{70}^{-1} Mpc) (4)	Gal Vel (km s ⁻¹) (5)	D_{cz} ^c (h_{70}^{-1} Mpc) (6)	D_{tot} ^d (h_{70}^{-1} Mpc) (7)	m_B (8)
P	4939	A1543+5951	2.682	5156	0.000	2.682	18.5
P	4939	A1542+5722	1.360	4287	5.050	5.230	16.0
P	4939	A1602+6000	4.393	4325	4.648	6.396	...
D	7071	A1505+6310	10.228	6584	3.231	10.726	...
D	7071	I1100	10.188	6561	3.557	10.791	14.1
D	7071	I1049	13.595	6728	1.582	13.687	14.8
D	7349	A1505+6310	10.228	6584	7.205	12.511	...
D	7349	I1100	10.188	6561	7.531	12.669	14.1
D	7349	A1457+5403	13.074	7974	3.886	13.639	16.0
P	7431	A1505+6310	10.228	6584	8.380	13.223	...
P	7431	A1457+5403	13.074	7974	2.710	13.352	16.0
P	7431	I1100	10.188	6561	8.706	13.401	14.1
Markarian 335							
D	1961	00025+1956	0.096	1950	0.000	0.096	16.0
D	1961	N7817	0.446	2310	0.692	0.823	12.7
D	1961	23533+1810	1.309	1738	0.000	1.309	17.0
D	2291	N7817	0.446	2310	0.000	0.446	12.7
D	2291	00025+1956	0.096	1950	0.589	0.597	16.0
D	2291	N7798	1.022	2403	0.000	1.022	12.7
D	4265	00008+2150	2.245	4455	0.000	2.245	16.0
D	4265	00017+2219	2.696	4444	0.000	2.696	15.4
D	4265	A0014+2031	2.879	4366	0.000	2.879	15.9
D	6266	00036+1928	0.692	5936	0.433	0.816	17.0
D	6266	N 15	2.457	6332	0.000	2.457	14.9
D	6266	A0002+1801	3.033	6315	0.000	3.033	17.2
Markarian 421							
D	3035	A1102+4120	2.142	2988	0.000	2.142	17.5
D	3035	11223+3554	3.105	2570	2.490	3.980	15.3

Table 10—Continued

Abs ^a Type (1)	Abs Vel (km s ⁻¹) (2)	Nearest Galaxy (3)	D_{\perp} ^b (h_{70}^{-1} Mpc) (4)	Gal Vel (km s ⁻¹) (5)	D_{cz} ^c (h_{70}^{-1} Mpc) (6)	D_{tot} ^d (h_{70}^{-1} Mpc) (7)	m_B (8)
D	3035	11032+4336	4.119	3224	0.000	4.119	14.6
Markarian 501							
D	4659	16510+3927	0.517	4625	0.000	0.517	15.0
D	4659	16381+4322	5.249	4763	0.000	5.249	15.6
D	4659	A1646+4437	5.559	4551	0.000	5.559	16.7
D	5990	16310+3727	6.300	5309	5.707	8.501	15.2
D	5990	16416+4556	8.433	5301	6.030	10.367	15.3
D	5990	I1226	8.786	5298	6.114	10.703	15.4
D	7521	17048+4107E	5.298	7852	0.313	5.307	15.6
D	7521	A1709+3941B	6.167	7600	0.000	6.167	...
D	7521	16360+4059	6.500	7908	1.051	6.584	16.0
D	8748	16572+4012	2.215	8714	0.000	2.215	14.9
D	8748	16482+4031	2.281	8956	0.000	2.281	15.7
D	8748	16558+4049	2.559	8625	0.000	2.559	15.4
Markarian 509							
D	2548	A2028-1821	4.662	2314	0.000	4.662	...
D	2548	A2115-0914	5.148	2402	0.000	5.148	...
D	2548	A2107-0354	5.268	2229	0.718	5.317	14.5
Markarian 817							
D	1918	14332+5934	0.282	1920	0.000	0.282	15.5
D	1918	N5667	0.495	1943	0.000	0.495	13.1
D	1918	N5678	0.496	1921	0.000	0.496	12.3
D	2082	14332+5934	0.282	1920	0.000	0.282	15.5
D	2082	A1439+5930	0.464	2331	0.000	0.464	17.0
D	2082	14399+5932	0.467	2325	0.000	0.467	17.0
D	4668	14293+5528	4.783	5291	4.459	6.539	15.6

Table 10—Continued

Abs ^a Type (1)	Abs Vel (km s ⁻¹) (2)	Nearest Galaxy (3)	D_{\perp} ^b (h_{70}^{-1} Mpc) (4)	Gal Vel (km s ⁻¹) (5)	D_{cz} ^c (h_{70}^{-1} Mpc) (6)	D_{tot} ^d (h_{70}^{-1} Mpc) (7)	m_B (8)
D	4668	N5368	8.403	4642	0.000	8.403	13.8
D	4668	13454+5549	8.554	4660	0.000	8.554	15.5
D	5074	14293+5528	4.783	5291	0.000	4.783	15.6
D	5074	N5368	8.403	4642	2.421	8.745	13.8
D	5074	13454+5549	8.554	4660	2.181	8.828	15.5
D	5221	14293+5528	4.783	5291	0.000	4.783	15.6
D	5221	N5368	8.403	4642	4.531	9.547	13.8
D	5221	13454+5549	8.554	4660	4.291	9.570	15.5
D	5778	14293+5528	4.783	5291	2.831	5.558	15.6
D	5778	A1420+5427	7.590	6176	1.065	7.664	18.5
D	5778	A1414+6042	5.079	6595	7.241	8.845	16.0
D	6240	A1414+6042	5.079	6595	0.637	5.119	16.0
D	6240	I1049	5.429	6728	2.521	5.986	14.8
D	6240	A1420+5427	7.590	6176	0.000	7.590	18.5
D	7316	I1049	5.429	6728	4.271	6.908	14.8
D	7316	A1414+6042	5.079	6595	6.154	7.979	16.0
D	7316	14526+6448	10.338	6761	4.201	11.159	15.1
D	7784	14212+6010	4.435	8520	6.138	7.572	15.3
D	7784	A1351+5746	11.212	7817	0.000	11.212	...
D	7784	A1457+5403	11.557	7974	0.000	11.557	16.0
PKS 2155-304 : Combined							
D	2629	A2156-3128	0.699	2786	0.000	0.699	16.7
D	2629	A2157-3142	0.796	2540	0.000	0.796	15.5
D	2629	A2159-3127	0.801	2608	0.000	0.801	15.4
D	2782	A2156-3128	0.699	2786	0.000	0.699	16.7
D	2782	A2157-3142	0.796	2540	0.000	0.796	15.5
D	2782	A2159-3127	0.801	2608	0.000	0.801	15.4
D	4028	N7201	2.160	4452	1.729	2.767	13.8
D	4028	A2159-3307	2.921	4266	0.000	2.921	14.4
D	4028	N7221	2.923	4358	0.354	2.944	13.1

Table 10—Continued

Abs ^a Type (1)	Abs Vel (km s ⁻¹) (2)	Nearest Galaxy (3)	D_{\perp} ^b (h_{70}^{-1} Mpc) (4)	Gal Vel (km s ⁻¹) (5)	D_{cz} ^c (h_{70}^{-1} Mpc) (6)	D_{tot} ^d (h_{70}^{-1} Mpc) (7)	m_B (8)
P	4706	N7201	2.160	4452	0.000	2.160	13.8
P	4706	A2147-3109	2.535	5044	0.489	2.582	16.3
P	4706	A2157-3025	0.332	5187	2.576	2.597	14.4
D	4948	A2157-3025	0.332	5187	0.000	0.332	14.4
D	4948	A2147-3109	2.535	5044	0.000	2.535	16.3
D	4948	I5139	2.636	5362	1.573	3.070	13.0
D	5010	A2157-3025	0.332	5187	0.000	0.332	14.4
D	5010	A2147-3109	2.535	5044	0.000	2.535	16.3
D	5010	I5139	2.636	5362	0.692	2.726	13.0
D	5115	A2157-3025	0.332	5187	0.000	0.332	14.4
D	5115	A2147-3109	2.535	5044	0.000	2.535	16.3
D	5115	I5139	2.636	5362	0.000	2.636	13.0
D	5615	A2157-3025	0.332	5187	1.834	1.864	14.4
D	5615	A2200-2909	2.317	5658	0.000	2.317	...
D	5615	A2200-2900	2.457	5614	0.000	2.457	15.3
D	5670	A2200-2909	2.317	5658	0.000	2.317	...
D	5670	A2200-2900	2.457	5614	0.000	2.457	15.3
D	5670	A2157-3025	0.332	5187	2.615	2.636	14.4
P	7720	A2159-2820	4.117	7210	3.096	5.152	15.2
P	7720	A2207-2913	5.238	7324	1.517	5.453	16.6
P	7720	A2206-2801	6.078	7319	1.634	6.294	14.0
P	9717	A2159-3042	1.814	9737	0.000	1.814	15.3
P	9717	A2159-3047	2.132	9454	0.000	2.132	16.2
P	9717	A2153-2928	2.777	9664	0.000	2.777	16.0
P	10099	A2159-3042	1.814	9737	0.909	2.029	15.3
P	10099	A2153-2928	2.777	9664	1.968	3.403	16.0
P	10099	A2201-3212	5.247	9804	0.038	5.247	...
P	12114	A2158-3112	2.759	11509	4.390	5.185	16.5
P	12114	A2158-3108	2.565	11470	4.944	5.570	16.5
P	12114	A2205-3027	6.348	12334	0.000	6.348	16.1
D	13588	A2143-2933	9.994	14030	1.769	10.150	15.6
D	13588	A2142-2923	10.548	13815	0.000	10.548	16.5

Table 10—Continued

Abs ^a Type (1)	Abs Vel (km s ⁻¹) (2)	Nearest Galaxy (3)	D_{\perp} ^b (h_{70}^{-1} Mpc) (4)	Gal Vel (km s ⁻¹) (5)	D_{cz} ^c (h_{70}^{-1} Mpc) (6)	D_{tot} ^d (h_{70}^{-1} Mpc) (7)	m_B (8)
D	13588	A2139-3020	11.257	13088	3.207	11.705	16.4
D	16200	A2155-3033A	0.576	16200	0.000	0.576	16.1
D	16200	A2156-3030B	0.888	16785	4.060	4.156	...
D	16200	A2154-3155	6.259	16730	3.194	7.027	15.9
D	16321	A2155-3033A	0.576	16200	0.000	0.576	16.1
D	16321	A2156-3030B	0.888	16785	2.329	2.492	...
D	16321	A2154-3155	6.259	16730	1.462	6.428	15.9
D	16922	A2155-3033B	0.441	17093	0.000	0.441	...
D	16922	A2156-3030A	0.653	17156	0.000	0.653	...
D	16922	A2156-3017	0.772	17179	0.000	0.772	...
D	16970	A2155-3033B	0.441	17093	0.000	0.441	...
D	16970	A2156-3030A	0.653	17156	0.000	0.653	...
D	16970	A2156-3017	0.772	17179	0.000	0.772	...
D	17115	A2155-3033B	0.441	17093	0.000	0.441	...
D	17115	A2156-3030A	0.653	17156	0.000	0.653	...
D	17115	A2156-3017	0.772	17179	0.000	0.772	...
D	17710	A2156-3017	0.772	17179	3.303	3.392	...
D	17710	A2156-3030A	0.653	17156	3.631	3.690	...
D	17710	A2155-3033B	0.441	17093	4.531	4.552	...
D	18070	A2156-2900	6.482	17739	0.536	6.504	16.6
D	18070	A2155-2851	7.319	18277	0.000	7.319	16.4
D	18070	A2156-3017	0.772	17179	8.454	8.489	...
Q 1230+0115							
D	1487	A1225+0152	0.271	1298	0.000	0.271	16.3
D	1487	12308+0147	0.279	1643	0.000	0.279	15.3
D	1487	A1224+0146	0.294	1275	0.000	0.294	...
D	1663	12308+0147	0.279	1643	0.000	0.279	15.3
D	1663	N4517A	0.365	1530	0.000	0.365	12.9
D	1663	A1223+0117	0.423	1473	0.000	0.423	17.1
D	1742	12308+0147	0.279	1643	0.000	0.279	15.3

Table 10—Continued

Abs ^a Type (1)	Abs Vel (km s ⁻¹) (2)	Nearest Galaxy (3)	D_{\perp} ^b (h_{70}^{-1} Mpc) (4)	Gal Vel (km s ⁻¹) (5)	D_{cz} ^c (h_{70}^{-1} Mpc) (6)	D_{tot} ^d (h_{70}^{-1} Mpc) (7)	m_B (8)
D	1742	N4517A	0.365	1530	0.000	0.365	12.9
D	1742	A1223+0117	0.423	1473	0.000	0.423	17.1
D	1857	12308+0147	0.279	1643	0.000	0.279	15.3
D	1857	N4517A	0.365	1530	0.394	0.538	12.9
D	1857	12277+0254	0.562	1635	0.000	0.562	15.3
P	2034	A1228+0116	0.162	2289	0.000	0.162	18.3
P	2034	12270+0107	0.293	2234	0.000	0.293	17.0
P	2034	N4536	0.585	1808	0.000	0.585	11.2
D	2298	A1228+0116	0.162	2289	0.000	0.162	18.3
D	2298	12270+0107	0.293	2234	0.000	0.293	17.0
D	2298	A1227+0018	0.749	2410	0.000	0.749	...
P	5022	A1235+0157	2.375	4935	0.000	2.375	...
P	5022	12360+0201	2.467	5006	0.000	2.467	14.7
P	5022	12361+0139	2.511	5174	0.000	2.511	15.2
P	6712	12268+0120	0.726	6948	0.000	0.726	15.0
P	6712	N4493NW	1.131	7012	0.000	1.131	14.9
P	6712	N4493SE	1.134	6934	0.000	1.134	16.0
P	7539	A1228+0147	0.522	7611	0.000	0.522	17.5
P	7539	A1228+0155	0.733	7587	0.000	0.733	18.8
P	7539	A1228+0205	1.069	7593	0.000	1.069	18.5
D	9239	A1227+0144	0.523	9281	0.000	0.523	17.7
D	9239	A1228+0146A	0.581	9176	0.000	0.581	19.1
D	9239	A1226+0211	1.859	8807	1.902	2.660	18.1

^aType of absorber, D=Definite ($SL \geq 4\sigma$) or P=Possible ($3\sigma \leq SL < 4\sigma$).

^bGalaxy distance, perpendicular to line-of-sight (LOS).

^cAbsorber-galaxy distance along LOS, assuming retarded Hubble flow (± 300 km s⁻¹).

^dTotal 3D Euclidean absorber-galaxy distance, assuming retarded Hubble flow.

REFERENCES

- Baldwin, J. 1977, *ApJ*, 214, 679
- Bahcall, J. N., Jannuzi, B. T., Schneider, B. P., Hartig, G. F., Bohlin, R., & Junkkarinen, V. 1991a, in *The First Year of HST Observations*, ed. A. L. Kinney & J. C. Blades (Baltimore: STScI), 46
- Bahcall, J. N., Jannuzi, B. T., Schneider, B. P., Hartig, G. F., Bohlin, R., & Junkkarinen, V. 1991b, *ApJ*, 377, L5
- Bahcall, J. N., et al. 1993, *ApJS*, 87, 1
- Bahcall, J. N., Bergeron, J., Boksenberg, A., Hartig, G. F., Jannuzi, B. T., Kirhakos, S., Sargent, W. L. W., Savage, B. D., Schneider, D. P., Turnshek, D. A., Weymann, R. J., & Wolfe, A. M. 1996, *ApJ*, 457, 19
- Bajtlik, S., Duncan, R. C., & Ostriker, J. P. 1988, *ApJ*, 327, 570
- Barlow, T. A., & Tytler, D. 1998, *AJ*, 115, 1725
- Brandt, J. C., et al. 1993, *AJ*, 105, 831
- Brandt, J. C., et al. 1997, *AJ*, 114, 554
- Burks, G. S., Bartko, F., Shull, J. M., Stocke, J. T., Sachs, E. R., Burbidge, E. M., Cohen, R. D., Junkkarinen, V. T., Harms, R. J., & Massa, D. 1994, *ApJ*, 437, 630
- Carswell, R. F., Whelan, J., Smith, M. G., Boksenberg, A., & Tytler, D. 1982, *MNRAS*, 198, 91
- Cen, R., Miralda-Escudé, J., Ostriker, J. P., & Rauch, M. 1994, *ApJ*, 437, L9
- Cowie, L. L., Songaila, A., Kim, T.-S., & Hu, E. M. 1995 *AJ*, 109, 22.
- Crenshaw, D. M., Kraemer, S. B., Boggess, A., Maran, S. P., Mushotzky, R. F., & Wu, C.-C. 1999, *ApJ*, 516, 750
- Cristiani et al. 1997, in *Structure and Evolution of the IGM from QSO Absorption Lines*, ed. P. Petitjean & S. Charlot, (Paris: Editions Frontières), 165
- Da Costa, L. N., et al. 1998, *AJ*, 116, 1
- Davé, R., Hernquist, L., Katz, N., & Weinberg, D. 1999, *ApJ*, 511, 521
- Fardal, M. A., Giroux, M. L., & Shull, J. M. 1998, *AJ*, 115, 2206
- Gibson, B. K., Giroux, M. L., Penton, S. V., Stocke, J. T., & Shull, J. M. 2000a, *AJ*, submitted

- Gibson, B. K., Giroux, M. L., Penton, S. V., Putman, M. E., Stocke, J. T., & Shull, J. M. 2000b, AJ, submitted
- Gilliland, R. L., Morris, S. L., Weymann, R. J., Ebbets, D. C., & Lindler, D. J. 1992, PASP, 104, 367
- Gilliland, R., & Hulbert, S. 1993, GHRS Instrument Science Report 55
- Giovanelli, R., & Haynes, M. P. 1984, AJ, 89, 758
- Grogin, N. A., & Geller, M. J. 1998, ApJ, 505, 506
- Grogin, N. A., Geller, M. J., & Huchra, J. P. 1998, ApJS, 119, 277
- Haardt, F., & Madau, P. 1996, ApJ, 461, 20
- Hartmann, D., & Burton, W. B. 1997, Atlas of Galactic Neutral Hydrogen (Cambridge: Cambridge Univ. Press)
- Haynes, R. F., et al. 1999, in New Views of the Magellanic Clouds, ed. Y.-H. Chu, et al., (San Francisco: ASP), 63
- Hernquist, L., Katz, N., Weinberg, D. H., & Miralda-Escudé, J. 1996, ApJ, 457, L51
- Huchra, J., Geller, M., Clemens, C., Tokarz, S., & Michel, A. 1992, Bull. C.D.S., 41, 31
- Huchra, J. P., Vogeley, M. S., & Geller, M. J. 1999, ApJS, 121, 287
- Impey, C. D., Petry, C. E., & Flint, K. P. 1999, ApJ, 524, 536
- Jannuzi, B. T., et al. 1998, ApJS, 118, 1
- Lanzetta, K. M., Bowen, D. V., Tytler, D., & Webb, J. K. 1995, ApJ, 442, 538
- Kriss, G. A., et al. 2000, ApJ, in press
- Lockman, F. J., & Savage, B. D. 1995, ApJS, 97, 1
- Lu, M., Savage, B., & Sembach, K. 1994, ApJ, 417, L119
- Lu, L., Sargent, W. L., Womble, D. S., & Takada-Hidai, M. 1996, AJ, 472, 509
- Mandel, J. 1984, The Statistical Analysis of Experimental Data, (New York, Dover).
- Markwardt, C., 14 June 1999 Version, <http://astro.physics.wisc.edu/~craigm/idl/idl.html>
- Marzke, R. O., Huchra, J. P., & Geller, M. J. 1996, AJ, 112, 1803
- Miralda-Escudé, J., & Ostriker, J. P. 1990, ApJ, 350, 1

- Moré, J., & Wright, S. 1993, *Frontiers in Applied Math*, Number 14, *Optimization Software Guide*, SIAM.
- Morras, R. 1983, *AJ*, 88, 62
- Morris, S. L., Weymann, R. J., Savage, B. D., & Gilliland, R. L. 1991, *ApJ*, 377, L21
- Morris, S. L., Weymann, R. J., Dressler, A., McCarthy, P. J., Smith, B. A., Terrile, R. J., Giovanelli, R., & Irwin, M. 1993, *ApJ*, 419, 524
- Morris, S. L., & van den Bergh, S. 1994, *ApJ*, 427, 696
- Morton, D. C. 1991, *ApJS*, 77, 119
- Murdoch, H. S., Hunstead, R. W., Pettini, M., & Blades, J. C. 1986, *ApJ*, 309, 19
- Murphy, E. M., Lockman, F. J., & Savage, B. D. 1995, *ApJ*, 447, 642
- Oegerle, W. R., Tripp, T. M., Sembach, K. R., Jenkins, E. B., Bowen, D. V., Savage, B. D., Shull, J. M., & York, D. G. 2000, *ApJ*, in press
- Penton, S. V., Shull, J. M., & Stocke, J. T. 2000a, *ApJ*, submitted (Paper II)
- Penton, S. V., Stocke, J. T., & Shull, J. M. 2000b, in preparation (Paper III)
- Penton, S. V., Shull, J. M., & Stocke, J. T. 2000c, in preparation (Paper IV)
- Penton, S. V., Shull, J. M., & Edelson, R. 2000d, *Database of IUE-AGN Ultraviolet Spectra*, in preparation, see <http://casa.colorado.edu/~iueagn>
- Rauch, M., Weymann, R. J., & Morris, S. L. 1996 *ApJ*, 458, 518.
- Russell, S. C., & Dopita, M. A. 1992, *ApJ*, 384, 508
- Sargent, W. L. W., Young, P. J., Boksenberg, A., & Tytler, D. 1980, *ApJS*, 42, 41
- Sargent, W. L. W. 1987 in *QSO Absorption Lines*, ed. J. C. Blades, D. Turnshek & C. A. Norman (Cambridge: Cambridge Univ. Press), 1.
- Savage, B., Sembach, K., & Lu, L. 1995, *ApJ*, 449, 145
- Savage, B., Sembach, K., & Lu, L. 1997, *AJ*, 113, 2158
- Savage, B., Tripp, M., & Lu, L. 1998, *AJ*, 115, 436
- Sherbert, L., & Hulbert, S. 1997, *GHRS Instrument Science Report 67 (Official Update)*
- Sembach, K. R., Savage, B. D., & Lu, L. 1995a, *ApJ*, 449, 145
- Sembach, K. R., Savage, B. D., Murphy, E., & Lu, L. 1995b, *ApJ*, 451, 616

- Sembach, K. R., & Savage, B. D. 1996, *ApJ*, 457, 211
- Sembach, K. R., Savage, B. D., Lu, L., & Murphy, E. M. 1999, *ApJ*, 515, 108
- Shapiro, P. R., & Benjamin, R. A. 1993, in *Star-Forming Galaxies and their Interstellar Media*, ed. J. Franco (Cambridge: Cambridge Univ. Press), 273
- Shapiro, P. R., Giroux, M., & Babul, A. 1994, *ApJ*, 427, 25
- Shull, J. M., Stocke, J. T., & Penton, S. V. 1996, *AJ*, 111, 72
- Shull, J. M. 1997, in *Structure and Evolution of the IGM from QSO Absorption Lines*, ed. P. Petitjean & S. Charlot, (Paris: Editions Frontières), 101
- Shull, J. M., Penton, S. V., Stocke, J. T., Giroux, M. L., van Gorkom, J. H., Lee, Y. H., & Carilli, C. 1998, *AJ*, 116, 2094
- Shull, J. M., Penton, S. V., & Stocke, J. T. 1999a, *PASA*, Vol. 16, No. 1, 95
- Shull, J. M., Roberts, D., Giroux M. L., Penton, S. V., & Fardal, M. A. 1999b, *AJ*, 118, 1450
- Shull, J. M., Giroux, M. L., Penton, S. V., Tumlinson, J., Jenkins, E. B., Moos, H. W., Oegerle, W. R., Savage, B. D., Sembach, K. R., York, D. G., and the FUSE Science Team 2000, *ApJ*, submitted
- Slavin, J. D., Shull, J. M., & Begelman, M. C. 1993, *ApJ*, 407, 83
- Songaila, A., Cowie, L. L., & Hu, E. M. 1995
- Steidel, C. C., 1995 in *QSO Absorption Lines*, ed. G. Meylan (Berlin: Springer), 139
- Stocke, J. T., Shull, J. M., Penton, S. V., Donahue, M., & Carilli, C. 1995, *ApJ*, 451, 24 (S95)
- Tripp, T. M., Lu, L., & Savage, B. D. 1998a, *ApJ*, 508, 200
- Tripp, T.M., Lu, L., & Savage, B. D. 1998b, in *The Scientific Impact of the Goddard High Resolution Spectrograph*, ASP Conference Series, Vol. 143, ed., J. C. Brandt, T. B. Ake, C. C. Peterson, 261
- Tufte, S. L., Reynolds, R. J., & Haffner, L. M. 1999, in *Stromlo Workshop on High Velocity Clouds*, ASP Conference Series, Vol 166, ed., B. K. Gibson, & M. E. Putman, 231
- Tytler, D., Fan, X.-M., Burles, S., Cottrell, L, Davis, C., Kirkman, D., & Lin, Z. 1995 in *QSO Absorption Lines*, ed. G. Meylan (Berlin: Springer), 289
- Van Gorkom, J. H., Bahcall, J. N., Jannuzi, B. T., & Schneider, D. P. 1993, *AJ*, 106, 2213
- Van Gorkom, J. C., Carilli, C. L., Stocke, J. T., Perlman, E. S., & Shull, J. M. 1996, *AJ*, 112, 1397

- Wakker B. P., & van Woerden, H. 1991, *A&A* 250, 509
- Wakker B. P., van Woerden, H., Schwarz U. J., Peletier, R. F., & Douglas, N. 1996, *A&A*, 306, L25
- Weymann, R., Rauch, M., Williams, R., Morris, S., & Heap, S. 1995, *ApJ*, 438, 650
- Weymann, R., et al. 1998, *ApJ*, 506, 1
- Wolfe, A. M. 1995, in *QSO Absorption Lines*, ed. G. Meylan (Berlin: Springer), 13.
- York, D. G., Blades, J. C., Cowie, L., Morton, D. C., Songaila, A., & Wu, C. 1982, *ApJ*, 225, 467
- Zhang, Y., Meiksin, A., Anninos, P., & Norman, M. 1997, *ApJ*, 495, 63